

**REPORT ON RESEARCH ACTIVITIES
FOR THE QUARTER
APRIL 1 THROUGH JUNE 30, 1990**

Prepared for

**Nuclear Regulatory Commission
Contract NRC-02-88-005**

Prepared by

**Center for Nuclear Waste Regulatory Analyses
San Antonio, Texas**

August 1990

**REPORT ON RESEARCH ACTIVITIES
FOR THE QUARTER
APRIL 1 THROUGH JUNE 30, 1990**

Prepared for

Nuclear Regulatory Commission
Contract NRC-02-88-005

Edited by

Wesley C. Patrick

**Center for Nuclear Waste Regulatory Analyses
San Antonio, Texas**

August 1990

TABLE OF CONTENTS (Cont'd)

	<u>Page</u>
3. THERMOHYDROLOGY by Ronald T. Green, Frank Dodge, and Steve Svedeman	3-1
3.1 Technical Objectives	3-1
3.2 Design and Execution of Preliminary Separate Effects Experiments	3-1
3.2.1 Separate Effects Experimental Apparatus	3-1
3.2.2 Separate Effects Experiments	3-3
3.2.2.1 Separate Effects Experiment Test 3	3-3
3.2.2.2 Separate Effects Experiment Test 4	3-5
3.2.2.3 Separate Effects Experiment Test 5	3-8
3.2.3 Separate Effects Experiments Results	3-14
3.2.3.1 Results of Separate Effects Experiment Test 3	3-14
3.2.3.2 Results of Separate Effects Experiment Test 4	3-15
3.2.3.3 Results of Separate Effects Experiment Test 5	3-15
3.3 Simulation Experiments	3-16
4. SEISMIC ROCK MECHANICS by Simon M. Hsiung and Asadul H. Chowdhury	4-1
4.1 Technical Objectives	4-1
4.2 Evaluation of Rock-Joint Models and Computer Codes	4-1
4.2.1 Cyclic Loading of a Specimen with a Slipping Joint	4-1
4.2.2 Slip in a Jointed Body Induced by a Harmonic Shear Wave	4-3
4.2.3 Line Source in an Elastic Medium with a Slip-Prone Joint	4-4
4.3 Specimen Preparation Activities	4-5
4.3.1 Direct Shear Specimen Preparation	4-8
4.3.2 Uniaxial and Triaxial Compression Specimens	4-9
4.3.3 Brazilian Disk Tension Specimens	4-9
4.3.4 Problems for Direct Shear Specimen Preparation	4-12

TABLE OF CONTENTS (Cont'd)

	<u>Page</u>
4.4 Nevada Test Site (NTS) Data Collection on Ground-Shock Excitation	4-12
4.5 Field Investigation	4-14
4.5.1 Excavation Response	4-14
4.5.2 Piezometers - Pore Water Pressure Measurement	4-15
4.5.3 Data Acquisition	4-16
4.6 References	4-18
5. INTEGRATED WASTE PACKAGE EXPERIMENTS <i>by Gustavo Cragolino and Narasi Sridhar</i>	5-1
5.1 Technical Objectives	5-1
5.2 Collection and Review of Information on Corrosion for Waste-Package Containers	5-1
5.2.1 LLNL Investigations	5-2
5.2.2 Cortest Investigations	5-3
5.2.3 Future Research Needs	5-4
5.3 Waste Package Experimental Programs	5-5
5.3.1 Corrosion of Container Materials in the Tuff Repository Environments	5-5
5.3.1.1 Microstructural Analyses of CDA-613	5-5
5.3.1.2 Corrosion Tests in Standard Solutions	5-8
5.3.1.3 Electrochemical Characterization of Materials	5-8
5.3.2 Metallurgical Stability of Container Materials in the Tuff Repository Environment	5-13
5.4 Summary of Results	5-15
5.5 References	5-16

TABLE OF CONTENTS (Cont'd)

	<u>Page</u>
6. STOCHASTIC ANALYSIS OF UNSATURATED FLOW AND TRANSPORT <i>by Rachid Ababou</i>	6-1
6.1 Technical Objectives	6-1
6.2 Research Accomplishments	6-1
6.2.1 Three-Dimensional Synthetic-Flow Experiment	6-2
6.2.2 Numerical Analysis of Nonlinear Unsaturated Flow	6-2
6.2.3 Unsaturated Coefficients and Statistical Correlations	6-2
7. GEOCHEMICAL NATURAL ANALOGS <i>by English C. Percy</i>	7-1
7.1 Technical Objectives	7-1
7.2 Activity This Period in Task 1	7-1
7.2.1 Technical Presentation and Literature Review	7-1
7.2.2 Possible Sites for Geochemical Analog Research	7-2
7.2.2.1 Yucca Mountain, Nevada	7-2
7.2.2.2 Peña Blanca, Mexico	7-3
7.2.2.3 Santorini, Greece	7-5
7.3 Conclusions	7-7
7.4 References	7-7
APPENDIX A - High-Resolution Modeling of Strip Source Infiltration: Three-Dimensional Synthetic Experiment Analogous to Las Cruces Trench Experiment <i>by R. Ababou</i>	A-1
APPENDIX B - Numerical Analysis of Nonlinear Unsaturated Flow Equations <i>by R. Ababou</i>	B-1

LIST OF FIGURES

<u>Figure</u>	<u>Title</u>	<u>Page</u>
2-1	X-ray diffraction pattern of clinoptilolite-rich tuff from Death Valley Junction, California	2-3
2-2	X-ray diffraction pattern of heulandite from Poona, Maharashtra State, India	2-4
2-3	X-ray diffraction pattern of clinoptilolite-rich from Death Valley Junction, California, after heavy liquid separation	2-5
2-4	Concentration of K^+ in the aqueous phase as a function of time	2-9
2-5	Concentration of Na^+ in the aqueous phase as a function of time	2-10
2-6	Concentration of Ca^{2+} in the aqueous phase as a function of time	2-11
2-7	Concentration of Na^+ in the aqueous phase as a function of time	2-12
2-8	Ratio of the concentrations of Na^+ to K^+ in clinoptilolite as a function of the ratio of the concentrations (millimoles per liter) of Na^+ to K^+ in possibly coexisting water	2-17
2-9	Ratio of the concentration of Mg^{2+} to Ca^{2+} in clinoptilolite as a function of the ratio of the concentrations (millimoles per liter) of Mg^{2+} to Ca^{2+} in possibly coexisting water	2-17
2-10	Ratio of the square of the concentration of Na^+ to the concentration of Ca^{2+} in clinoptilolite (concentrations in atoms per 72 oxygens) as a function of the ratio of the square of the concentration of Na^+ to the concentration of Ca^{2+} in possibly coexisting water (concentrations in millimoles per liter)	2-18
2-11	Ratio of the square of the concentration of Na^+ to the concentration of Ca^{2+} in clinoptilolite (concentrations in atoms per 72 oxygens) as a function of the ratio of the square of the concentration of Na^+ to the concentration of Ca^{2+} in possibly coexisting water (concentrations in millimoles per liter)	2-18
2-12	Ratio of the square of the concentration of K^+ to the concentration of Ca^{2+} in clinoptilolite (concentrations in atoms per 72 oxygens) as a function of the ratio of the square of the concentration of K^+ to the concentration of Ca^{2+} in possibly coexisting water (concentrations in millimoles per liter)	2-19

LIST OF FIGURES (Cont'd)

<u>Figure</u>	<u>Title</u>	<u>Page</u>
2-13	Ratio of the square of the concentration of Na^+ to the concentration of Mg^{2+} in clinoptilolite (concentrations in atoms per 72 oxygens) as a function of the ratio of the square of the concentration of Ma^+ to the concentration of Mg^{2+} in possibly coexisting water (concentrations in millimoles per liter)	2-19
2-14	Ratio of the square of the concentration of K^+ to the concentration of Mg^{2+} in clinoptilolite (concentrations in atoms per 72 oxygens) as a function of the ratio of the square of the concentration of K^+ to the concentration of Mg^{2+} in possibly coexisting water (concentrations in millimoles per liter)	2-20
2-15	Aqueous silica concentration as a function of mineralogic environment: major water-producing horizons above and below the mineralogic discontinuity	2-21
3-1	Design details of the smaller test chamber with densitometer measurement locations	3-2
3-2	Test 3 sequence of events as measured at densitometer locations (9,6) and (9,18)	3-4
3-3	Ambient temperature and pressure during Test 3	3-6
3-4	Temperature measured in the test chamber during Test 3	3-6
3-5	Tensiometer measurements during Test 3. Pressure is measured relative to barometric pressure	3-7
3-6	Densitometer measurements from Test 3 at locations (11,3) through (11,21)	3-7
3-7	Test 4 sequence of events as measured at the temperature sensor locations	3-8
3-8	Ambient temperature and pressure during Test 4	3-9
3-9	Tensiometer measurements during Test 4. Pressure is measured relative to barometric pressure	3-9
3-10	Densitometer measurements from Test 4 from locations (11,15), (11,18), and (11,21) and at locations (15,15), (15,18) and (15,21)	3-10

LIST OF FIGURES (Cont'd)

<u>Figure</u>	<u>Title</u>	<u>Page</u>
3-11	Test 5 sequence of events as measured at the two heat-exchanger temperature sensors	3-11
3-12	Ambient temperature and pressure during Test 5	3-12
3-13	Photograph of the test chamber at day 7 of Test 5	3-13
3-14	Photograph of the test chamber at day 14 of Test 5	3-13
3-15	Photograph of the test chamber at day 23 of Test 5	3-13
3-16	Extent of moisture infiltration at day 2 of Test 3	3-14
4-1	Three benchmark analytical problems (a,b, and c)	4-2
4-2	3DEC block model of the three-dimensional specimen with a planar crack for benchmark problem (a) in Figure 4-1	4-3
4-3	3DEC block model showing internal discretization for benchmark problem (b) in Figure 4-1	4-5
4-4	Comparison of transmission, reflection, and absorption coefficients	4-6
4-5	Shear stress versus time at points A and B for slipping discontinuity (cohesion=0.5 MPa)	4-6
4-6	Problem geometry and boundary conditions for numerical model for benchmark problem (c) in Figure 4-1	4-7
4-7	3DEC model showing semicircular source and "joined" blocks used to provide appropriate zoned discretization for benchmark problem (c) in Figure 4-1	4-7
4-8	Comparison of dimensionless slip at point P with Coulomb joint model dimensionless slip = $(4hp\beta^2/m_o)\delta u$, dimensionless time = $t\beta/h$	4-8
4-9	Core drilled at the field site shown set up for laboratory coring	4-9
4-10	Direct shear specimen shown in the cutting process using a slab saw	4-10

LIST OF FIGURES (Cont'd)

<u>Figure</u>	<u>Title</u>	<u>Page</u>
4-11	Three prepared direct shear specimens	4-10
4-12	Grinding machine	4-11
4-13	Two Brazilian disk tension specimens and one compression specimen in the preparation process	4-11
4-14	Proposed typical instrumentation array for cross sections of the 5210 sublevel at 95 and 101 stopes	4-16
4-15	Lucky Friday silver shaft cross section of the proposed drill hole for piezometer installation (view looking N74°E)	4-17
5-1	SEM-EDX analysis of polished and etched CDA-613 alloy. 20kV 2000X	5-7
5-2	ASTM A-262 B test results	5-9
5-3	Surface Cr depletion	5-9
5-4	Sample curve from a cyclic polarization test	5-12
5-5	Effect of chloride in simulated J-13 water on pitting of Incoloy 825. P=Pit, C=Crevice Attack	5-13
5-6	Effect of chloride in simulated J-13 water on pitting of 304L stainless steel. P=Pits	5-14

LIST OF TABLES

<u>Table</u>	<u>Title</u>	<u>Page</u>
2-1	X-ray Diffraction Pattern of Clinoptilolite-Rich Tuff from Death Valley Junction, California: (a,b)	2-6
2-2	Composition of Na-exchanged Clinoptilolite Based on ICP or AA Analysis	2-7
2-3	Comparison of K^+ or Ca^{2+} Equivalents Removed from Solution with Na^+ Equivalents Released into Solution	2-12
4-1	Comparison of 3DEC Results with Conceptual Model and UDEC for a Block with a Slipping Crack Under Cyclic Loading	4-4
4-2	Candidate Field Tests of Block Motion	4-13
5-1	Corrosion Test Results for Stainless Steels Specimens (McCright, 1984)	5-2
5-2	Corrosion Rate of Candidate Container Materials in J-13 Water as Determined from Weight-Loss Data (Glass, 1984)	5-3
5-3	Solubility of Iron in Cu-Al Alpha Phase as a Function of Temperature (Brezina, 1982)	5-6
5-4	Results of Cyclic Polarization Tests on Incoloy Alloy 825 in Simulated J-13 Solutions Modified to Various Chloride Levels	5-11
5-5	Diffusivity of Hydrogen in Candidate Container Materials Measured by Electrolytic Permeation Technique	5-15

ACKNOWLEDGMENTS

This report was prepared to document work performed by the Center for Nuclear Waste Regulatory Analyses (CNWRA) for the U.S. Nuclear Regulatory Commission (NRC) under Contract No. NRC-02-88-005. The research activities reported here were performed on behalf of the NRC Office of Regulatory Research, Division of Engineering. The report is an independent product of the CNWRA and does not necessarily reflect the views or regulatory position of the NRC.

Each chapter of this report acknowledges those investigators who, although not specifically involved in writing the report, made significant contributions to the research projects. In addition, the authors gratefully acknowledge the technical support and technical reviews conducted by other members of the CNWRA and Institute staffs. Appreciation is particularly due Faye Forcum and Yolanda Lozano, who prepared the text of the document; Curtis Gray, who provided graphical assistance; and Dr. Shirley Heller, who provided a full range of expert editorial services in the preparation of the final document.

1. EXECUTIVE SUMMARY

1.1 INTRODUCTION

This is the second in a series of research quarterly reports which document and make available to the technical community work that has been undertaken by the Center for Nuclear Waste Regulatory Analyses (Center) as part of its contract with the U.S. Nuclear Regulatory Commission (NRC). Reports are prepared each calendar quarter, with the fourth such report each year constituting the annual progress report.

Each of the research projects discussed here are being conducted in accordance with approved Research Project Plans, which were developed in response to research needs identified by the NRC and the Center. These Plans are the vehicle for establishing the objectives, technical approach, justification, and funding for each of the studies. In addition, the Project Plans describe the interrelationships among the various projects which provide a sound basis for integrating research results. Because these are primarily planning and program management matters, they are not discussed further here (with the exception of objectives).

In reading this report, it is important to realize that several of the projects have recently been approved. Consequently, there is relatively little work to report at this time. In such cases, this quarter's report provides basic information on the objectives of the new projects as well as early activities such as literature assessments. Other projects have been in progress long enough that significant technical progress in laboratory, computational, or field studies can be reported.

This report is organized to provide, first, an Executive Summary that documents in capsule form, the progress over the past quarter of each research project. The Executive Summary is followed by Chapters 2-7 representing respectively each of the six currently active research projects. Project objectives and a report of research activities and results (as appropriate) to date are given in each chapter.

1.2 UNSATURATED MASS TRANSPORT (GEOCHEMISTRY)

1.2.1 Experimental Studies

A major geologic feature potentially affecting the suitability of Yucca Mountain, Nevada, as a repository site for high-level nuclear wastes is the presence of thick lateral zones of zeolitic tuffs. Because of their sorptive properties, zeolites could provide important geologic barriers to migration of radionuclides away from the repository to the accessible environment. To support NRC's high-level waste program, the Center is conducting experimental studies on the thermodynamic and ion exchange properties of zeolites under Task 3 of the Geochemistry Research Project. These studies are designed to generate data needed to evaluate the effectiveness of zeolitic tuffs as barriers to radionuclide migration.

The work conducted during this quarter was aimed at determining the kinetics of ion exchange between clinoptilolite and aqueous solutions. The initial experiments were

conducted using Na-enriched clinoptilolite and aqueous solutions of potassium or calcium chloride. The results provide constraints on isotherm experiments that are planned to be conducted, as well as providing useful estimates of ion exchange rates among aqueous species in groundwater and zeolite minerals in geologic media.

On the basis of previous characterization work on clinoptilolite-rich tuff specimens from various localities (CNWRA, 1990), samples from Death Valley Junction, California, were chosen as run materials for the experiments. Na-enriched clinoptilolite was prepared from these samples after removing most of the mineral impurities by heavy liquid separation, and ion exchanging the zeolite with NaCl solutions at 70°C for at least 9 days. Kinetic experiments were conducted by reacting weighed amounts of Na-enriched clinoptilolite with aqueous solutions of KCl, CaCl₂, KCl + NaCl, and CaCl₂ + NaCl. The ion exchange reactions were followed by taking aliquots of the aqueous phase on a periodic basis, and analyzing the concentrations of K⁺, Ca²⁺, and/or Na⁺ by inductively coupled plasma emission spectrometry or by using ion-selective electrodes. The concentrations determined using these two techniques generally agree within analytical uncertainty. Charge balance calculations comparing the equivalents of K⁺ or Ca²⁺ removed from solution with the equivalents of Na⁺ released from the clinoptilolite indicate the exchange reactions are essentially binary in nature, with insignificant effects of exchangeable ions other than Na⁺ that may be present in clinoptilolite and in mineral impurities, or of H⁺ in the aqueous phase. The results of the kinetic ion exchange experiments indicate that equilibrium is attained in the systems studied within 2 days. A minimum of 3 days is anticipated to be used in the isotherm experiments to be conducted next quarter.

1.2.2 Geochemical Modeling

Groundwater and mineral chemistry data from Yucca Mountain were analyzed to identify correlations that would aid the conditioning and validation of computational models based on chemical equilibrium. Thermodynamic evaluation of field data for possibly coexisting clinoptilolites and waters from Yucca Mountain, Nevada, for consistency with cation exchange equilibrium presently yield inconclusive results. The analysis is restricted particularly because of the weak control on the locations from which water samples have been collected. However, within the range of compositions observed, equilibrium interpretations are permissive and at least partially consistent with experimental exchange data in binary systems. Clinoptilolite and cristobalite occur above analcime and kaolinite at Yucca Mountain. Waters collected from producing zones above this mineralogic transition have generally higher aqueous silica concentrations than waters collected from producing zones below this discontinuity. The limited data support the proposal that this change in mineralogy is controlled by variations in the activity of aqueous silica.

1.3 THERMOHYDROLOGY

Work continued on the separate effects experiments during this past quarter with Tests 3, 4, and 5 being concluded. Parallel efforts also continued with regard to the modeling of two-phase flow through porous media as applied to the separate effects experiments.

There were several differences in the experimental setup in Tests 3 and 4 as compared to the setup for Tests 1 and 2. Adaptations to the test chamber used in Tests 3 and 4

include the installation of a bolt through the side walls to prevent bowing and the addition of styrofoam insulation to reduce heat loss and temperature fluctuations. The medium used in Tests 3, 4, and 5 was a mixture of two bead sizes. Test 5 used a smaller-sized test chamber and also included a simulated fracture located midway through the medium and approximately equidistant and parallel to the two heat exchangers. Because of the limited size of the small test chamber, tensiometers and thermistors were not installed into the medium in Test 5. Two ports were installed in the side walls of the smaller test chamber to permit injecting either water or colored dyes into the medium.

The moisture content of the medium was measured during Test 5, as in Tests 3 and 4, using a gamma-ray densitometer. The gamma-ray source of the densitometer was the same as in the previous experiments; however, a new detector was used in Test 5.

The movement of the colored dyes proved to be the most useful output information of Test 5. Although general moisture-content trends can be made using the densitometer measurements, the resolution of the densitometer measurements is not sufficient to provide quantitatively significant data for evaluation purposes.

Major shortcomings of the densitometer method in Test 5 were the narrow depth of the test chamber, thermal fluctuations in the environment where the test was conducted, and density differences in water that were attributable to temperature changes.

As observed with the dye, the induced fracture had a pronounced affect upon the flow paths of water in the medium. In particular, the water moved very little across the fracture as evidenced by the dyes. Intuitively, it was thought that water proximal to the heated surface would rise until encountering the top of the chamber, then move inward until encountering the induced fracture. Contrary to this early hypothesis, the initial direction of flow was downward along the face of the heat exchanger until arriving at the lower end of the test chamber, then toward the interior of the chamber. Movement of water across the induced fracture was not noted until late in the test when the half of the medium near the higher temperature heat exchanger visibly began to dry and the material on the other side became visibly wetter.

1.4 SEISMIC ROCK MECHANICS

During this reporting quarter, activities such as instrumented field studies, rock-joint shear-test specimen preparation, computer-code qualification studies, Nevada Test Site (NTS) data collection on ground shock excitation, and preparation of cylindrical specimens for material characterization tests were carried out.

Three of the four benchmark analytical problems were analyzed for the qualification study on the 3DEC computer code. A special version of 3DEC (3DECSP) was used for the analysis of the problem identified as slip in a jointed body induced by a harmonic shear wave. The capability of simulating nonzero cohesion and tension when discontinuity shear and/or tensile strength is exceeded was included in the special version. The results of the analyses indicate that 3DEC provides satisfactory correspondence with the conceptual models expressed in the three benchmark problems. The result also indicates that the

effect of the nonreflecting boundary condition as implemented in the 3DEC for dynamic analysis depends on the size of the domain used in the analysis.

Preparation of direct shear-test specimens and cylindrical specimens for material characterization tests is currently underway. Three direct shear specimens, twenty-two cylindrical specimens for uniaxial and triaxial compressive tests, and twenty-five disk specimens for Brazilian disk tension tests were completed. Water was used as a cutting fluid for the preparation of shear test specimens to avoid the potential of altering fracture surface mechanical characteristics. However, use of water reduces cooling and cutting effectiveness, and contributes to blade wear.

Vast amounts of data on ground motion under impulsive loading have been generated in the course of underground nuclear explosions at the Nevada Test Site, and during other field tests related to weapons performance. An important component of this information is block motion study for which velocity and displacement data along major discontinuities forming geologic blocks are recorded. Currently, a preliminary set of five field test cases for which some of the most complete data sets have been collected were selected, and attempts are being made to secure the documents containing the data. Published references for two of the five cases have been obtained, and data are currently being summarized.

The design of field instrumentation network to monitor the short- and long-term response of excavations to repeated seismic events, and the changes in water pressure in faults or other structural features in the rock mass as a result of seismic loading is underway. The instrumentation network that will be installed at the Lucky Friday Mine, Mullan, Idaho, will be coupled with the mine-wide, macro-seismic network of the U.S. Bureau of Mines.

1.5 INTEGRATED WASTE PACKAGE EXPERIMENTS

The objectives of the Integrated Waste Package Experiments (IWPE) Research Project are to critically evaluate the current material degradation data and to determine the parameters affecting long-term container-material performance. Following extensive peer review and a thorough assessment of recently available information, a new program plan for this project was completed and sent to NRC staff for review on May 23, 1990. Since the new plan is not yet approved, reporting for this period is done in accordance with Revision 1 of the IWPE program plan. The program plan is organized according to three tasks: Task 1 deals with the critical review of information available on corrosion of materials for waste-package containers; Task 2 refers to the Waste Package Experimental Program, which includes corrosion and material stability tests; and Task 3 comprises general support and reporting. The report for the third quarter of FY90 is focused on specific accomplishments within Tasks 1 and 2.

A critical review of experimental results reported by Lawrence Livermore National Laboratory (LLNL) and Cortest Columbus in the area of crevice corrosion of candidate container materials is included in Section 5.2 of this report. The review is confined to the austenitic alloys, since these materials are the current focus of our experimental program. It is concluded that limited experimental work has been performed. Future research needs are identified and discussed, emphasizing the geometry, role of environmental variables,

alloying effects and dimensions, and presence of nonmetallic components in the crevice configuration.

Experimental results obtained during this reporting period are described in Section 5.3. Initial characterization of the alloys under study continued, and the presence of iron-rich particles in CDA-613 was confirmed by scanning electron microscopy combined with energy dispersive X-ray analysis. Increased corrosion in a standard oxidizing environment was observed in the as-received nickel-based alloys (Incoloy alloy 825 and Hastelloy C-22) as a result of chromium depletion at the surface.

Localized corrosion of Incoloy alloy 825 was studied by using cyclic potentiodynamic polarization tests in simulated J-13 well water with the addition of chloride ion over a wide range of concentrations (6 to 1000 ppm). A threshold concentration of about 20 to 100 ppm for the development of localized corrosion was identified. It was concluded that crevice corrosion predominates over pitting at these low concentrations.

Hydrogen permeation tests performed in 0.1 N NaOH at 95°C resulted in values of hydrogen diffusivities for AISI 316L stainless steel, Incoloy alloy 825, Hastelloy alloy C-22, and CDA-715 comparable to values reported in the literature for similar materials. No hydrogen permeation was detected within the time frame of the tests for CDA-102 (oxygen-free high-conductivity copper). Further studies will continue in simulated repository environments, covering also hydrogen embrittlement tests.

1.6 STOCHASTIC ANALYSIS OF FLOW AND TRANSPORT

A quantitative characterization of large-scale flow and radionuclide transport through the heterogeneous unsaturated fractured rock of Yucca Mountain will be necessary to evaluate compliance with the siting criteria and performance objectives associated with the proposed Yucca Mountain high-level waste (HLW) repository (10 CFR 60.122 and 60.113.). Realistic modeling of the complex, heterogeneous flow and transport processes at Yucca Mountain will require incorporating the effects of relatively small-scale space-time variability in modeling large-scale unsaturated flow and radionuclide transport. This is one of the main objectives of the Stochastic Analysis of Large-Scale Flow and Transport in Unsaturated Fractured Rock Research Project.

The effective starting date of the project was February 2, 1990. The specific objectives of the project are to: perform a review of the literature and assess available models and data relevant to the subject site; select a global approach to model large-scale flow and transport in unsaturated fractured rock, develop submodels for incorporation into the global model, and perform large-scale simulations and participate in the validation of flow/transport models for the Yucca Mountain repository. The project is divided in three tasks. The currently active task is Task 1: "Review, Analysis, and Development of Modeling Approach," including Subtask 1, "Literature Review of Modeling Approaches"; Subtask 2, "Preliminary Data Review and Assessment"; and Subtask 3, "Selection and Initial Development of Global Modeling Approach." The project plan was recently revised to reflect changes in numerical modeling and computer-related expenditures, to include discussion of INTRAVAL test cases data, and finally to adjust total cost to available research funds. This quarterly report develops further some of the research areas already mentioned in the previous report; these include, in particular, (1) synthetic experiments and visualization of

3D unsaturated flow, (2) numerical issues related to nonlinearity, and (3) effects of statistical correlations among hydrodynamic coefficients.

1.7 GEOCHEMICAL ANALOGS

The Geochemical Analog Project is designed to provide knowledge of the state of the art in natural analog studies applied to contaminant transport. As part of this project, we will design and undertake a geochemical natural analog study of contaminant transport relevant to the proposed repository in the unsaturated zone at Yucca Mountain. Fundamental new data will be obtained to improve the understanding of particular processes and events affecting contaminant transport in unsaturated media. This natural analog research will aid validation of predictive models for geochemical transport and will provide data for time and space scales generally inaccessible in laboratory studies.

Task 1 of the project requires a review of pertinent literature and participation in a natural analog workshop. We are examining the literature for references on geochemical natural analogs using several criteria: (1) What sites have been the subjects of previous study? (2) What methods have been used and with what success? (3) What geochemical processes are amenable to natural analog study and with what degree of resolution? and (4) What sites would constitute good analogs of conditions at Yucca Mountain? Progress in Task 1 includes continued expansion of the database for the literature review and participation in the CEC Natural Analogs Working Group 1990 meeting in Pitlochry, Scotland. A poster entitled "Possible Analog Research Sites for the Proposed High-Level Nuclear Waste Repository in Hydrologically Unsaturated Tuff at Yucca Mountain, Nevada," was presented at the workshop. A draft paper summarizing the presentation was prepared for inclusion in the conference proceedings volume and comprises the substance of this report.

2. UNSATURATED MASS TRANSPORT (GEOCHEMISTRY)

by Roberto T. Pabalan and William M. Murphy

Investigators: Roberto T. Pabalan (CNWRA), Paul Bertetti (CNWRA), and William M. Murphy (CNWRA)

2.1 EXPERIMENTAL STUDIES

2.1.1 Technical Objectives

A major technical consideration in evaluating the suitability of Yucca Mountain, Nevada, as a potential repository site for HLW is the presence of thick lateral zones of zeolitic tuffs. Because of their sorptive properties, zeolites could provide important geologic barriers to migration of radionuclides away from the repository to the accessible environment. To support the NRC's HLW program, the CNWRA is conducting experimental studies on the thermodynamic and ion exchange properties of zeolites under Task 3 of the Geochemistry Research Project. These studies are designed to generate data needed to evaluate the effectiveness of zeolitic tuffs as barriers to radionuclide migration.

The work conducted during this quarter was designed to determine the kinetics of ion exchange between clinoptilolite and aqueous solutions. The initial experiments were conducted using Na-enriched clinoptilolite and aqueous solutions of potassium or calcium chloride. The results provide constraints on isotherm experiments that are planned to be conducted, as well as provide useful estimates of ion exchange rates among aqueous species in groundwater and zeolite minerals in geologic media.

2.1.2 Ion Exchange Kinetic Experiments

2.1.2.1 *Characterization and Preparation of Clinoptilolite Materials*

Published experimental data on ion exchange between clinoptilolite and aqueous solutions show that ion exchange behavior and the resultant thermodynamic quantities derived from them are sensitive to the nature of the materials used in the experiments (Pabalan and Murphy, 1990). Most ion exchange studies that have been conducted utilized specimens of zeolitized volcanic tuff because sufficient amounts of macroscopic crystals of clinoptilolite are not readily available. These tuff samples commonly contain mineral impurities such as quartz, feldspar, iron oxides, and clays.

In the previous CNWRA research program quarterly report (CNWRA, 1990), results of characterization work that have been conducted on a number of clinoptilolite-rich zeolitized tuff specimens were reported. On the basis of this work, which utilized X-ray diffraction, petrographic analysis, and scanning electron microscopy with energy dispersive X-ray spectrometry, the clinoptilolite-rich tuff specimens (sample name CDV) from Death Valley Junction, California, were chosen as run materials for the ion exchange experiments. These specimens were obtained from Minerals Research Co. (P.O. Box 591, Clarkson, New York 14430). Mineral impurities that have been identified in sample CDV include quartz, plagioclase, K-feldspar, and smectites.

The mineral clinoptilolite is isostructural with heulandite, differing principally in the cation composition and Al/Si ratio (Gottardi and Galli, 1985). Clinoptilolite is the name given to the alkali- and Si-rich end-member, and heulandite is the alkaline earth- and Al-rich variety. Clinoptilolite is substantially more stable with respect to short-term heating in the laboratory than is heulandite. Indeed, Mumpton (1960) suggested differentiation of the two on the basis of an overnight heating test at 450°C: clinoptilolite retains its crystalline structure, whereas heulandite becomes X-ray amorphous. Heating tests at 450°C were performed on the zeolitized tuff samples that were characterized previously (CNWRA, 1990). The X-ray diffraction (XRD) patterns of heated and unheated clinoptilolite-rich tuff (sample CDV) from Death Valley, California, are shown on Figure 2-1. For comparison purposes, the XRD patterns of heulandite (source locality: Poona, Maharashtra State, India) before and after heating are shown on Figure 2-2. The XRD pattern of clinoptilolite changed very little after heating, while heulandite became X-ray amorphous.

Powdered CDV material was prepared by breaking the as-received samples, which are covered with a canvas bag, into pieces less than one-third of an inch in diameter with a rock hammer and grinding these small pieces in a Spex #8000 Mixer/Mill using a tungsten carbide vial. The CDV powders were sieved into five size ranges using a Ro-Tap sieve shaker and 8-inch-diameter stainless steel sieves. The ranges were (1) 35-100 mesh (500-150 microns), (2) 100-200 mesh (150-75 microns), (3) 200-325 mesh (75-45 microns), (4) 325-450 mesh (45-32 microns), and (5) <450 mesh (<32 microns). Sieving was repeated several times to minimize the retention of clinoptilolite grains of a particular size with grains in the larger size range.

Using the 100-200 mesh size fraction, mineral impurities were separated from clinoptilolite by density separation using heavy liquid in 250 ml separatory funnels. The heavy liquid was prepared by mixing tetrabromoethane (density = 2.9672 at 20°C) and NN-dimethyl formamide (density = 0.93445 at 20°C) (Hutchison, 1974). The separation was performed twice for each batch of clinoptilolite powder, initially using a heavy liquid density of about 2.14 g/ml, and later using a density of about 2.08 g/ml. The tetrabromoethane and NN-dimethyl formamide were washed several times from the clinoptilolite with acetone. The tetrabromoethane was also recovered using liquid-liquid extraction for later reuse. To remove the acetone, the clinoptilolite powders were washed several times with deionized water in an ultrasonic bath and also soaked overnight in deionized water. The clinoptilolite was then dried for several hours at 80°C in a convection oven, and equilibrated with water vapor over a saturated NaCl solution inside a desiccator. When not being used in the experiments, the clinoptilolite was kept in the desiccator over saturated NaCl solution to maintain a constant (and equilibrium) water content in the crystal structure.

To check the efficiency of mineral separation using heavy liquids, the purified clinoptilolite (sample name CDV-P) and the heavy mineral separates (sample CDV-HS) were analyzed by XRD. The XRD patterns of CDV-P and CDV-HS are shown in Figures 2-3(a) and 2-3(b), respectively. The approximate weight percent of the minerals present in the samples are given in Table 2-1. These results indicate that clinoptilolite is separated well from other minerals in the original material. Goethite remaining in CDV-P is intimately intergrown with clinoptilolite, and was not effectively removed by density separation.

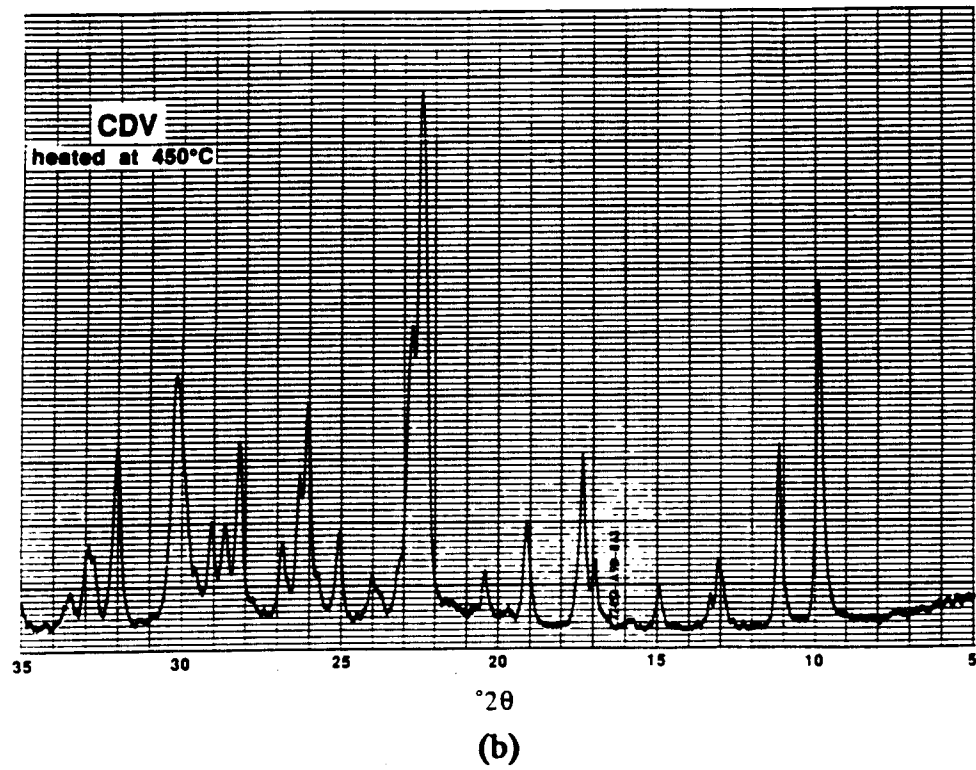
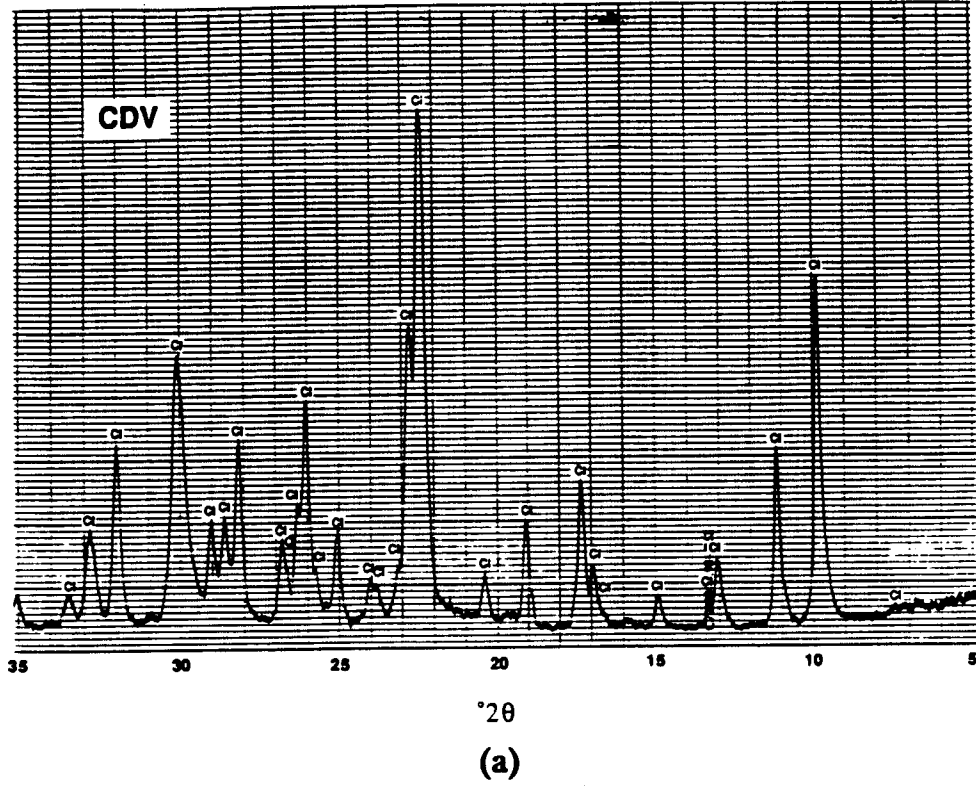


Figure 2-1. X-ray diffraction pattern of clinoptilolite-rich tuff from Death Valley Junction, California: (a) before and (b) after heating overnight at 450°C. Cl=clinoptilolite; Q=quartz.

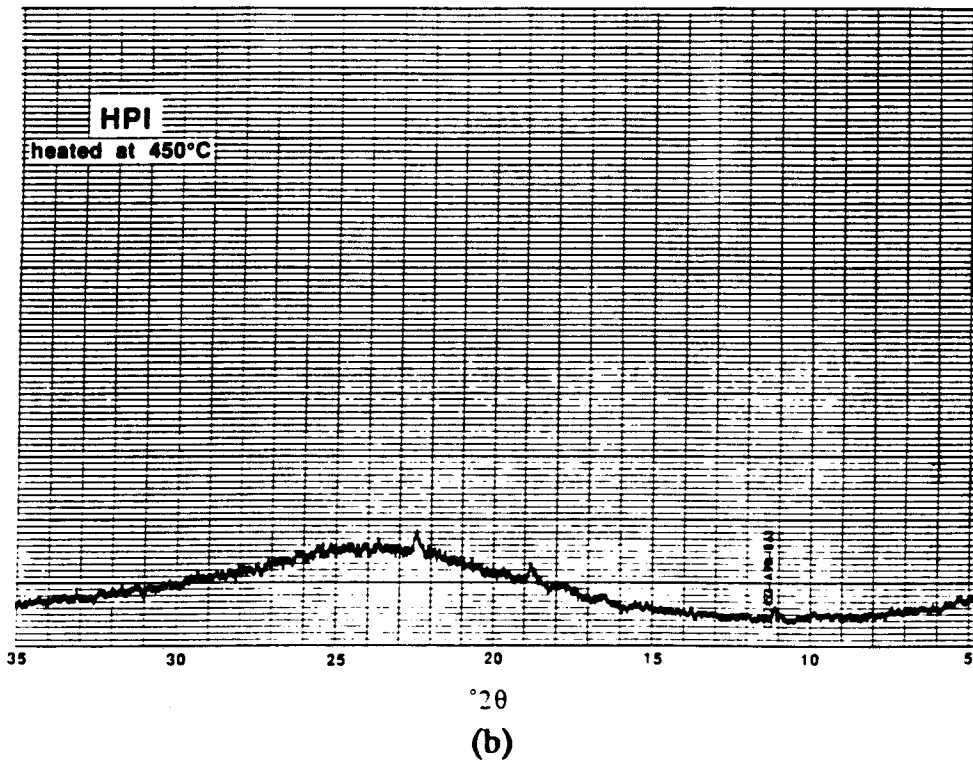
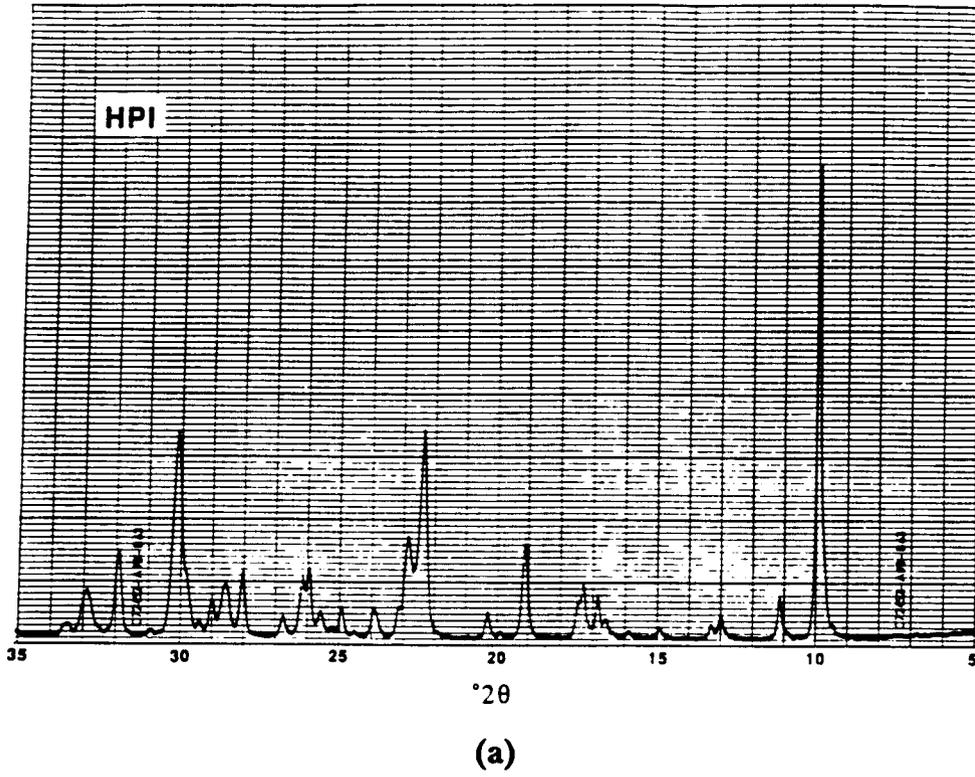
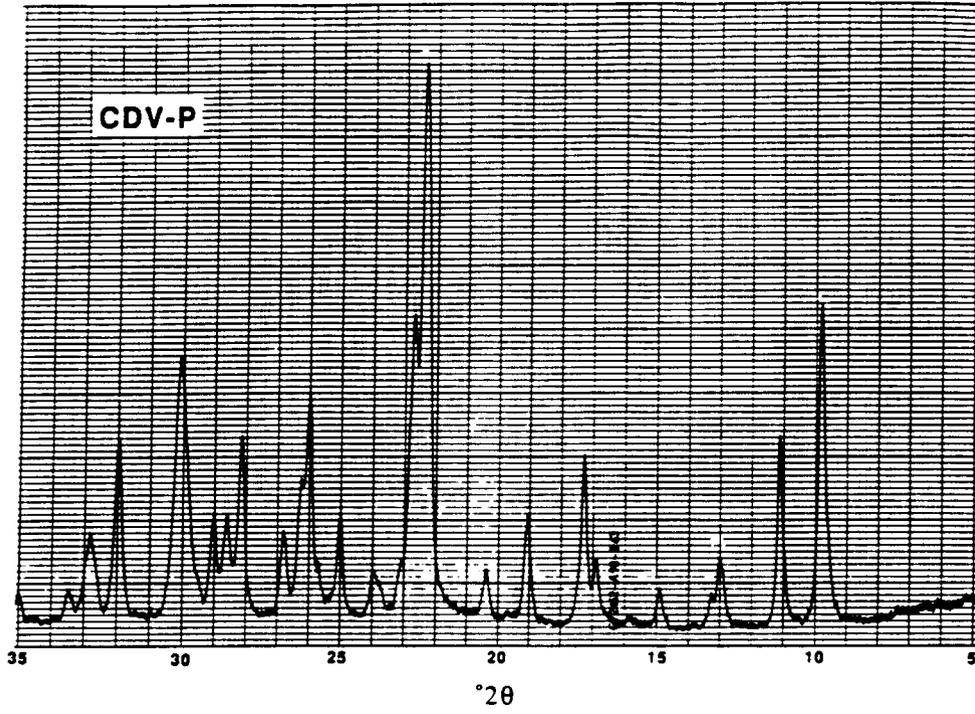
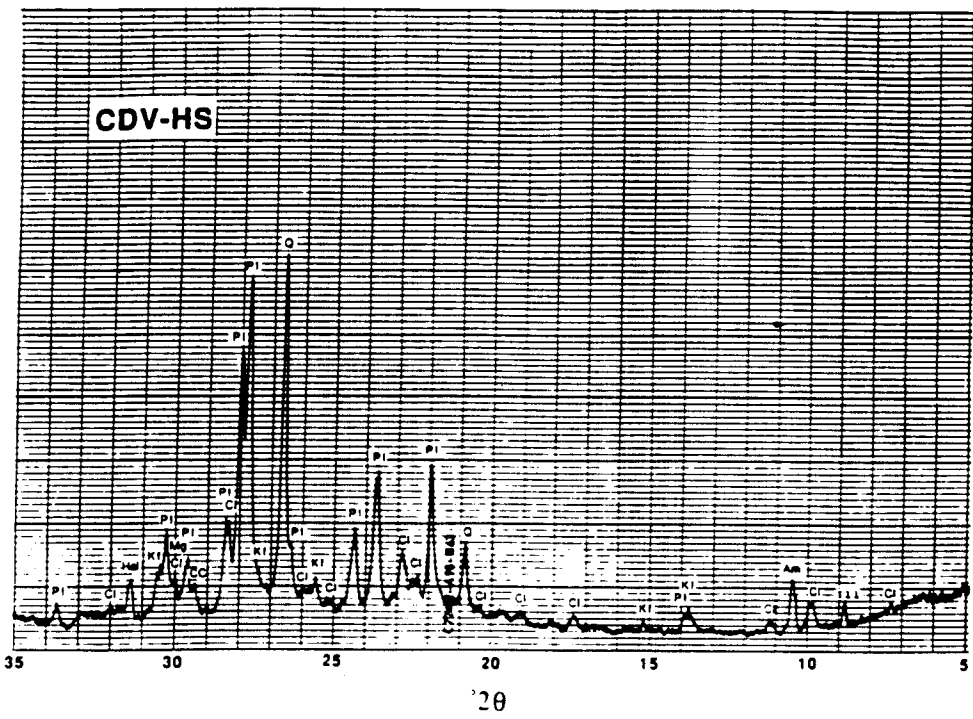


Figure 2-2. X-ray diffraction pattern of heulandite from Poona, Maharashtra State, India: (a) before and (b) after heating overnight at 450°C



(a)



(b)

Figure 2-3. X-ray diffraction pattern of clinoptilolite-rich tuff from Death Valley Junction, California, after heavy liquid separation: (a) purified material and (b) heavy mineral separate. Cl=clinoptilolite; Pl=plagioclase; CC=calcite; Q=quartz; Kf=K-feldspar; Ill=illite; Hal=halite; and Am=amphibole.

Table 2-1

**X-RAY DIFFRACTION PATTERN OF CLINOPTILOLITE-RICH TUFF FROM
DEATH VALLEY JUNCTION, CALIFORNIA**

ZEOLITIZED TUFFS	MINERALOGY, APPROXIMATE WT. %													
	QUARTZ	PLAGIOCLASE	K-FELDSPAR	MAGNETITE	GEOTHITE	CALCITE	HALITE	AMPHIBOLE	ILLITE (10Å MICA)	SMECTITE	CLINOPTILOLITE	MORDENITE	AMORPHOUS/ BELOW DETECTION	
BULK XRD SAMPLE NO.														
CDV	1	1	1		TR			TR	TR	2	86	TR?	6	Based on XRD and petrographic analyses
CDV-P					2						98		-	Based on XRD only
CDV-HS	6	30	6	12	4	6	11?	2	3		20		-	Based on XRD only
Tr = TRACE ? = TENTATIVE IDENTIFICATION														

Table 2-2

COMPOSITION OF NA-EXCHANGED CLINOPTILOLITE BASED ON ICP OR AA ANALYSIS

Reaction Time (Days)	Weight Percent (element)						
	Na	K	Ca	Mg	Fe	Al	Si
0	2.49	3.11	<0.25	0.17	0.34	5.90	30.89
2	3.99	1.48	<0.25	0.13	0.31	5.82	30.29
5	4.08	0.96	0.009	0.11	0.29	5.27	29.19
7	4.09	0.78	0.0085	0.11	0.32	5.63	28.22
9	4.40	0.67	0.0085	0.11	0.32	5.85	30.13
11	4.38	0.64	0.0069	0.11	0.25	3.41	27.94
14	4.34	0.66	0.0092	0.11	0.32	6.02	30.43

Prior to the ion-exchange experiments, Na-enriched clinoptilolite was prepared by prolonged treatment of CDV-P powder with concentrated sodium chloride solutions. The change in the composition of clinoptilolite to the more Na-rich variety was followed by taking aliquots of the solid being treated and by analyzing their composition by inductively coupled plasma emission (ICP) and/or atomic absorption (AA) spectrometry. Dissolution of the solids was done using lithium metaborate fusion. Prior to dissolution, each sample was washed thoroughly to eliminate excess NaCl, dried in the oven at 80°C, and equilibrated with water vapor over saturated NaCl solution until constant weight was attained.

The procedure for preparing Na-enriched clinoptilolite described in CNWRA Technical Operating Procedure TOP-005 (Pabalan and Murphy, 1990, p. 72-73) involves reacting clinoptilolite powder with 1m NaCl solutions at 25°C for 5 days and at 70°C for 2 days. This procedure was determined to be inadequate in achieving maximum exchange with NaCl. A modified procedure involving reacting the clinoptilolite with 3m NaCl solutions at 70°C for several days yields the results given in Table 2-2. These results are considered to be preliminary because the ICP and AA analyses utilized only two or three solution concentrations in generating the calibration curves, and the standard solutions were prepared from single-element aqueous standards. Thus the analyses did not account for possible matrix effects and nonlinearity in the calibration curves. Technical operating procedures for ICP and AA analysis using National Institute of Standards and Technology (NIST) and U.S. Geological Survey (USGS) rock and mineral standards are still being developed and tested. Nevertheless, the results in Table 2-2 indicate that maximum exchange with 3m NaCl solutions is achieved at 70°C in about 9 days. For comparison, Alietti et al. (1974) reported that nearly complete exchange between clinoptilolite and 1m

NaCl solution was achieved in 10 days at 95°C. The Na-enriched clinoptilolite was washed repeatedly with deionized water at 70°C in a shaker water bath to remove excess or imbibed NaCl, until no Cl⁻ is detected in the washings with 0.1M AgNO₃ solution.

While maximum exchange of Na for other exchangeable cations initially in the clinoptilolite appears to have been achieved in about 9 days, the results given in Table 2-2 indicate significant amounts of K, Ca, Mg, and Fe still remain in the Na-enriched clinoptilolite sample. Fe is most likely present in the goethite phase identified in the XRD pattern. K, Ca, and Mg are most probably present in other mineral phases such as K-feldspar, plagioclase, or volcanic glass. These mineral impurities are in amounts below the detection limit of the XRD method. However, these other phases are not expected to affect the results of the ion exchange experiments.

2.1.2.2 Ion Exchange Kinetic Experiments

The rate of ion exchange among clinoptilolite and aqueous solutions were studied using the Na-enriched clinoptilolite prepared above. The aqueous solutions consisted of KCl, CaCl₂, KCl+NaCl, and CaCl₂+NaCl solutions, which were prepared from ACS grade reagents and deionized water (Barnstead Nanopure II system). The experiments were conducted as follows: 50 ml of the aqueous solution of known composition were added to weighed amounts (0.2-2.0 g) of Na-enriched clinoptilolite in 60 ml polyethylene bottles. The bottles were thermostatted at 25°C, and kept under agitation using a shaker water bath (Fisher Versabath 236) set at 80 rpm. Aliquots of the aqueous solutions were taken on a periodic basis for chemical analysis for potassium, calcium, and/or sodium using ICP spectrometry or using ion-selective electrodes (ISE). The amount of solids used in the experiments, as well as aliquot volumes and dilution factors used in the sampling procedure, was adjusted so that expected changes in aqueous solution concentrations can be resolved by ICP and ISE analyses. Samples of reference solutions were also taken to determine the actual initial concentration of the solutions, to monitor their stability with time, and to check the reproducibility of the chemical analyses. Samples for ICP analysis consisted of two or five ml aliquots, which were diluted to 50 or 100 ml with 10-percent HCl + 2-percent HNO₃ matrix. ISE samples consisted of one ml aliquots which were diluted to 10 ml with deionized water. ISE analyses utilized Orion ion-selective electrodes and an Orion EA 920 pH/mV/ISE/°C meter.

The experimental results are summarized in Figures 2-4 through 2-7. In these figures, the first column of symbols represents solution concentrations determined by ISE analysis; and the second column of symbols represents concentrations determined by ICP analysis. In general, the concentrations determined by the two methods agree within analytical uncertainty (±10 percent). Figures 2-4 and 2-6 show the decrease in concentrations of K⁺ and Ca²⁺ in solution, respectively, as a function of time. Figures 2-5 and 2-7 show the increase in Na⁺ concentration in the aqueous phase with increasing time, as K⁺ or Ca²⁺ initially in solution exchanges for Na⁺ initially in the zeolite phase.

Charge balance constraints for a binary exchange reaction require that the number of equivalents of K⁺ or Ca²⁺ removed from solution equals the number of equivalents of Na⁺ released from the zeolite. Table 2-3 compares the equivalents of K⁺ or Ca²⁺ removed from the aqueous phase with those of Na⁺ released into solution. The

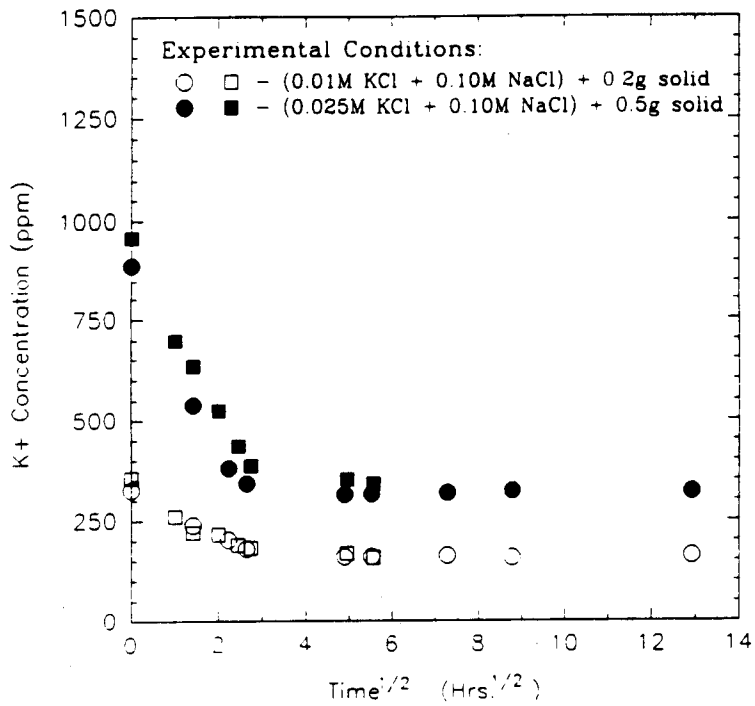
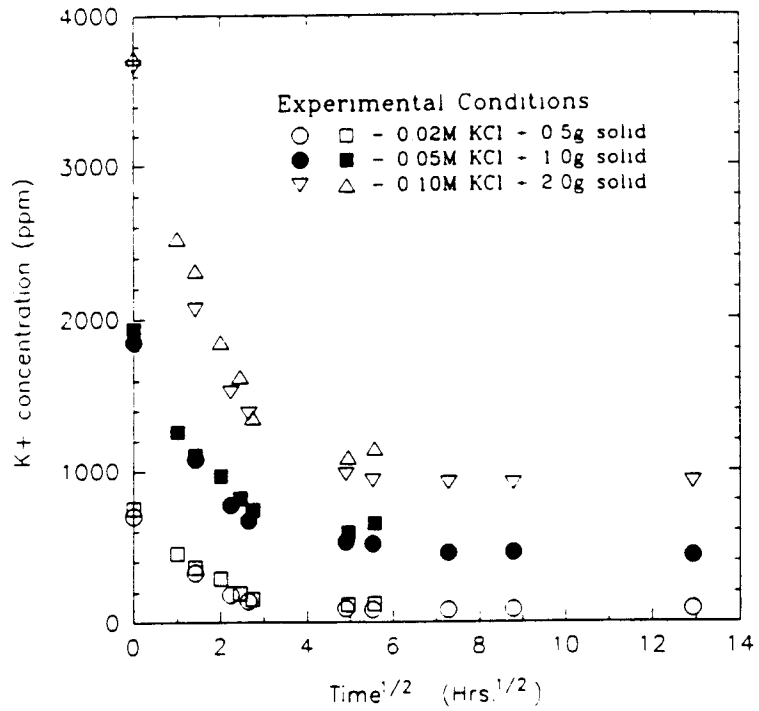


Figure 2-4. Concentration of K⁺ in the aqueous phase as a function of time

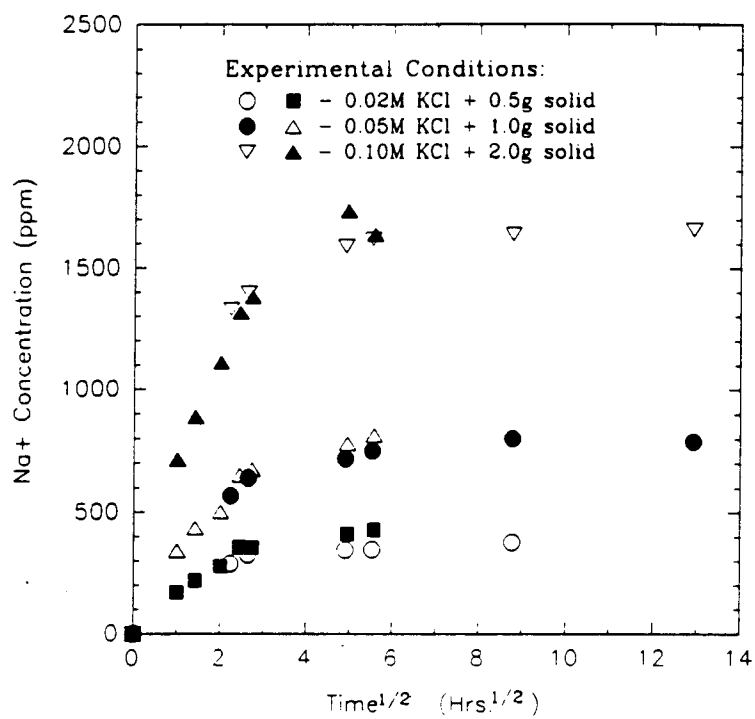


Figure 2-5. Concentration of Na⁺ in the aqueous phase as a function of time

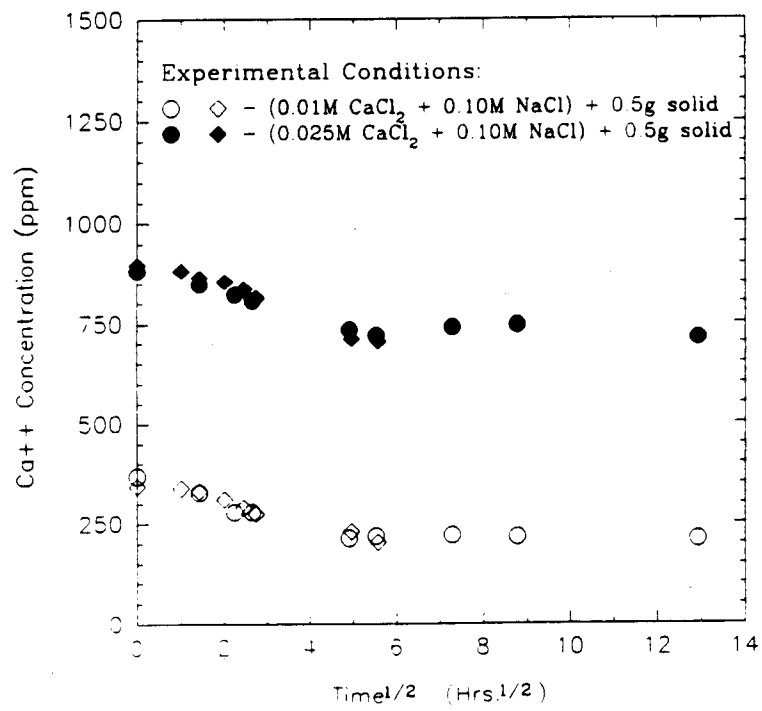
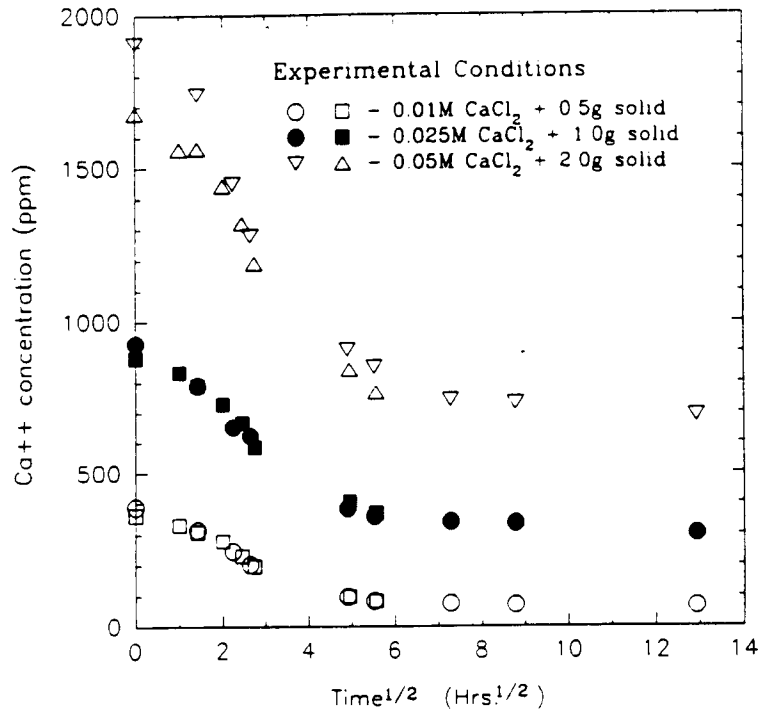


Figure 2-6. Concentration of Ca^{2+} in the aqueous phase as a function of time

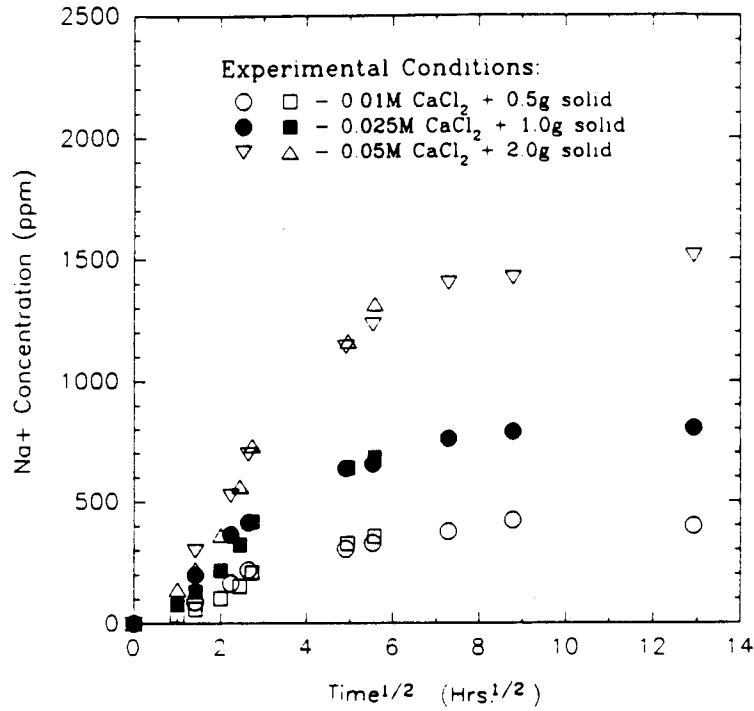


Figure 2-7. Concentration of Na⁺ in the aqueous phase as a function of time

Table 2-3

COMPARISON OF K⁺ OR Ca²⁺ EQUIVALENTS REMOVED FROM SOLUTION WITH Na⁺ EQUIVALENTS RELEASED INTO SOLUTION

Initial Solution Composition	Equiv. K ⁺ Removed	Equiv. Ca ²⁺ Removed	Equiv. Na ⁺ Released
0.02M KCl	0.0157		0.0156
0.05M KCl	0.036		0.034
0.01M KCl	0.070		0.071
0.01M KCl+0.10M NaCl	0.0042		0.0085
0.025M KCl+0.10M NaCl	0.015		0.016
0.01M CaCl ₂		0.016	0.017
0.025M CaCl ₂		0.030	0.034
0.05M CaCl ₂		0.079	0.072
0.01M CaCl ₂ +0.10M NaCl		0.008	0.012
0.025M CaCl ₂ +0.10M NaCl		0.011	0.012

values shown in Table 2-3 indicate that, except in two cases, the amount of Na^+ released into solution balances the amount of K^+ or Ca^{2+} taken up by the solid phase within analytical uncertainty. The cause of the disagreement in two of the systems studied are not certain at this point, but may be a result of matrix effects in the analytical methods used. In general, it appears that the ion exchange is essentially binary in nature, and that H^+ in the aqueous phase does not significantly participate in the exchange process. The amount of exchangeable ions other than Na^+ that may have been present in the Na-enriched clinoptilolite or in mineral impurities appears to be negligible.

The results of the preceding kinetic experiments indicate that ion exchange equilibrium for the systems studied is attained in about 2 days. The results provide constraints on the minimum amount of time required for conducting the ion exchange isotherm experiments. A minimum of 3 days will be used in the isotherm experiments that will be conducted in the next quarter.

2.2 GEOCHEMICAL MODELING

2.2.1 Technical Objective

The objective of research in geochemical modeling for the third quarter of fiscal year 1990 was to analyze and interpret data from Yucca Mountain, Nevada, to identify correlations between solid and aqueous phase chemistry that would aid the conditioning and validating of the computational models based on chemical equilibrium.

2.2.2 Introduction

Geochemical modeling commonly invokes the premise that partial and/or local equilibrium exists among minerals and aqueous solutions. Correlations between mineral and coexisting water chemistries could help validate this assumption and would help in the construction or conditioning of predictive models. Abundant water and mineral chemistry data have been collected at Yucca Mountain. However, there has been little attempt reflected in the literature to correlate the chemistry for coexisting waters and minerals. The object of this research is to identify sets of mineral and water chemistry data from the same location at Yucca Mountain, and to examine the data for correlations that may represent equilibrium controls.

2.2.3 Water Chemistry Data

Chemical data for waters extracted from wells at Yucca Mountain and vicinity were taken from the compilation by Kerrisk (1987). A major difficulty is to identify the locations, e.g., depths, from which the waters were extracted. With the exception of drill holes UE-25b No. 1 and USW H-3, all water samples are integral well samples. Two of the three water samples from UE-25b No. 1 are integral samples, and the third is taken from the 863- to 875-m depth interval in the well. Kerrisk (1987) notes that leakage probably occurred around the packing, so the interval sample is similar to the integral samples for UE-25b No. 1. The water sample from USW H-3 was taken from the 822- to 1220-m interval. Permeable, water-producing horizons have been identified for several drill

holes (Benson et al., 1983; Lahoud et al., 1984; Whitfield et al., 1985), and integral water samples from these wells may reflect the chemistry of water in these permeable zones.

2.2.4 Mineral Chemistry Data

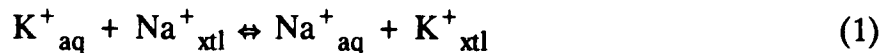
Clinoptilolite forms at Yucca Mountain primarily as an alteration product of volcanic glass by interaction with groundwater, and its chemistry is likely to reflect equilibrium with the aqueous phase. Furthermore, cation exchange reactions between water and clinoptilolite rapidly approach equilibrium under experimental conditions (e.g., Ames, 1964, and section 2.1.2 above). Therefore, chemical correlations representing equilibrium between clinoptilolite and coexisting water are likely to exist.

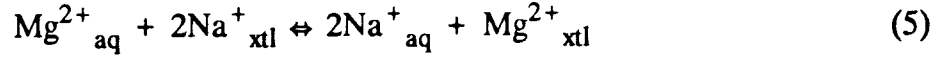
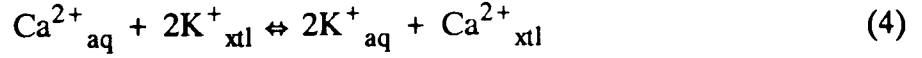
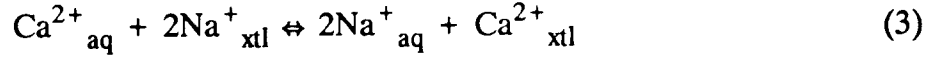
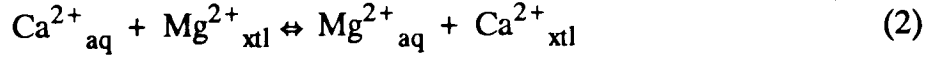
An extensive data set of compositions of clinoptilolites from bore holes at Yucca Mountain (Broxton et al., 1986) shows large variations in the Na, Ca, K, and Mg contents. It is stated generally that clinoptilolites are richer in K to the north, richer in Na and K in the west, and richer in Ca and Mg in the east of Yucca Mountain (Broxton et al., 1986). Although compositions from some individual drill holes tend to be clustered, these geographic generalizations do not apply strictly for all samples. For instance, clinoptilolites from USW G-4 span nearly the entire range of observed compositions. Groundwaters tend to be lower in Ca in the east than in the west (Kerrisk, 1987), which is consistent with the gross trend observed for clinoptilolite and suggests an equilibrium relation. In general, multiple clinoptilolite analyses for each sample depth studied are similar, and average compositions for each depth are employed for the attempted correlations given in this report.

Eleven combinations of water and clinoptilolite chemistry data were identified from tuffaceous units at Yucca Mountain that possibly represent samples with physically correlated sources. Two integral water samples from well UE-25bNo. 1, with producing zones at the 810- to 825- and 860- to 875-m depths in the upper Bullfrog Member of the Crater Flat Tuff (about 60 percent of total production) and the 480- to 650-m zone encompassing the Calico Hills Tuff and the Prow Pass Member of the Crater Flat Tuff (Lahoud et al., 1984; Benson et al., 1983), and an interval sample from the 863- to 875-m depth may be related to two clinoptilolites taken at the same well from the 863.2- and 877.5-m depths reported by Broxton et al. (1986). The product of these gives six combinations. The integral water sample from the J-13 well, with a producing zone in the lower Topopah Spring Member (approximately 282- to 450-m depth; Benson et al., 1983) of the Paintbrush Tuff, is related to three clinoptilolites at the 406.9-, 433.1-, and 441.1-m depths reported by Broxton et al. (1986) and one clinoptilolite from a fracture at 432.8-m depth reported by Carlos (1989). The water from the producing zone in the Crater Flat Tuff (600- to 900-m depth) in well USW H-4 (Whitfield et al., 1985; Benson et al., 1983) is related to a clinoptilolite from the 603.5-m depth (Broxton et al., 1986).

2.2.5 Exchange Reactions

The following six exchange reactions among Na^+ , K^+ , Ca^{2+} , and Mg^{2+} constitute a complete array of binary reactions among these species.





where aq identifies species in the aqueous phase and xtl identifies species in the crystalline (clinoptilolite) phase. The equilibrium condition for each reaction can be expressed, respectively, as

$$K_1 = \frac{a_{\text{Na}^{+}\text{aq}} a_{\text{K}^{+}\text{xtl}}}{a_{\text{K}^{+}\text{aq}} a_{\text{Na}^{+}\text{xtl}}} \quad (7)$$

$$K_2 = \frac{a_{\text{Mg}^{2+}\text{aq}} a_{\text{Ca}^{2+}\text{xtl}}}{a_{\text{Ca}^{2+}\text{aq}} a_{\text{Mg}^{2+}\text{xtl}}} \quad (8)$$

$$K_3 = \frac{(a_{\text{Na}^{+}\text{aq}})^2 a_{\text{Ca}^{2+}\text{xtl}}}{a_{\text{Ca}^{2+}\text{aq}} (a_{\text{Na}^{+}\text{xtl}})^2} \quad (9)$$

$$K_4 = \frac{(a_{\text{K}^{+}\text{aq}})^2 a_{\text{Ca}^{2+}\text{xtl}}}{a_{\text{Ca}^{2+}\text{aq}} (a_{\text{K}^{+}\text{xtl}})^2} \quad (10)$$

$$K_5 = \frac{(a_{\text{Na}^{+}\text{aq}})^2 a_{\text{Mg}^{2+}\text{xtl}}}{a_{\text{Mg}^{2+}\text{aq}} (a_{\text{Na}^{+}\text{xtl}})^2} \quad (11)$$

$$K_6 = \frac{(a_{\text{K}^{+}\text{aq}})^2 a_{\text{Mg}^{2+}\text{xtl}}}{a_{\text{Mg}^{2+}\text{aq}} (a_{\text{K}^{+}\text{xtl}})^2} \quad (12)$$

where a denotes the thermodynamic activity of the subscripted species and K stands for the equilibrium constant for the subscripted exchange reaction. It follows that equilibrium between the water and clinoptilolite requires the ratios of cation activities in the aqueous phase to be proportional to the ratios of the activities of the same cations in the solid phase where, for exchange between monovalent and divalent ions, the monovalent ion activities are squared. For example, Eq. (12) can be rearranged as

$$\frac{(a_{K^+aq})^2}{a_{Mg^{2+aq}}} = K_6 \frac{(a_{K^+xtl})^2}{a_{Mg^{2+xtl}}} \quad (12A)$$

For the purpose of examining the data for the correlations such as that predicted in Eq. (12A), it will be assumed that activity coefficients for species in the solid and aqueous phases have a secondary effect.* For species in the aqueous phase, which is dilute at Yucca Mountain, the ratio of activity coefficients for a given pair of cations will be nearly the same for all waters. Solid-phase activity coefficients represent a greater uncertainty, and could in principle lead to variability or nonlinearity in the correlations.

2.2.6 Interpretation of Data

Data for possibly coexisting waters and clinoptilolites are plotted in Figures 2-8 through 2-14 in coordinates to test the proportionalities represented in Eqs. (7) through (12). Concentrations of cations in the aqueous phase used in the calculations were in units of millimoles per liter, and concentrations of cations in clinoptilolite had units of atoms per 72 oxygens. If equilibrium proportionalities such as that expressed in Eq. (12A) are reflected by the data, and if activity coefficient ratios are not a strong function of composition, then the data should plot on straight lines with positive slopes that pass through the origin. The data for Na-Ca exchange are represented twice (Figures 2-10 and 2-11), with elimination of one spurious point in the latter plot.

The considerable scatter evident in all plots deters the objective of regressing interpretive fits to the data. Much of the scatter is due to the range of clinoptilolite compositions correlated to each water composition. A given water can coexist at equilibrium with a clinoptilolite of only one composition.** Therefore, the clinoptilolite compositional range for a given water sample indicates lack of equilibrium and/or water heterogeneity in the geologic setting. Given the poor control on the physical coexistence in nature of the water and clinoptilolite samples, and the demonstrated heterogeneity of Yucca Mountain groundwaters even within single wells, the scatter in the plots is not surprising.

*Hence, ratios of concentrations will be plotted rather than ratios of activities.

**Solid-phase immiscibility could lead to multiple clinoptilolites in equilibrium with a given water; however, the continuous range of clinoptilolite compositions observed in nature, and experimental studies of clinoptilolite exchange indicate that immiscibility is not important for the range of compositions studied here.

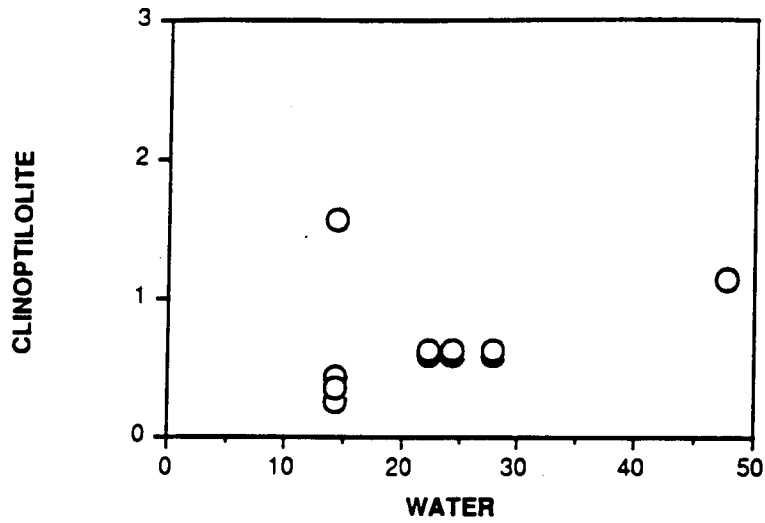


Figure 2-8. Ratio of the concentrations of Na^+ to K^+ in clinoptilolite as a function of the ratio of the concentrations (millimoles per liter) of Na^+ to K^+ in possibly coexisting water

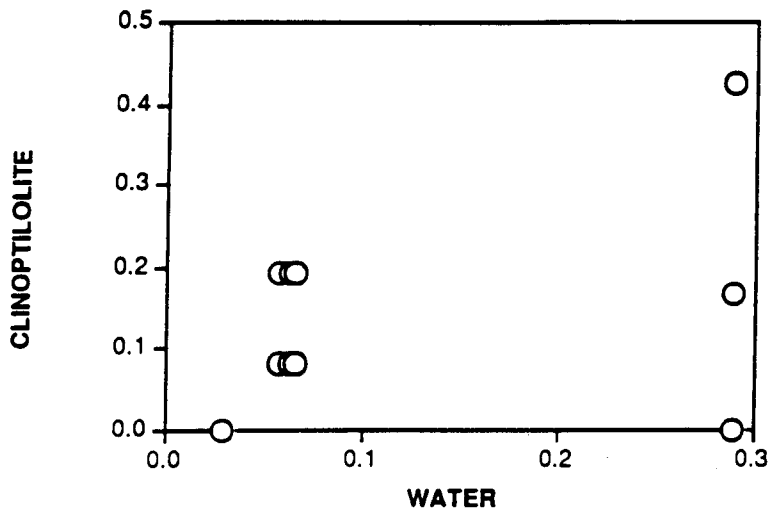


Figure 2-9. Ratio of the concentrations of Mg^{2+} to Ca^{2+} in clinoptilolite as a function of the ratio of the concentrations (millimoles per liter) of Mg^{2+} to Ca^{2+} in possibly coexisting water

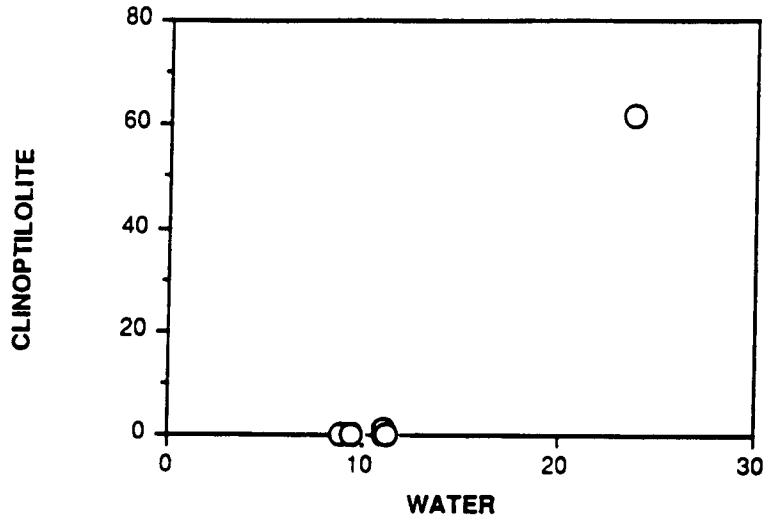


Figure 2-10. Ratio of the square of the concentration of Na^+ to the concentration of Ca^{2+} in clinoptilolite (concentrations in atoms per 72 oxygens) as a function of the ratio of the square of the concentration of Na^+ to the concentration of Ca^{2+} in possibly coexisting water (concentrations in millimoles per liter)

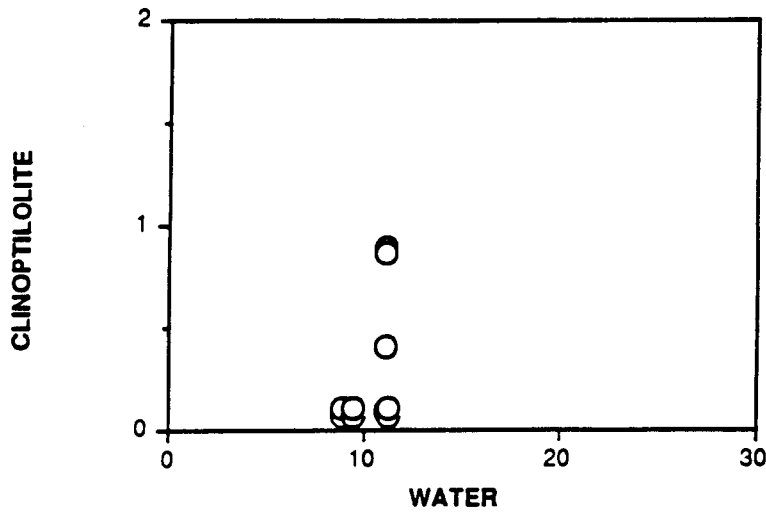


Figure 2-11. Ratio of the square of the concentration of Na^+ to the concentration of Ca^{2+} in clinoptilolite (concentrations in atoms per 72 oxygens) as a function of the ratio of the square of the concentration of Na^+ to the concentration of Ca^{2+} in possibly coexisting water (concentrations in millimoles per liter). (Note change in vertical scale.)

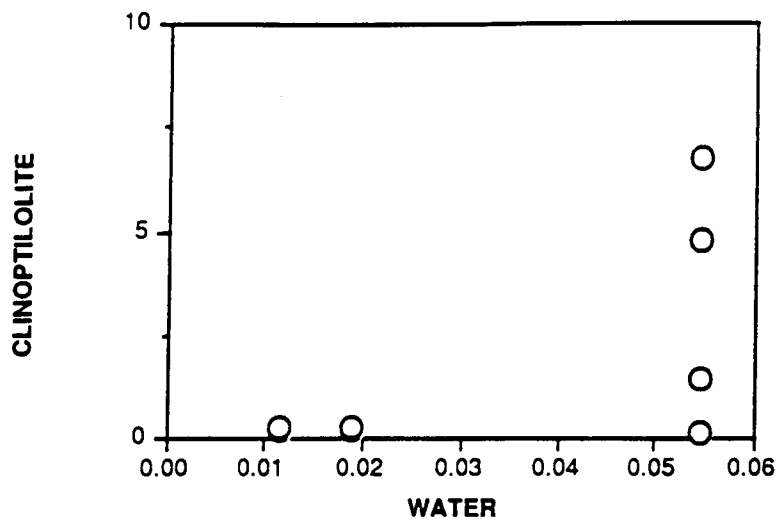


Figure 2-12. Ratio of the square of the concentration of K^+ to the concentration of Ca^{2+} in clinoptilolite (concentrations in atoms per 72 oxygens) as a function of the ratio of the square of the concentration of K^+ to the concentration of Ca^{2+} in possibly coexisting water (concentrations in millimoles per liter)

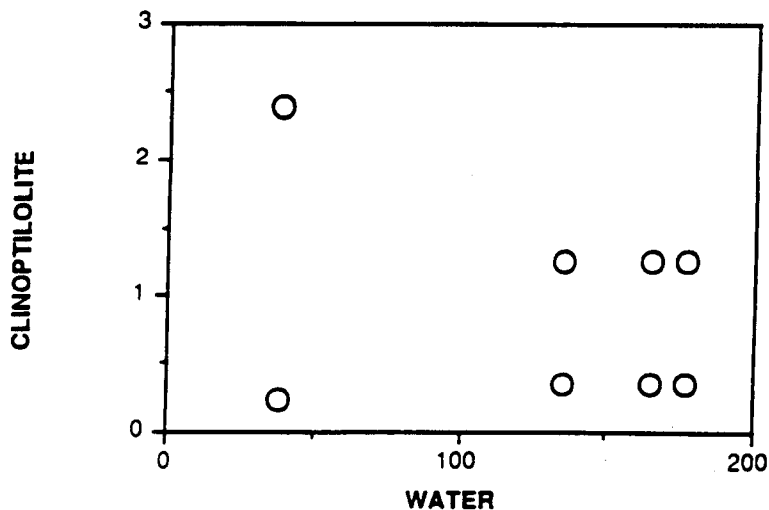


Figure 2-13. Ratio of the square of the concentration of Na^+ to the concentration of Mg^{2+} in clinoptilolite (concentrations in atoms per 72 oxygens) as a function of the ratio of the square of the concentration of Na^+ to the concentration of Mg^{2+} in possibly coexisting water (concentrations in millimoles per liter)

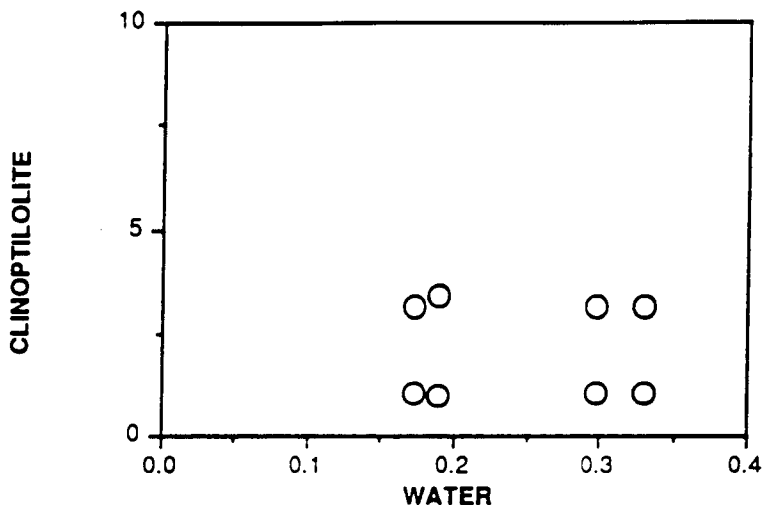


Figure 2-14. Ratio of the square of the concentration of K^+ to the concentration of Mg^{2+} in clinoptilolite (concentrations in atoms per 72 oxygens) as a function of the ratio of the square of the concentration of K^+ to the concentration of Mg^{2+} in possibly coexisting water (concentrations in millimoles per liter)

From a positive perspective, the data generally permit equilibrium interpretations within the range of compositions observed. The data for Na-K exchange (Figure 2-8) define a tight proportionality after elimination of the spurious point at Na/K for clinoptilolite greater than 1.5. The slope of a line through the remaining data and the origin would be approximately 0.02, which indicates a strong partitioning of K into the clinoptilolite. This result is qualitatively consistent with experimental data for binary Na-K exchange (Ames, 1964). Similarly, with elimination of the Mg-free clinoptilolite analyses, which seem unrealistic, the data for Ca-Mg exchange (Figure 2-9) can be interpreted to define an equilibrium proportionality with an uncertainty in the value of the proportionality constant of approximately a factor of 2. Similar permissive exchange equilibrium interpretations could be made for the data for other cation pairs.

2.2.7 Aqueous Silica Concentration and Mineralogy

A prominent mineralogic discontinuity occurs in many of the drill cores taken from Yucca Mountain. Cristobalite and clinoptilolite are found above the discontinuity, and analcime ± kaolinite are below it. This transition has been attributed to an increase in temperature with depth (Smyth, 1982) or to a decrease in the activity of aqueous silica with depth (e.g., Kerrisk, 1987). The two effects may be related. Higher temperatures lead to greater rates of quartz growth and cristobalite dissolution, which would reduce the aqueous silica activity. Correlation of water chemistry (Kerrisk, 1987) and water-producing horizons (Lahoud et al., 1984; Whitfield et al., 1985; Benson et al., 1983) with mineralogic data as a function of depth (Bish and Chipera, 1989) permits an examination of the relation between aqueous silica activity and the mineralogic discontinuity. Data for nine water

analyses from six drill holes at Yucca Mountain are shown in Figure 2-15. For this limited data set, the waters that were collected primarily from water-producing horizons above the mineralogic discontinuity generally have higher aqueous silica concentrations than waters taken from below the discontinuity. This supports the suspected relation between aqueous silica activity and mineralogy. However, plots of silica concentration versus temperature yield no clear trends.

2.2.8 Conclusions

Thermodynamic evaluation of field data compiled for possibly coexisting clinoptilolites and waters from Yucca Mountain, Nevada for consistency with cation exchange equilibrium presently yield inconclusive results. The analysis is restricted particularly because of the weak control on the locations from which water samples have been collected. An emphasis should be placed in future research on gathering chemical data on clearly coexisting mineral and water phases. In addition, the theoretical analysis is hampered by the complexity and poor understanding of the mixing properties of natural multicomponent clinoptilolite solid solutions. In general the field data presently available are too variable to permit extraction of equilibrium exchange constants. However, within the range of compositions observed, equilibrium interpretations are permissive and at least partially consistent with experimental exchange data in binary systems. As models for multicomponent clinoptilolite solutions are developed, they should be tested against these and hopefully better field data.

Clinoptilolite and cristobalite occur above analcime and kaolinite at Yucca Mountain. Waters collected from producing zones above this mineralogic transition have generally higher aqueous silica concentrations than waters collected from producing zones below this discontinuity. The limited data support the proposal that this change in mineralogy is controlled by variations in the activity of aqueous silica.

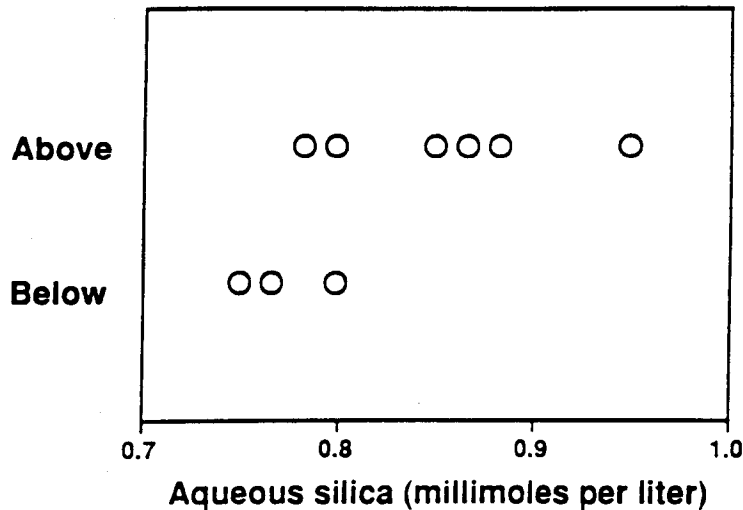


Figure 2-15. Aqueous silica concentration as a function of mineralogic environment: major water-producing horizons above and below the mineralogic discontinuity

2.3 REFERENCES

- Alietti, A., G. Gottardi, and L. Poppi. 1974. The heat behaviour of the cation exchanged zeolites with heulandite structure. *Tscherm Miner. Petr. Mitt.* 21:291-298.
- Ames, L. L. Jr. 1964. Some zeolite equilibria with alkali metal cations. *Amer. Miner.* 49:127-145.
- Bish, D. L., and S. J. Chipera. 1989. *Revised Mineralogic Summary of Yucca Mountain, Nevada.* Los Alamos National Laboratory (LANL) LA-11497-MS. Los Alamos, New Mexico: LANL.
- Benson, L. V., J. H. Robison, R. K. Rlankennagel, and A. E. Ogard. 1983. Chemical composition of ground water and the locations of permeable zones in the Yucca Mountain area, Nevada. U.S. Geological Survey (USGS) Open-File Report 83-854. Reston, Virginia: USGS.
- Broxton, D. E., R. G. Warren, R. C. Hagan, and G. Luedemann. 1986. Chemistry of diagenetically altered tuffs at a potential nuclear waste repository, Yucca Mountain, Nye County, Nevada. LANL LA-10802-MS. Los Alamos, New Mexico: LANL.
- Carlos, B. A. 1987. Minerals in fractures of the saturated zone from drill core USW G-4, Yucca Mountain, Nye County, Nevada. LA-10927-MS. Los Alamos, New Mexico: LANL.
- Carlos, B. A. 1989. Fracture-coating minerals in the Topopah Spring Member and upper Tuff of Calico Hills from drill hole J-13. LANL LA-11504-MS. Los Alamos, New Mexico: LANL.
- Center for Nuclear Waste Regulatory Analyses (CNWRA). 1990. *Report on Research Activities for the Quarter January 1 Through March 30, 1990.* CNWRA 90-01Q. San Antonio, Texas: CNWRA.
- Gottardi, G., and E. Galli. 1985. *Natural Zeolites.* New York: Springer-Verlag:409.
- Hutchison, C. S. 1974. *Laboratory Handbook of Petrographic Techniques.* New York: John Wiley & Sons:120-126.
- Kerrisk, J. F. 1987. *Groundwater Chemistry at Yucca Mountain, Nevada, and Vicinity.* LANL LA-10929-MS. Los Alamos, New Mexico: LANL.
- Lahoud, R. G., D. H. Lobmeyer, and M. S. Whitfield, Jr. 1984. Geohydrology of volcanic tuff penetrated by test well UE-25b No. 1, Yucca Mountain, Nye County, Nevada. USGS Water Res. Infor. Rept. 84-4253. Reston, Virginia: USGS.
- Mumpton, F. A. 1960. Clinoptilolite redefined. *Journal of Amer. Min.* 45:351-369.

- Pabalan, R. T., and W. M. Murphy. 1990. Progress in experimental studies on the thermodynamic and ion exchange properties of clinoptilolite. CNWRA 89-006. San Antonio, Texas: CNWRA:91.
- Smyth, J. R. 1982. Zeolite stability constraints on radioactive waste isolation in zeolite-bearing volcanic rocks. *Jour. Geology* 90:195-201.
- Whitfield, M. S., Jr., E. P. Eshom, W. Thordarson, and D. H. Schaefer. 1985. Geohydrology of rocks penetrated by test well USW H-4, Yucca Mountain, Nye County, Nevada. USGS Water Res. Infor. Rept. 85-4030. Reston, Virginia: USGS.

3. THERMOHYDROLOGY

by Ronald T. Green, Frank Dodge, and Steve Svedeman

Investigators: ^{CNWR}Ronald T. Green (SwRI), Frank Dodge (SwRI), and Steve Svedeman (SwRI)

3.1 TECHNICAL OBJECTIVES

Technical issues and uncertainties for the proposed Yucca Mountain HLW repository site indicate a need for research on thermohydrological phenomena (i.e., phenomena associated with heat and fluid flow) to provide information relevant to performance assessment and design criteria. The class of thermohydrological phenomena examined in this project includes phenomena driven by heat emanating from HLW emplaced in a geologic repository. Information derived principally from research is used to establish a knowledge base of thermohydrologic phenomena; the base will be used to assess models of processes used in performance assessments.

3.2 DESIGN AND EXECUTION OF PRELIMINARY SEPARATE EFFECTS EXPERIMENTS

Work continued on the separate effects experiments during this past quarter; and Tests 3, 4, and 5 were concluded. Parallel efforts also continued with regard to the modeling of two-phase flow through porous media as applied to the separate effects experiments.

3.2.1 Separate Effects Experimental Apparatus

Separate effects experiments Tests 3 and 4 were performed using the 23.8-in. (60.5-cm) x 26.0-in. (66.0-cm) x 3.0-in. (7.6-cm) test chamber. This was the same test chamber that was used in Tests 1 and 2. The configurations of temperature sensors and tensiometers for these tests were also the same as in the previous two tests.

The apparatus setup in Tests 3 and 4 had several differences compared with the earlier setup for Tests 1 and 2. A bolt was installed through the center of the two side walls of the test chamber to prevent the walls from bowing outward as a result from either hydrostatic pressure (for saturated material) or added weight from the water taken into the medium during wetting. The side-wall bowing was thought to have induced settling of the glass-bead medium during the Test 2 experiment.

A 0.75-in. (1.9-cm) thick sheet of styrofoam insulation was applied to the two side walls of the test chamber to inhibit heat losses through the side walls and reduce temperature fluctuations in the test chamber. The additional thickness of the apparatus caused by the insulation necessitated further separating of the densitometer source from the detector.

The media in Tests 3 and 4 were comprised of equal weights of Nos. 2740 and 1420 sieve-size glass beads. The beads were dry mixed by hand in 800-ml batches prior to being put in the test chamber. After the beads were placed in the chamber, they were packed by mechanically agitating the chamber structure with a pneumatic hammer. The

final end plate of the chamber to be installed was equipped with a flexible diaphragm that, once installed, was compressed into the medium to eliminate voids and gaps. The medium was saturated to the desired moisture content by adding a predetermined quantity of water, determined by assuming a total porosity of 37 percent of the test-chamber volume.

The last separate effects experiment (Test 5) was performed using a 5.75-in. (14.6-cm) x 8.15-in. (20.7-cm) x 0.75-in. (1.8-cm) test chamber. The two side walls of the chamber were constructed of 0.5-in. (1.3-cm) thick acrylic. A 0.75-in. (1.9-cm) thick sheet of styrofoam insulation was applied to both side walls of the test chamber to reduce heat loss and inhibit thermal fluctuations. As in the larger test chamber, this smaller sized test chamber was also fitted with heat exchangers. The two vertical walls of the test chamber contained the heat exchangers so as to permit maintaining the end walls at specified temperatures during the tests. A schematic in Figure 3-1 illustrates the design details of the smaller chamber.

Because of the small size of the test chamber, neither temperature probes nor tensiometers were installed through the side walls into the medium. However, a temperature probe was installed in the fittings of the inlets of each of the two heat exchangers.

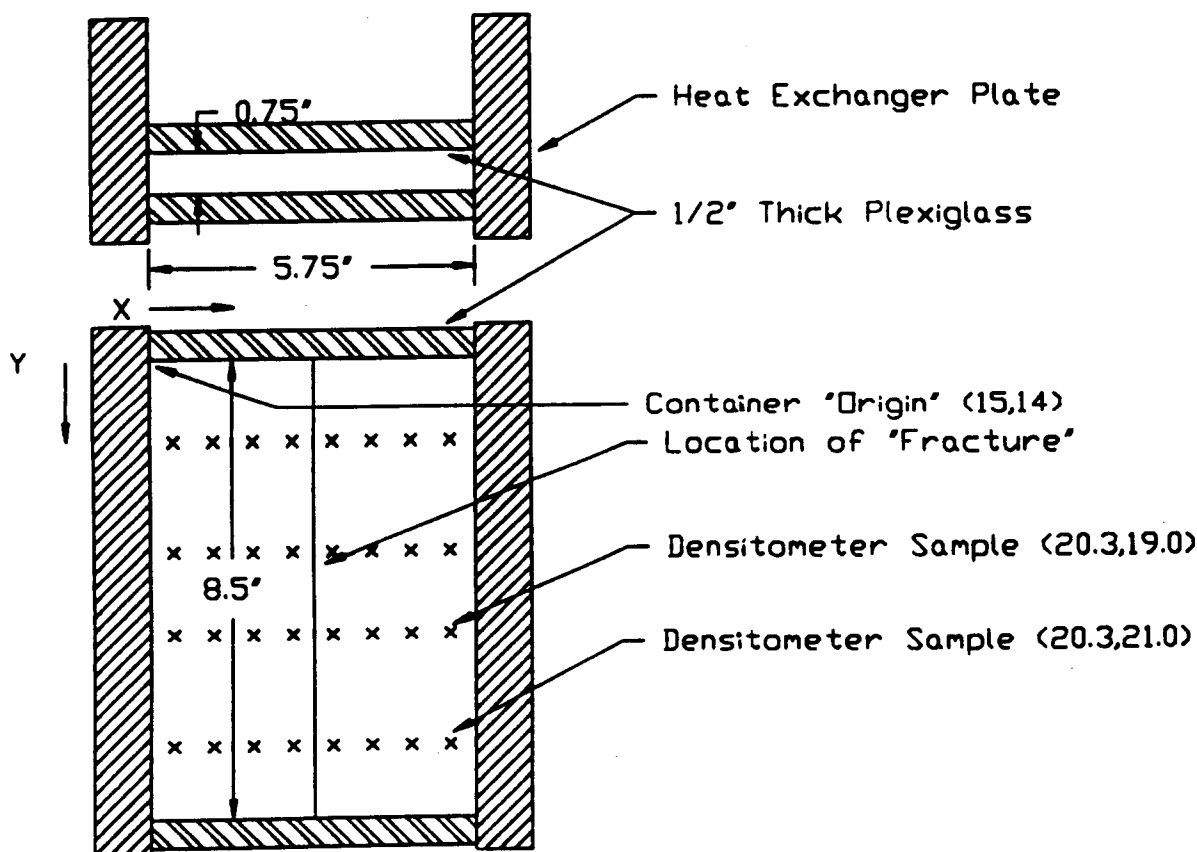


Figure 3-1. Design details of the smaller test chamber with densitometer measurement locations

Two ports (one midway up on the left and one midway up on the right and both approximately 1 inch (2.54 cm) in from the heat exchangers) were installed in the side walls of the test chamber to permit injecting either water or colored dyes into the medium. The outer ends of the ports were sealed after injection to prevent the movement of water either in or out of the chamber.

A uniform medium with a simulated fracture was used in Test 5. The medium was comprised of a mixture of equal parts of Nos. 2140 and 1420 sieve-size glass beads with a simulated fracture comprised of No. 312 sieve-size beads. The bead mixture was mixed with a predetermined amount of water to provide a medium with an approximately uniform saturation content of 60 percent. The partially saturated bead mixture was placed in the upturned chamber through the left side wall that had been removed. The moist mixture was periodically pressed into position during filling. After approximately half of the chamber was filled with the bead mixture, 2 ml of 160-micron glass beads were evenly sprinkled over the exposed medium face. Since the area of the simulated fracture is 39.3 cm², the average calculated thickness of the fracture is 500 microns. The remainder of the chamber was then filled and compacted with the moist glass-bead mixture. After the final end plate of the chamber was secured in place, the chamber was rotated to its upright position so that the simulated fracture was vertically oriented and the heat exchangers were located on the right and left sides of the chamber.

The moisture content of the medium was measured during Test 5, as in Tests 3 and 4, using a gamma-ray densitometer. The gamma-ray source of the densitometer was the same as in the previous experiments; however, a new detector was used in Test 5. The new detector was an AM-241 stabilized NaI scintillation detector (Ludlum Measurement Model 44-14) equipped with a stabilized gamma counter/scaler single-channel analyzer (Model 2200-1). Gamma-ray attenuation was measured at 32 locations in the smaller-sized test chamber. The locations of the measurements are illustrated in Figure 3-1.

Measurements from the new densitometer are presented differently than those from the old densitometer. With the old densitometer, increases in relative densitometer measurements corresponded with increases in moisture contents (greater attenuation). The new densitometer presents results more directly; increases in densitometer measurements correspond to decreases in moisture contents (less attenuation).

3.2.2 Separate Effects Experiments

3.2.2.1 Separate Effects Experiment Test 3

Test 3 was performed over a 12-day period to observe water movement in a mixture of Nos. 2470 and 2420 sieve-size glass beads under isothermal conditions. The test sequence is illustrated in Figure 3-2 and is summarized as follows:

- The densitometer scanned the glass beads several times within the test chamber prior to the introduction of water to the chamber. The purpose of this measurement was to record the attenuation of the gamma-ray beam by the test chamber and the glass beads without the influence of water and provide a baseline for subsequent measurements.

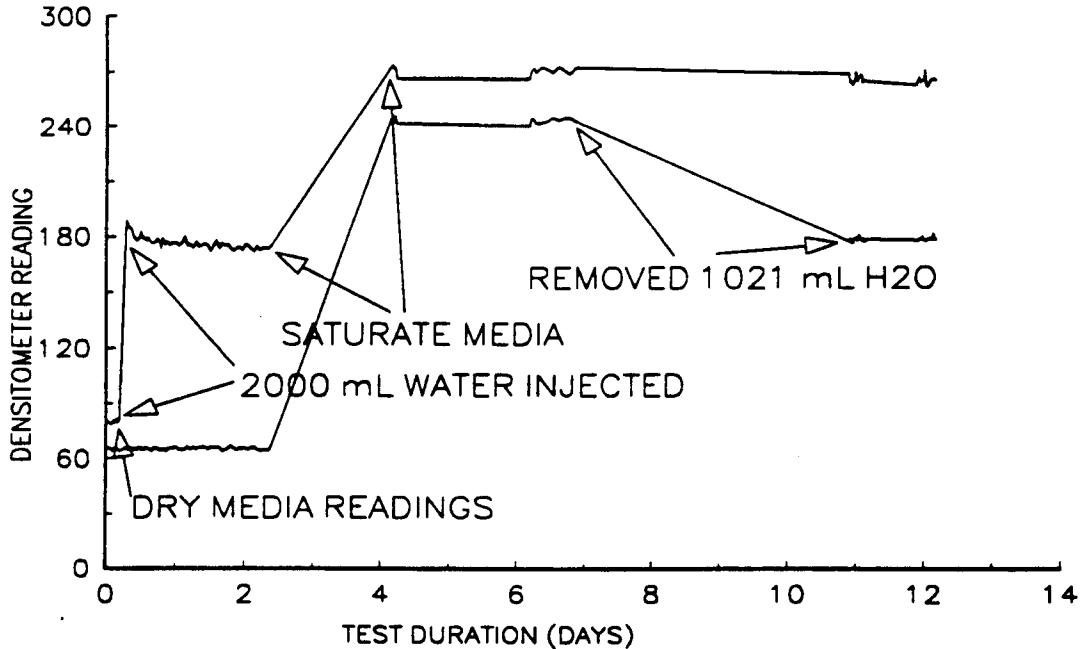


Figure 3-2. Test 3 sequence of events as measured at densitometer locations (9,6) and (9,18)

- A total of 2000 ml of deionized water was injected through a 0.13-in. (0.3-cm) tube at the port at location (13,15) (see Figure 3-2 for the x-y coordinate system) during the initial injection. The 2000 ml filled 21 percent of the void space of the medium of the test chamber.
- The water movement, suction pressure, and temperatures were monitored for a total of 2 days.
- An additional 7610 ml of water were injected into the medium. This episode of water injection was slow and required 2 days. The water was injected intermittently under a hydraulic head of 2 to 3 feet (61 to 91 cm). The medium was essentially fully saturated after injection of a total of 9610 ml of water.
- The medium was measured at full saturation with the densitometer several times over the next 3 days.
- A total of 1021 ml of water was extracted from the medium. Several methods, including applying a small vacuum (approximately 3-psi negative pressure), were used to extract the water. Four days were required to extract the water. No measurements were recorded during this period.

The ambient temperature and barometric pressure recorded during the experiment are presented in Figure 3-3. The temperatures recorded within the test chamber are illustrated in Figure 3-4. The tensiometer readings for Test 3 are illustrated in Figure 3-5, and the densitometer readings for Test 3 at selected locations are illustrated in Figure 3-6. The densitometer measurements are expressed in terms of relative counts with baseline readings at zero and 100-percent saturation. Increases in densitometer readings correspond to increases in moisture levels.

3.2.2.2 *Separate Effects Experiment Test 4*

Test 4 was performed over a 23-day period to monitor water movement in a partially saturated medium under nonisothermal conditions. The intact test chamber and medium remaining after the termination of Test 3 were used in Test 4. The test sequence recorded using the temperature sensors is illustrated in Figure 3-7 and is summarized as follows:

- At commencement of the test, the temperature of the top heat exchanger was set at 60°C using fluid circulated from a constant-temperature heat bath, while the temperature of the lower heat exchanger was maintained at approximately 20°C using circulating tap water. Therefore, the imposed temperature gradient was 0.66°C/cm.
- The temperature, suction pressure, and moisture content of the test chamber were monitored for a total of 3 days.
- The imposed temperature regime was reversed by setting the temperature of the bottom heat exchanger at 60°C and the top heat exchanger at 20°C. The temperature gradient for this setting was also 0.66°C/cm.
- At days 6, 8, and 9 of the experiment, the temperature of the lower heat exchanger was increased to 80°C, 95°C and 105°C, respectively, while the top heat exchanger was maintained at 20°C. The temperature gradients for these three settings were 1.0°C/cm, 1.2°C/cm, and 1.4°C/cm, respectively.
- At day 9 and prior to setting the temperature to 105°C, approximately 20 ml of red dye (food coloring) was injected at location (13,15) to help visualize the movement of water.
- At day 15, the constant-temperature water bath was turned off, but circulation of the fluid continued during the cooldown period.
- At day 20, the constant-temperature water bath was removed, and tap water at approximately 20°C was circulated through the lower heat exchanger.
- The temperature, suction pressure, and moisture content were measured and recorded until the experiment was terminated at day 23.

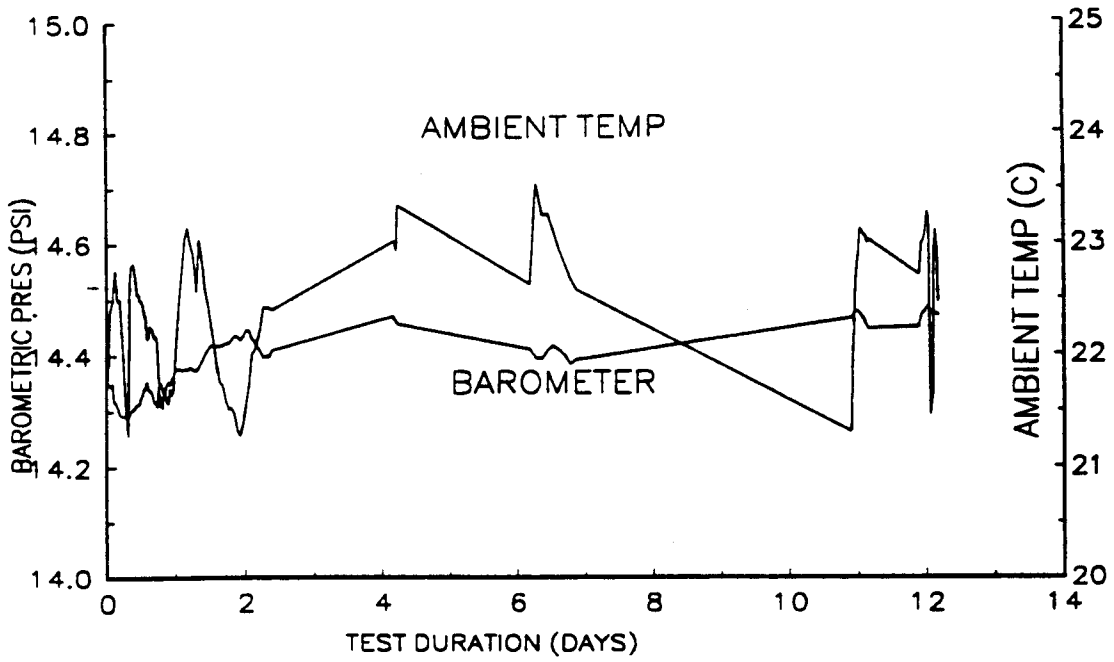


Figure 3-3. Ambient temperature and pressure during Test 3

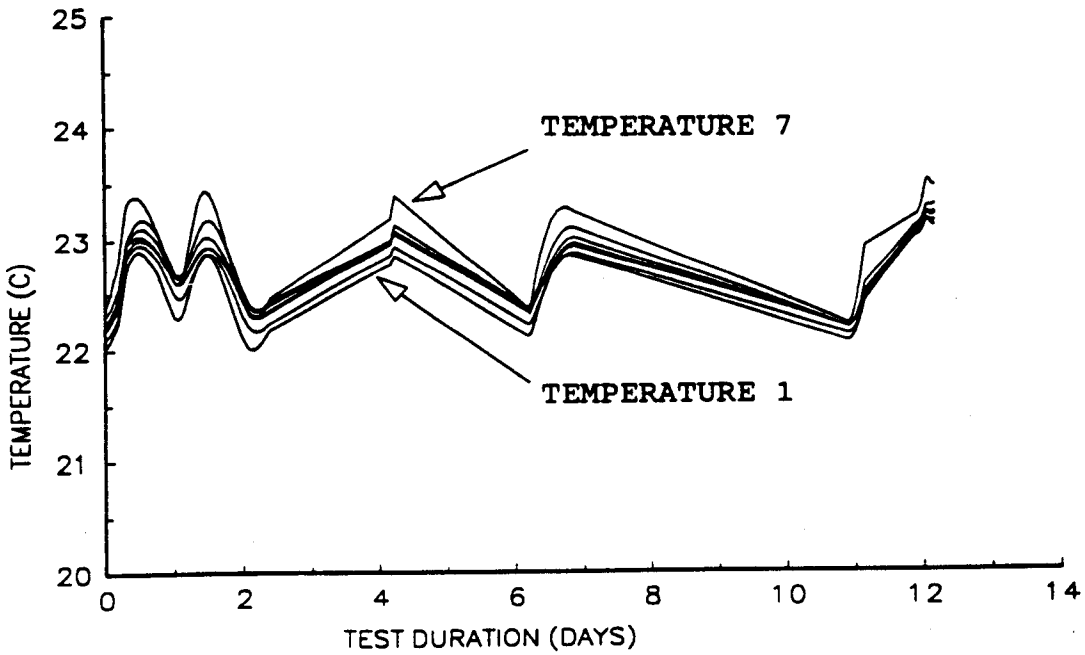


Figure 3-4. Temperature measured in the test chamber during Test 3

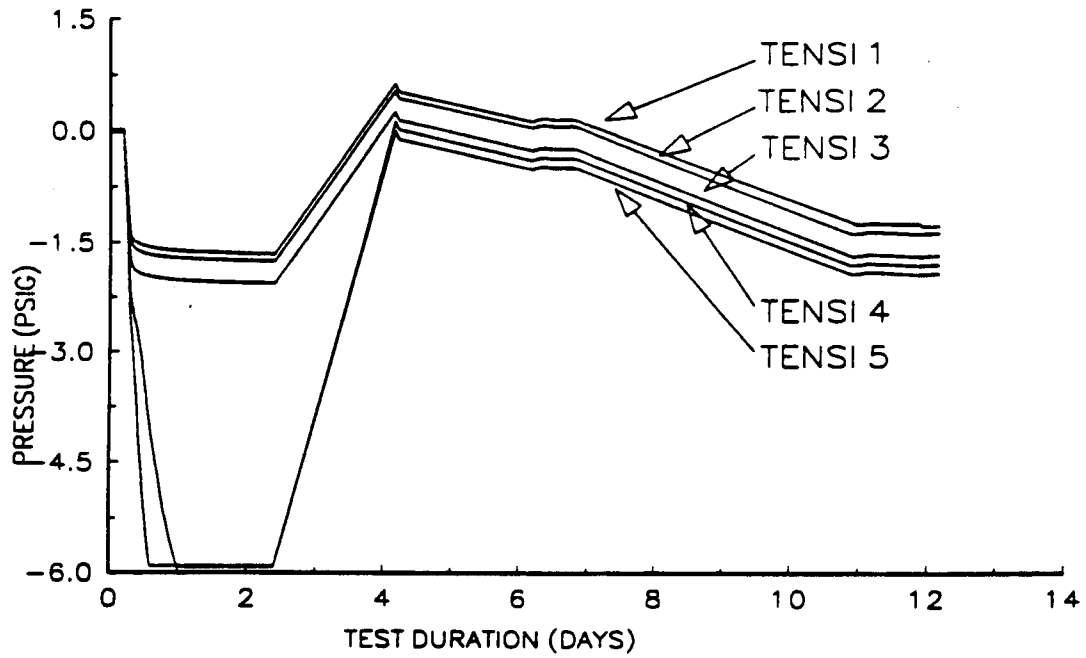


Figure 3-5. Tensiometer measurements during Test 3. Pressure is measured relative to barometric pressure.

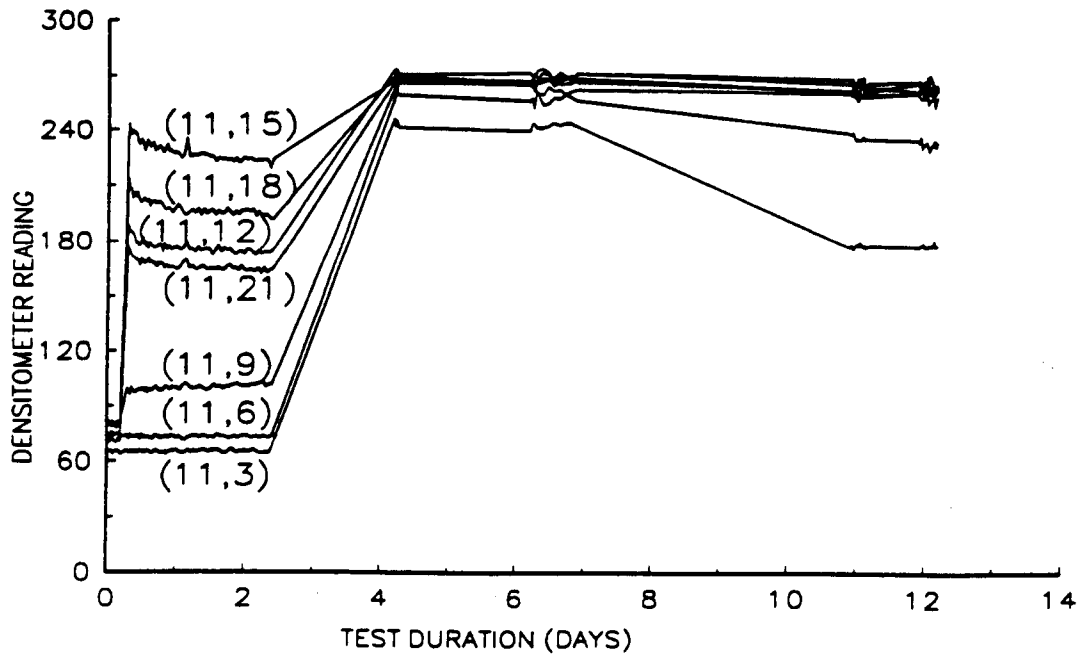


Figure 3-6. Densitometer measurements from Test 3 at locations (11,3) through (11,21)

The ambient temperature and barometric pressure recorded during the experiment are presented in Figure 3-8. The temperatures recorded within the test chamber are illustrated in Figure 3-7. The suction pressures measured relative to barometric pressure are illustrated in Figure 3-9. The densitometer measurements readings (expressed in terms of relative counts) for Test 4 at selected locations are illustrated in Figure 3-10. Increases in densitometer readings correspond to increases in moisture levels.

3.2.2.3 *Separate Effects Experiment Test 5*

Test 5 was performed over a 40-day period to monitor water movement under nonisothermal conditions in a partially saturated medium with a simulated fracture. The medium was a mixture of Nos. 2740 and 1420 sieve-size glass beads, and the simulated fracture was comprised of No. 812 sieve-size glass beads. The test sequence, illustrated in Figure 3-11, is summarized as follows:

- The test was started by taking densitometer readings for one-half day with a dry bead mixture in the container. After the dry bead mixture was removed, the premixed 60-percent saturated bead mixture was packed into the container and monitored with the densitometer until day 5.5.

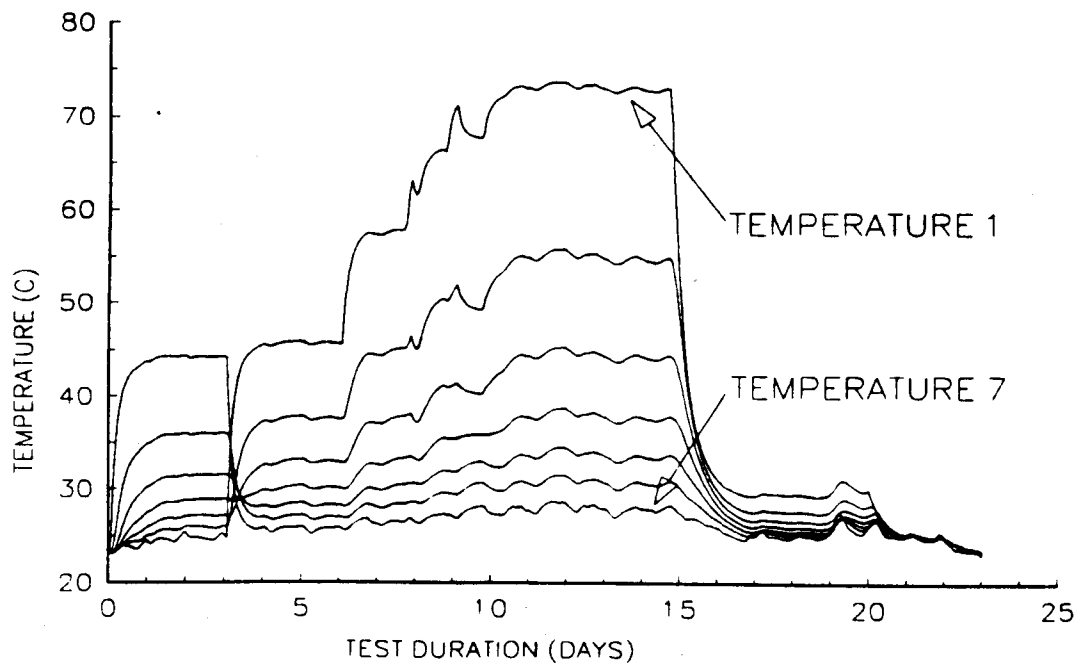


Figure 3-7. Test 4 sequence of events as measured at the temperature sensor locations

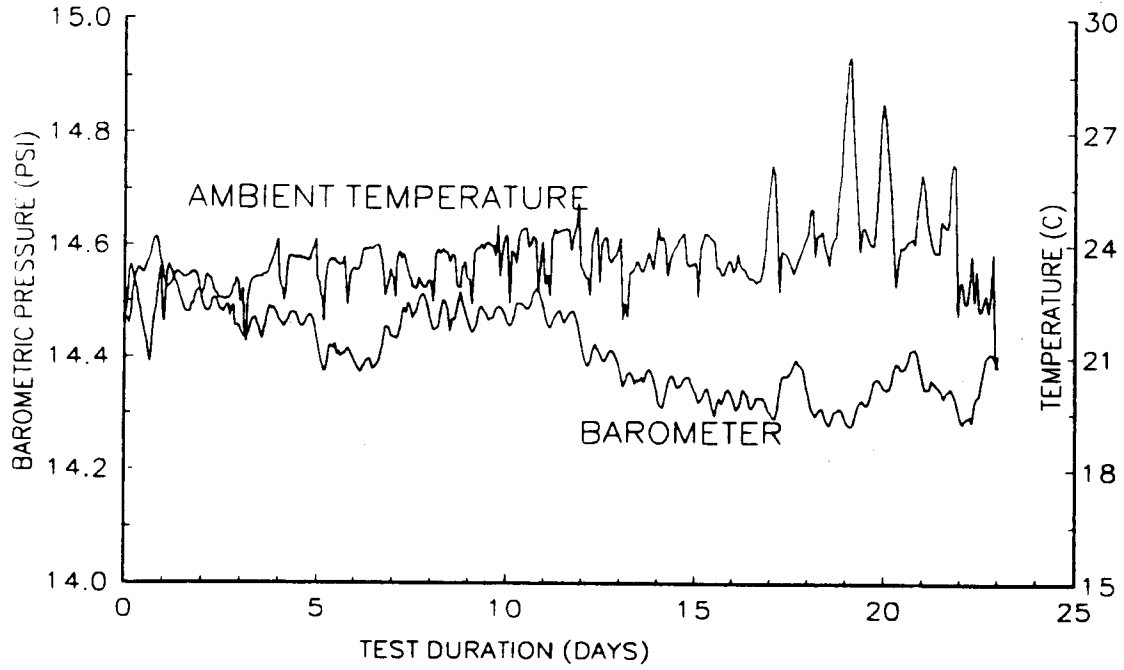


Figure 3-8. Ambient temperature and pressure during Test 4

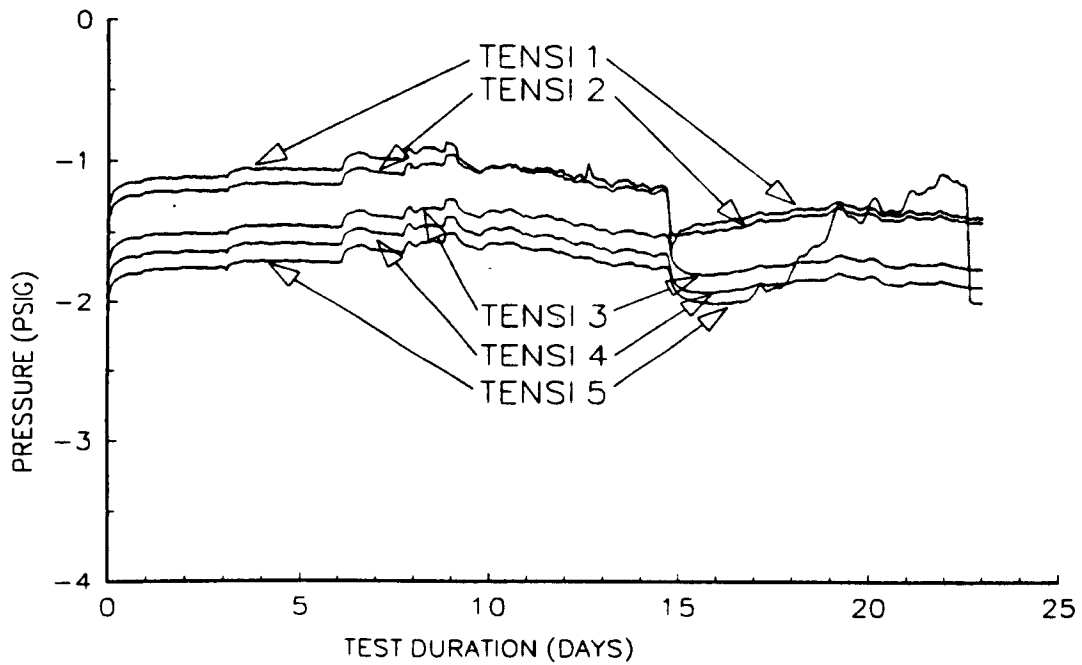


Figure 3-9. Tensiometer measurements during Test 4. Pressure is measured relative to barometric pressure

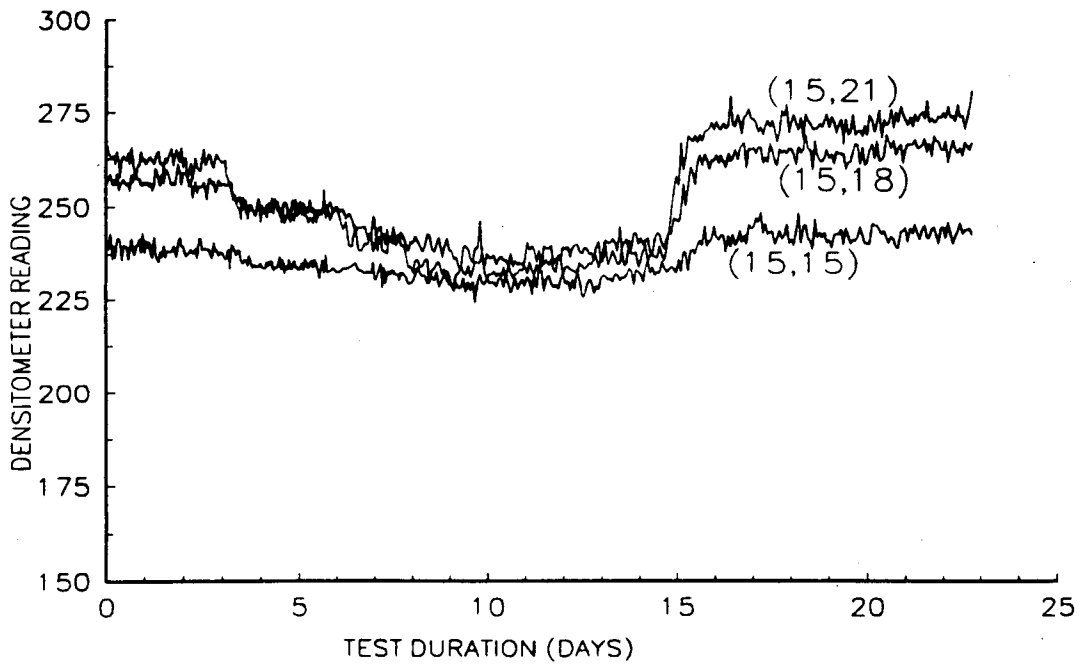
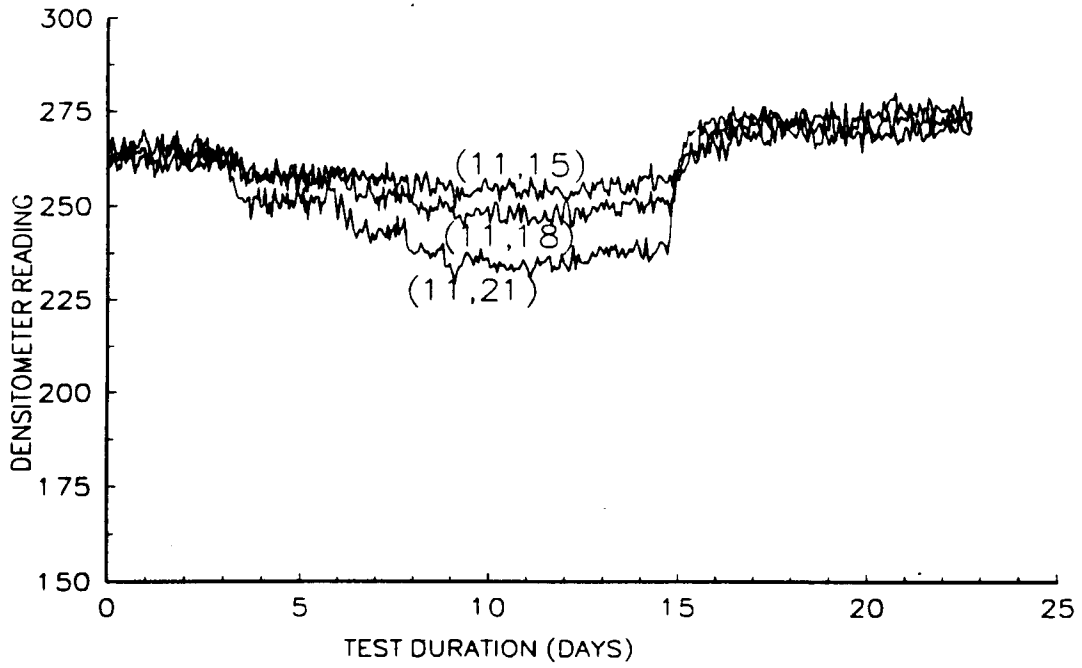


Figure 3-10. Densitometer measurements from Test 4 at locations (11,15), (11,18), and (11,21) and at locations (15,15), (15,18), and (15,21)

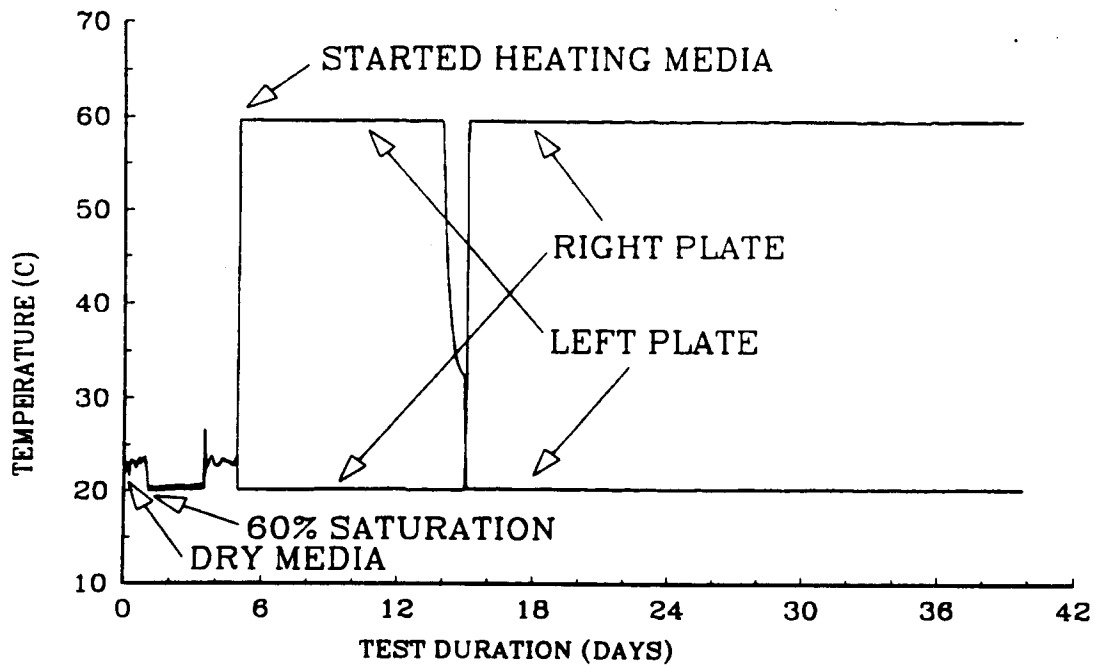


Figure 3-11. Test 5 sequence of events as measured at the two heat-exchanger temperature sensors

- At day 5.5, the heat exchanger on the right was held at 20°C, and the heat exchanger on the left was set to 60°C, both using fluid circulated from constant-temperature heat baths. The imposed temperature gradient was 2.7°C/cm.
- The temperatures at the inlets to the heat exchangers and the moisture content within the chamber were monitored for 3 days.
- Approximately 2 ml of red dye and 2 ml of blue dye were injected with a syringe into the medium through the right and left ports, respectively. The blue dye was Mrs. Stewart's Bluing, and the red dye was food coloring.
- Photographs were taken of the dye movement as seen on the front face of the test chamber. They were made at various periods throughout the duration of the test to help monitor water movement through the medium. The styrofoam layer was removed for short periods of time when the photographs were taken. A small dot of tape was placed on the front face of the chamber at the two points of dye injection for reference.
- At day 13 of the experiment, the water bath connected to the left heat exchanger was turned off; and the temperature was allowed to cool for 1 day.

- The temperature of the right heat exchanger was then raised to 60°C, and the left was set to 20°C. Additional blue dye (food coloring this time) was injected into the right port at the time the right heat exchanger was raised. The imposed temperature gradient was 2.7°C/cm.
- Additional red dye was injected into the left port after 14 days into the experiment.
- The temperatures of the two heat exchangers and moisture content were monitored for the duration of the experiment until it was terminated after 39 days. Photographs also were taken over the duration of the experiment.

The ambient temperature and barometric pressure recorded during the experiment are presented in Figure 3-12. The temperatures recorded at the inlets of the two heat exchangers are illustrated in Figure 3-11. Photographs illustrating the movement of the dyes at days 7, 14, and 23 of the experiment are illustrated in Figures 3-13 through 3-15, respectively.

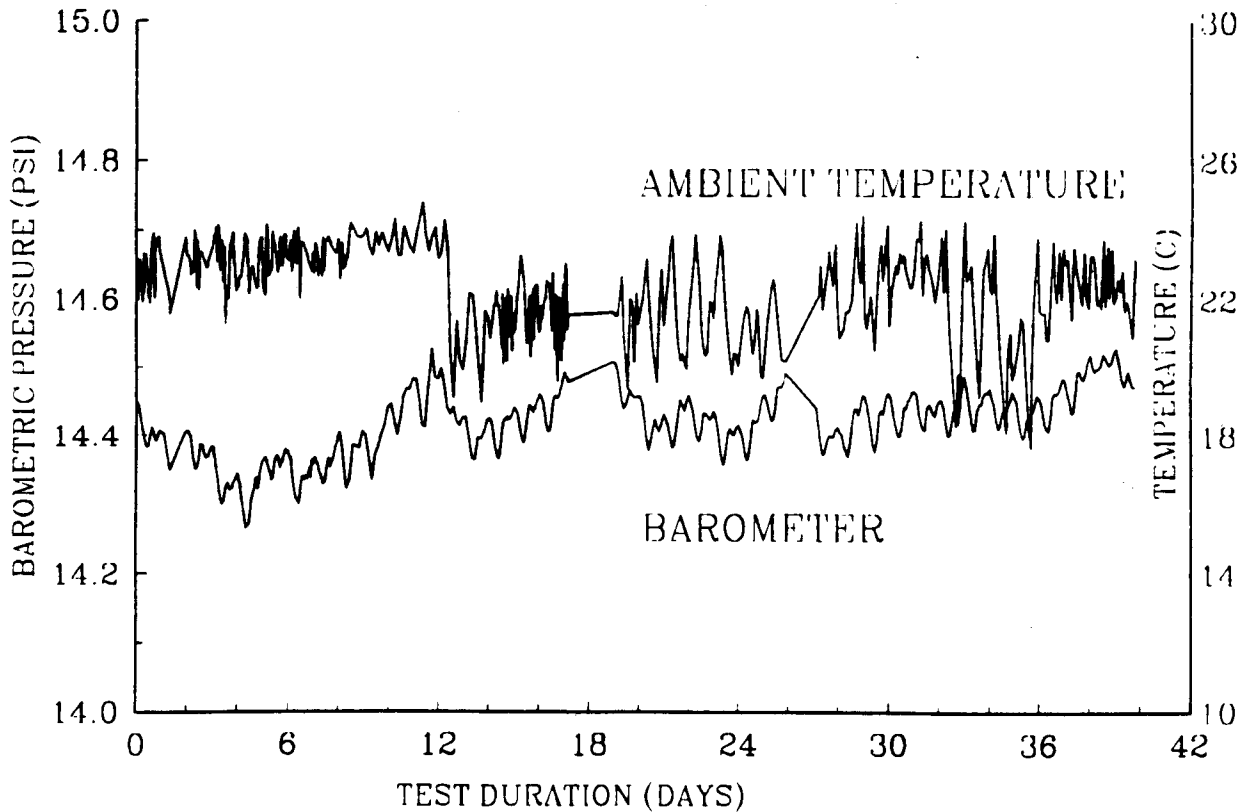


Figure 3-12. Ambient temperature and pressure during Test 5

3-13

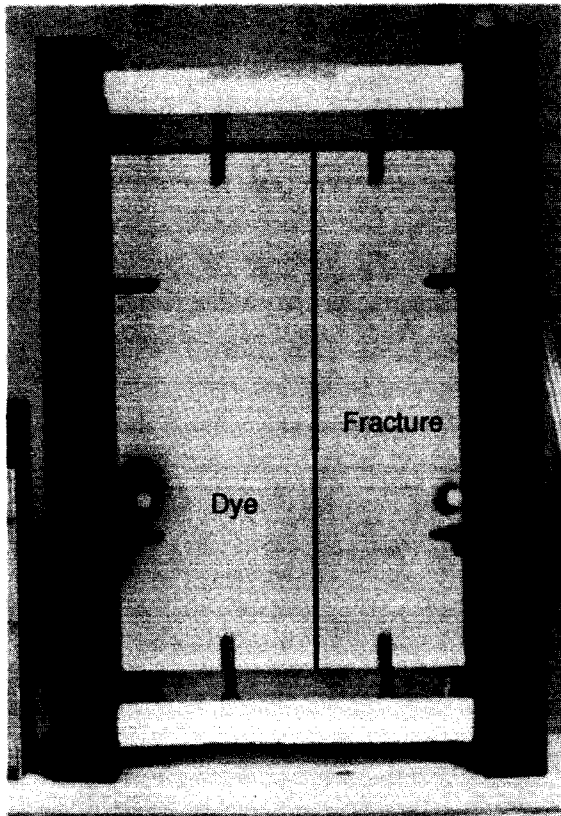


Figure 3-13. Photograph of the test chamber at day 7 of Test 5

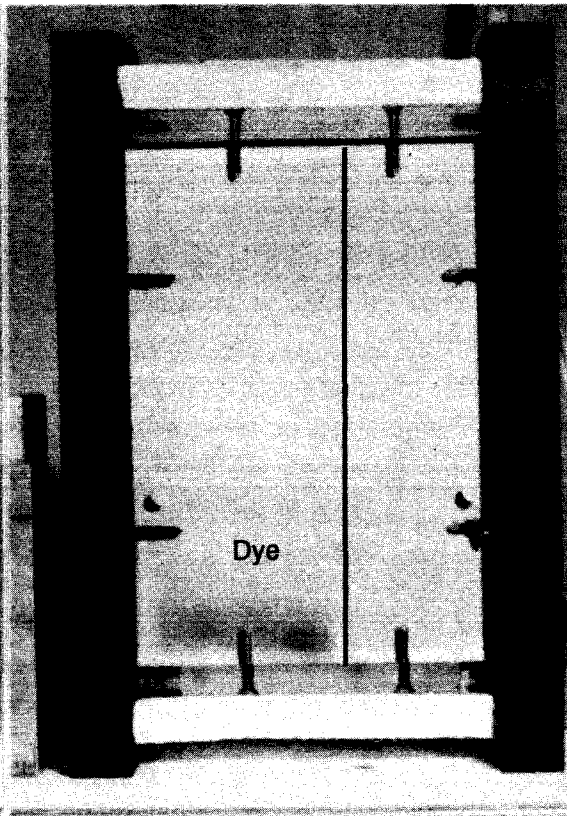


Figure 3-14. Photograph of the test chamber at day 14 of Test 5

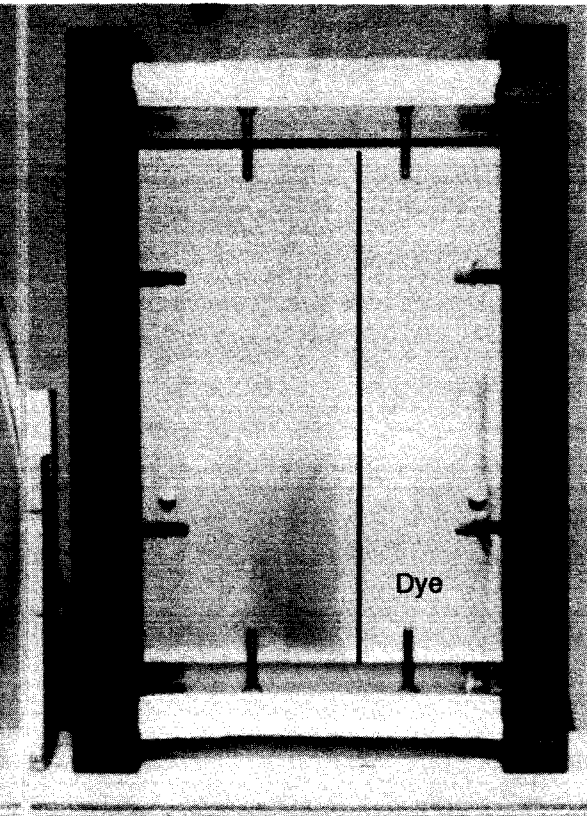


Figure 3-15. Photograph of the test chamber at day 23 of Test 5

3.2.3 Separate Effects Experiments Results

3.2.3.1 Results of Separate Effects Experiment Test 3

The ambient temperature varied by about 2°C (from about 21°C to 23°C) over the duration of the experiment. This compares to the slightly smaller fluctuation in temperature of 1.5°C (from about 22°C to 23.5°C) monitored within the medium. The slightly higher temperature in the medium relative to the ambient temperature is possibly attributable to radiative heat absorbed by the anodized aluminum heat exchangers or to the location of the ambient temperature sensor below the test section and closer to the cooler floor.

The visible extent of moisture infiltration at the time of injection and 2 days after injection is illustrated in Figure 3-16. The decrease in water content at the upper portion of the visible water pattern concurs with decreased densitometer readings at locations (11,9), (11,15), and (11,18) over the same time period (days 1 through 3) (Figure 3-6).

3.2.3.2 Results of Separate Effects Experiment Test 4

The ambient temperature fluctuated about 8°C (from about 21°C to 29°C) over the duration of the experiment. The fluctuations at day 8.5 and 10 in Test 4 (especially at temperature-sensor locations 1, 2, and 3, located closest to the higher temperature heat exchanger) are attributed to periods when the styrofoam insulation fell off the front of the test chamber.

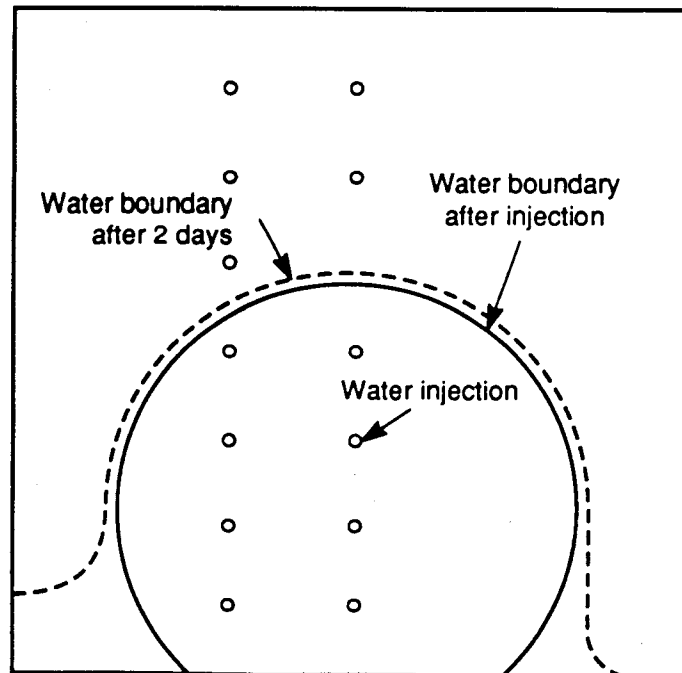


Figure 3-16. Extent of moisture infiltration at day 2 of Test 3

The temperature fluctuations at days 19 and 20 (during the period after the heat sources were removed from the experiment) are attributed to high ambient temperatures that occurred at these times.

Movement of water in response to changes in temperature after the heat source was removed is illustrated in the densitometer readings recorded at locations (11,15), (11,18), and (11,21) [Figure 3-10(a)] and at locations (15,15), (15,18), and (15,21) [Figure 3-10(b)]. At day 4 (when the temperature of the lower heat exchanger was set above the upper heat-exchanger plate), the densitometer plots illustrate decreasing local saturation levels. As the temperature of the lower plate was further increased on days 6, 8, and 9, the local saturation continued to decrease. When the heat was removed from the lower heat-exchanger plate at day 16, the densitometer plots [Figures 3-10(a) and (b)] illustrated the saturation returning to the preheated levels.

3.2.3.3 Results of Separate Effects Experiment Test 5

The movement of the colored dyes proved to be the most useful information collected during Test 5. Although general moisture-content trends can be made using the densitometer measurements, the resolution of the densitometer measurements is not sufficient to provide quantitatively significant data for evaluation purposes.

Major shortcomings of the densitometer method in Test 5 were the narrow depth of the test chamber, thermal fluctuations in the environment where the test was conducted, and density differences in water attributable to temperature. The most significant of these shortcomings was the narrow depth (3/4 in.) of the test chamber. Since the porosity of the Nos. 2740 and 1429 sieve-size glass-bead mix used in Test 5 is about 31 percent, full saturation of the medium would constitute about a quarter-inch depth of water. Therefore, the densitometer would be required to resolve minor quantities of total water for the water-content measurements to be significant. This proved to be beyond the capabilities of the densitometer used in this experiment.

The observed movement of the colored dyes provided a visual expression of the liquid moisture movement within the medium. The movement of water vapor was not monitored in this experiment. As observed with the dye, the induced fracture had a pronounced affect upon the flow paths of water in the medium. In particular, liquid water had little movement across the fracture as evidenced by the dyes. Two flow cells were created whose boundaries were comprised of three sides to the test chamber and the induced fracture. The circulation direction of the flow cells did not initially follow the direction that appeared to be intuitively correct. Upon commencement of the experiment, the direction of the water flow was downward along the face of the heat exchanger. Intuitively, it was thought that water proximal to the heated surface would rise until encountering the top of the chamber, then move inward until encountering the induced fracture. Contrary to this early hypothesis, the initial direction of flow was downward along the face of the heat exchanger until arriving at the lower end of the test chamber, then toward the interior of the chamber.

Movement of water across the induced fracture was not noted until late in the test when the half of the medium near the higher temperature heat exchanger

visibly began to dry and the material on the other side became visibly wetter. Some movement of the red dye (and presumably some water) was observed crossing the fracture when the moisture content of the cooler half of the medium became high enough to wet the pores of the larger-pored fracture.

3.3 SIMULATION EXPERIMENTS

The movement of liquid water, water vapor, and heat through fractured, porous media is being simulated using the TOUGH code. Physical processes observed during the implementation of separate effects experiment Test 5 will be simulated, if possible, using the TOUGH code.

The code has been modified to facilitate the input and evaluation of data. Additional efforts are ongoing toward incorporating a more efficient matrix solver into TOUGH. The ITPACK solver, developed at the University of Texas-Austin, will replace the current MA solver in the code. The new solver will be evaluated to assess the level of added efficiency, if any, afforded by the new solver.

4. SEISMIC ROCK MECHANICS

by *Simon M. Hsiung and Asadul H. Chowdhury*

Investigators: Asadul H. Chowdhury (CNWRA), Jaak Daeman (Univ. of Arizona), Roger Hart (ITASCA), and Simon Hsiung (CNWRA)

4.1 TECHNICAL OBJECTIVES

During this quarter, work was performed on three of the overall objectives of the Seismic Rock Mechanics Research Project. These objectives are: to assess, by conceptual models and experimental studies, the capabilities and limitations of rock-joint models/computer codes currently in use; to demonstrate by laboratory model studies and instrumented field studies the degree of accuracy (validation) for the rock-joint models/computer codes used for seismic analysis in a tuff medium; and to assess by instrumented field studies the significance of seismic pumping and to demonstrate the degree of validation for the rock-joint models/computer codes for simulation of seismic effects on groundwater hydrology. Progress made and the results obtained during the months of April, May, and June 1990 are reported in this quarterly report.

4.2 EVALUATION OF ROCK-JOINT MODELS AND COMPUTER CODES

The scope of the evaluation of rock-joint models and computer codes was discussed in the first CNWRA research program quarterly report (CNWRA, 1990). Currently, qualification studies on the 3DEC code against three of the four benchmark analytical problems have been completed. A discussion on the study results is presented in this quarterly report.

Figure 4-1 shows the three benchmark problems completed. The first problem is static, and the other two are dynamic. The Mohr-Coulomb joint model was used in the analysis of all three benchmark problems.

4.2.1 Cyclic Loading of a Specimen with a Slipping Crack

An elastic block with an inclined, internal, closed crack is shown in Figure 4-1a(i). When a constant axial displacement U_a is applied to one end of the block, and the other end is fixed, the resulting load causes inelastic slip on the joint. If the sense of displacement on the end of the block is reversed, the original unloaded condition may be reestablished; however, the load-displacement paths for loading and unloading are quite different. As shown by Olsson (1982), the stress-displacement relation for the loaded specimen illustrated in Figure 1a(ii) consists of three components. The subtle hysteresis response in a load-unload cycle is a result of joint slip and frictional locking at various stages of block deformation. A closed-form solution for the determination of the three slopes in Figure 4-1a(ii) was provided by Brady et al. (1985).

Figure 4-2 shows the 3DEC block model of the three-dimensional specimen with a planar crack. A complete load cycle in uniaxial compression was applied on the top surface of the model. The global stiffnesses were calculated directly from 3DEC results

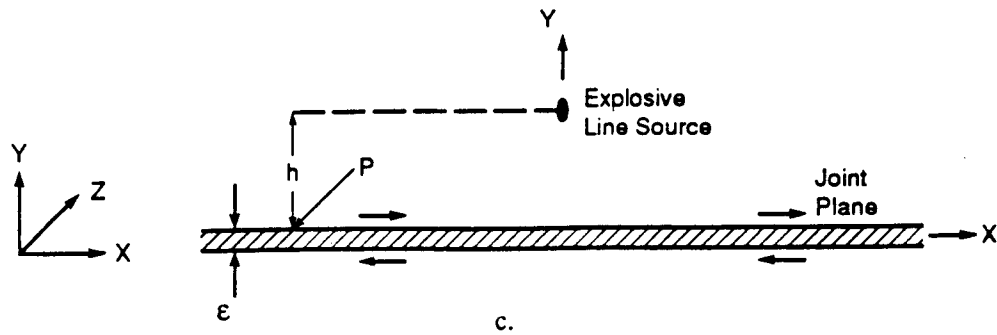
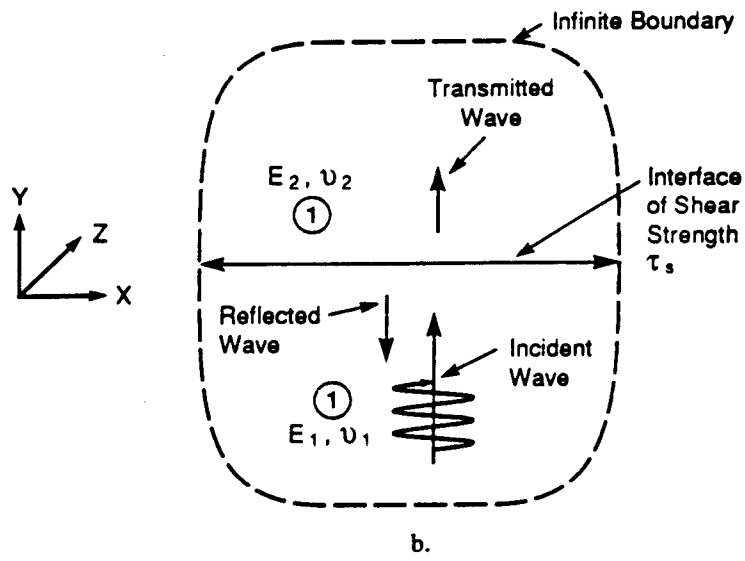
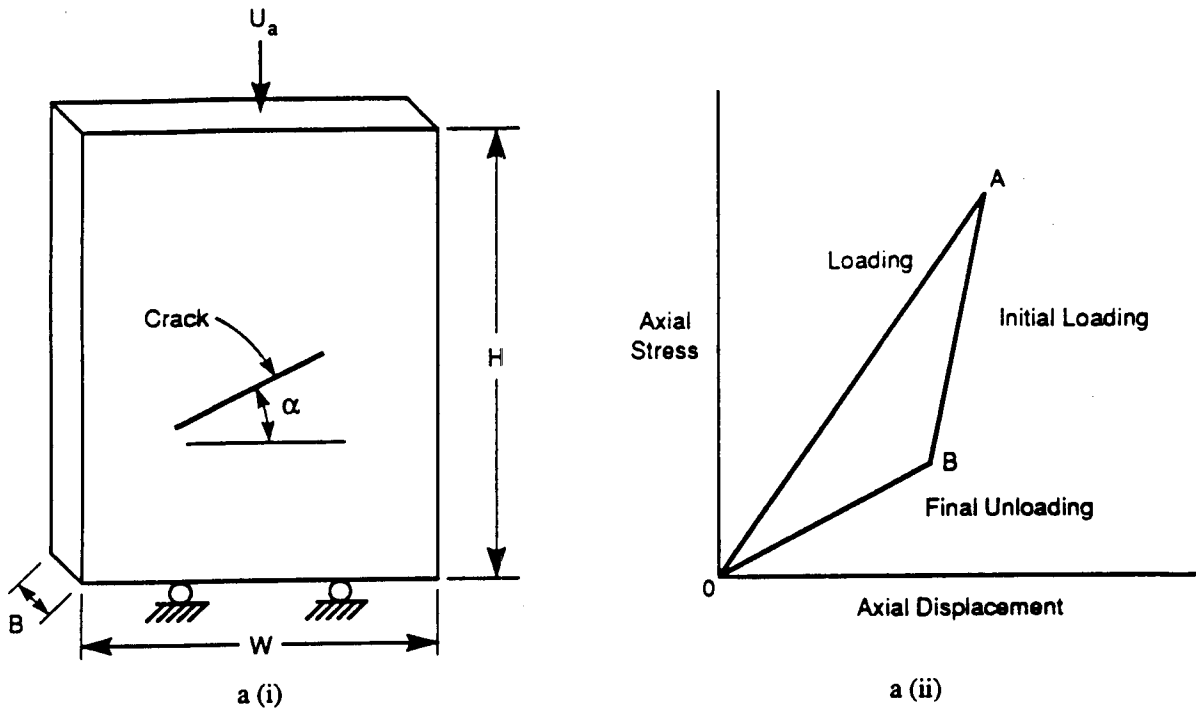


Figure 4-1. Three benchmark analytical problems: (a) cyclic loading of a specimen with a slipping crack, (b) slip in a jointed body induced by a harmonic shear wave, and (c) line source in an elastic medium with a slip-prone joint

using average vertical stresses and maximum vertical displacements for each load step. Table 4-1 shows the results from the conceptual model, UDEC, 3DEC in plane strain, and 3DEC in plane stress.

Modeling both plane stress and plane strain conditions, the results from the 3DEC analysis with the Mohr-Coulomb joint model agree well with the conceptual model and the UDEC analysis. It was observed that, similar to the UDEC analysis, the results from 3DEC analysis agree less closely as the length of the slipping crack increases with respect to the width of the specimen. This observation is expected, as the conceptual model assumes uniform distribution of normal stress on the crack and the elastic extensions, while, in practice, stress concentrations become more significant as the length of the slipping crack increases.

4.2.2 Slip in a Jointed Body Induced by a Harmonic Shear Wave

The dynamic behavior of a plane discontinuity loaded by a normally incident, plane harmonic shear wave presents a simple test of the dynamic performance of 3DEC. The problem shown in Figure 4-1b consists of a plane discontinuity, of limited shear strength, separating two homogeneous, isotropic, semi-infinite elastic bodies, and a normally incident, plane harmonic shear wave. If the transient shear stress exceeds the shear strength of the joint, slip will occur at the interface. As a result, energy is partitioned between reflected and transmitted waves and absorption at the interface. In an analysis of this problem by Miller (1978), closed-form solutions were derived for the transmission, reflection, and absorption coefficients.

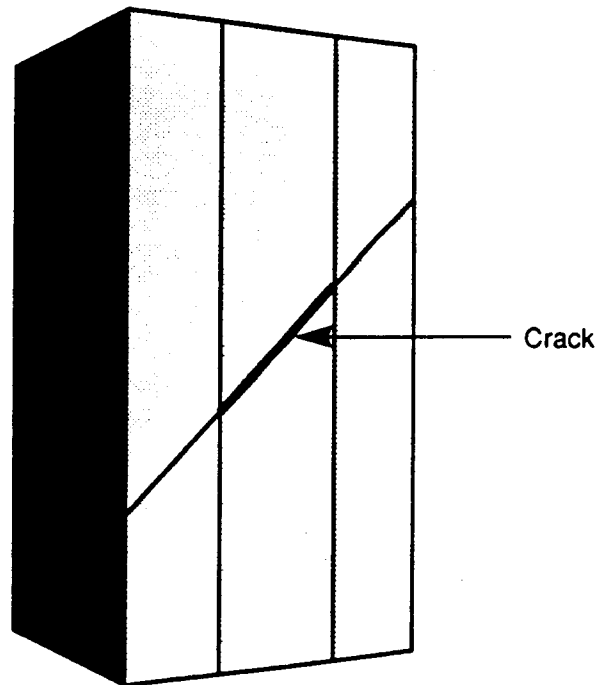


Figure 4-2. 3DEC block model of the three-dimensional specimen with a planar crack for benchmark problem (a) in Figure 4-1

Table 4-1

**COMPARISON OF 3DEC RESULTS WITH CONCEPTUAL MODEL
AND UDEC FOR A BLOCK WITH A SLIPPING CRACK
UNDER CYCLIC LOADING**

Loading Segment	Conceptual Model	UDEC		3DEC Plane Strain		3DEC Plane Stress	
	Stiffness (GPa/m)	Stiffness (GPa/m)	Error (%)	Stiffness (GPa/m)	Error (%)	Stiffness (GPa/m)	Error (%)
load (QA)	36.34	36.04	0.82	36.5	-0.44	36.8	-1.26
Unload (AB)	38.89	38.91	-0.05	38.83	0.15	38.33	1.43
Unload (BO)	34.52	34.14	1.10	35.27	-2.17	35.2	-1.96

Figure 4-3 shows the 3DEC block model showing internal discretization. A special version of 3DEC (3DECSP) was used for analysis. This version has the capability to simulate nonzero cohesion and tension when discontinuity shear and/or tensile strength is exceeded. Comparison of the acoustic coefficients for the wave propagation is conducted in terms of the dimensionless stress, τ_d , of the incident wave, defined by:

$$\tau_d = (\rho G)^{\frac{1}{2}} (\omega U) / \tau_s \quad (13)$$

where ρ is mass density, G is shear modulus, U is displacement amplitude of incident wave, τ_s is joint cohesion, ω is frequency of incident wave, and $(\rho G)^{\frac{1}{2}} = \gamma$.

Good correspondence is observed between the 3DEC results and closed-form solutions over a wide range of dimensionless stresses (Figure 4-4). The 3DEC analysis also confirmed that when the joint has a limited shear strength or cohesion, the shear wave transmitted across the interface has the peak amplitude of shear stress (Figure 4-5).

4.2.3 Line Source in an Elastic Medium with a Slip-Prone Joint

The problem shown in Figure 4-1c consists of a plane joint of infinite lateral extent in an elastic medium and a dynamic load at some distance from the discontinuity. The closed-form solution to this problem was derived by Day (1985) as a special symmetric condition for the general problem of slip of an interface due to a dynamic point source (Salvado and Minster, 1980). The problem was solved in terms of the magnitude of slip induced on the joint by the explosive-induced local load.

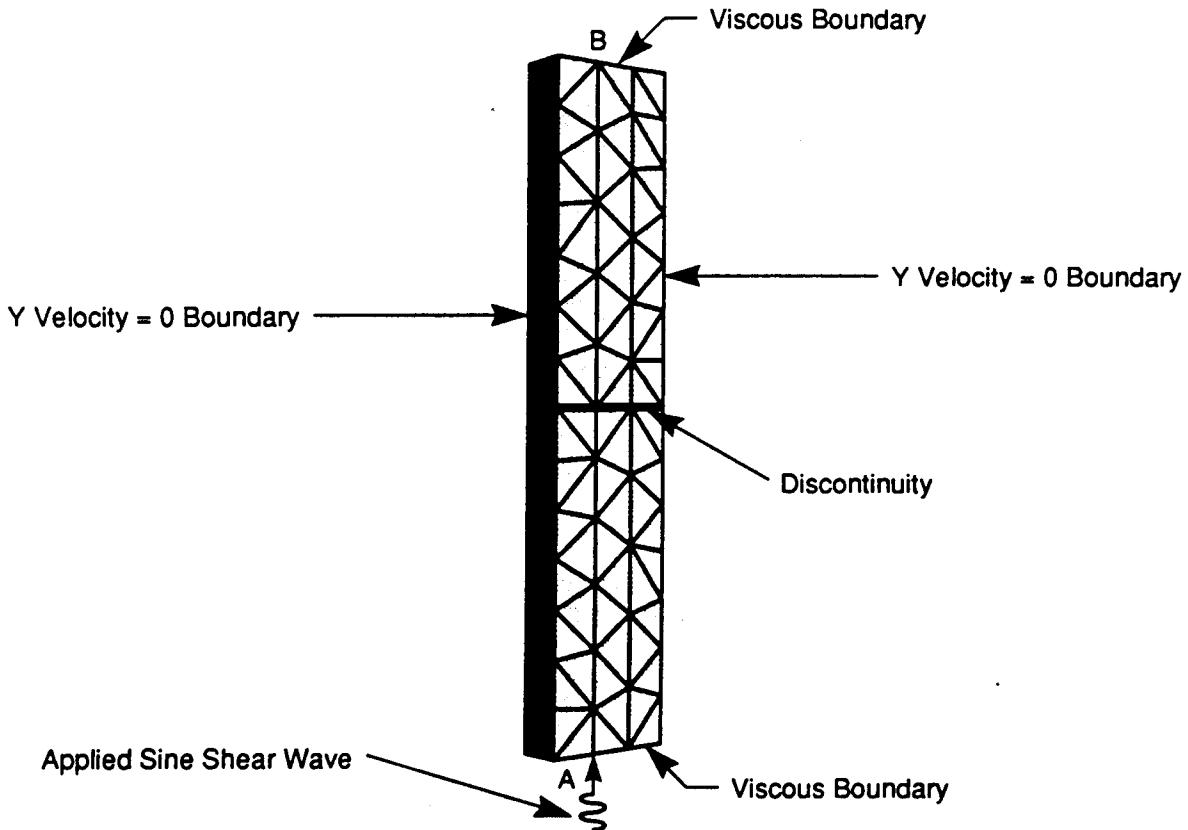


Figure 4-3. 3DEC block model showing internal discretization for benchmark problem (b) in Figure 4-1

Figures 4-6 and 4-7 show the problem geometry and boundary conditions for numerical model, and the 3DEC model showing semicircular source and "joined" blocks used to provide appropriate discretization, respectively. The dimensionless slip at point P calculated using 3DEC is plotted against the dimensionless time and is shown in Figure 4-8.

The dimensionless slip is compared with the analytical solution given by Day (1985) and the results from 3DEC analysis. The result of the 3DEC analysis provided satisfactory correspondence with the closed-form solution until the dimensionless time of 1.49. After that, a considerable deviation was shown, which can be attributed to boundary iterations (reflection). The effects of boundary reflection on slip response may be reduced by adjusting the model size.

4.3 SPECIMEN PREPARATION ACTIVITIES

Direct shear test specimens are being prepared for dynamic shear testing. In addition, cylindrical specimens for mechanical characterization tests associated with the shear specimens, including uniaxial and triaxial compression and Brazilian disk tension tests, are being prepared. These mechanical characterization tests will be performed on cylindrical specimens collected from the same tuff rock cores from which the shear specimens are being prepared.

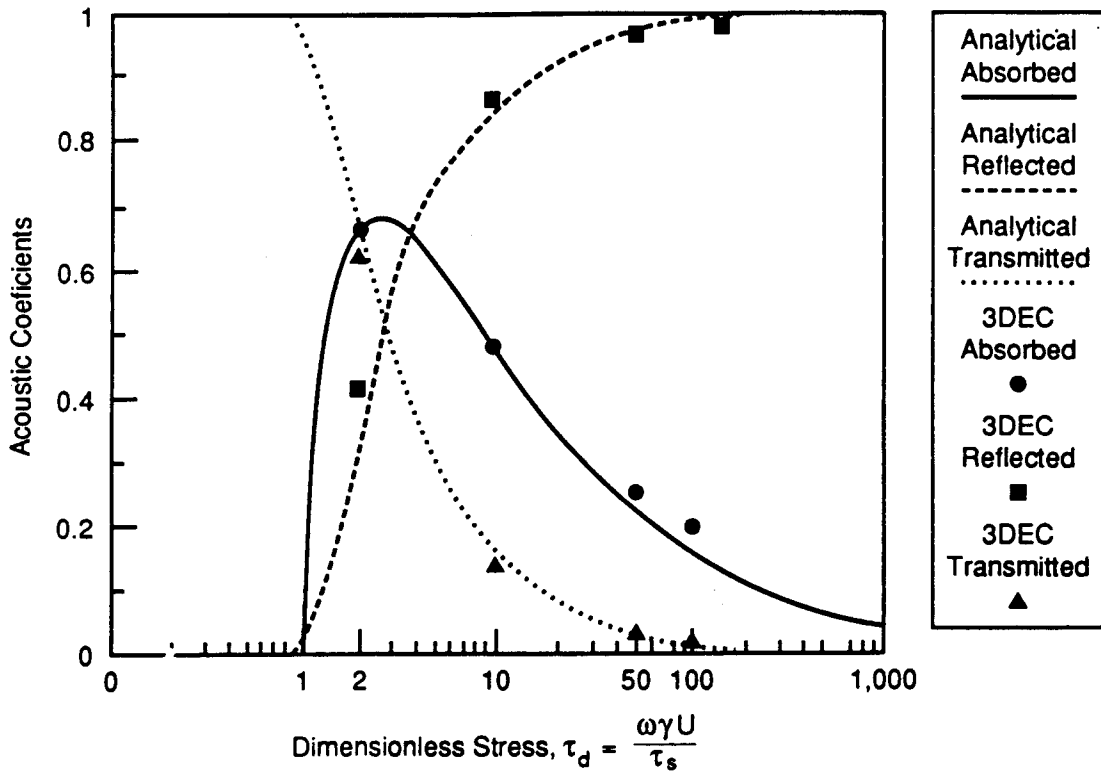


Figure 4-4. Comparison of transmission, reflection, and absorption coefficients

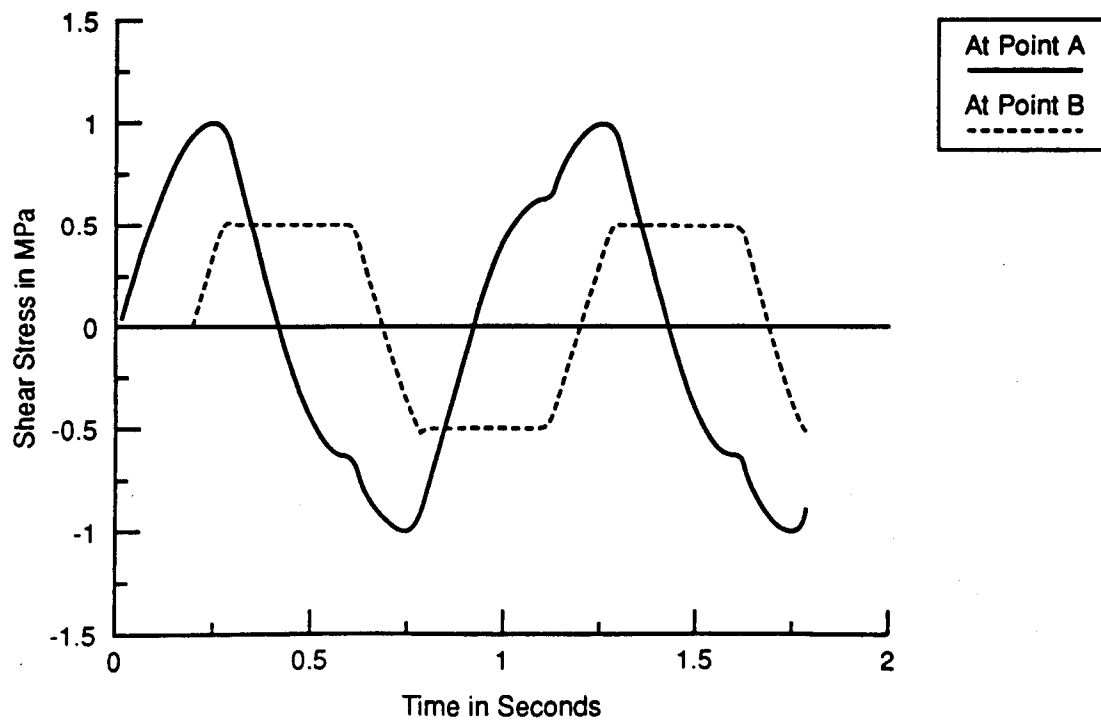


Figure 4-5. Shear stress versus time at points A and B for slipping discontinuity (cohesion = 0.5 MPa)

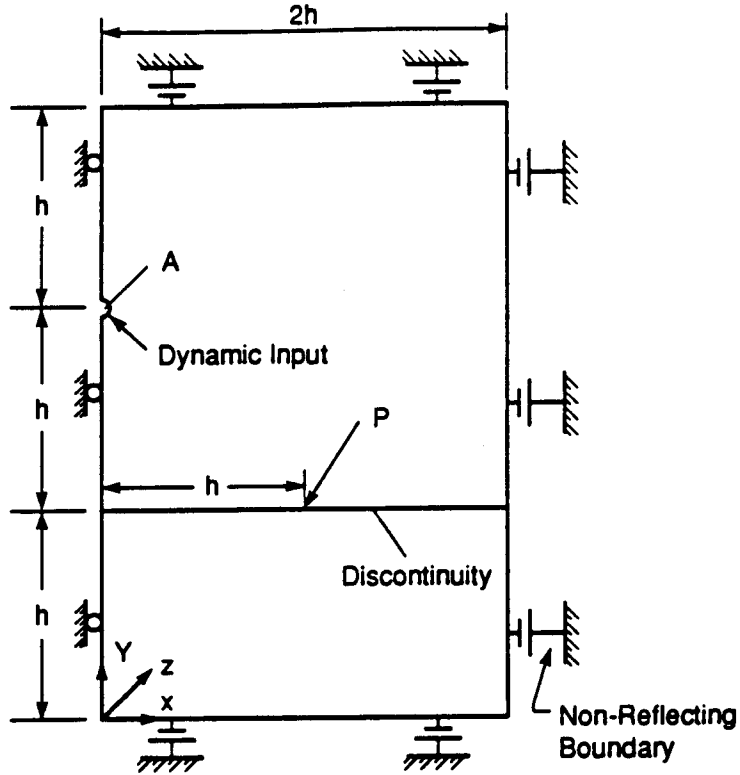


Figure 4-6. Problem geometry and boundary conditions for numerical model for benchmark problem (c) in Figure 4-1

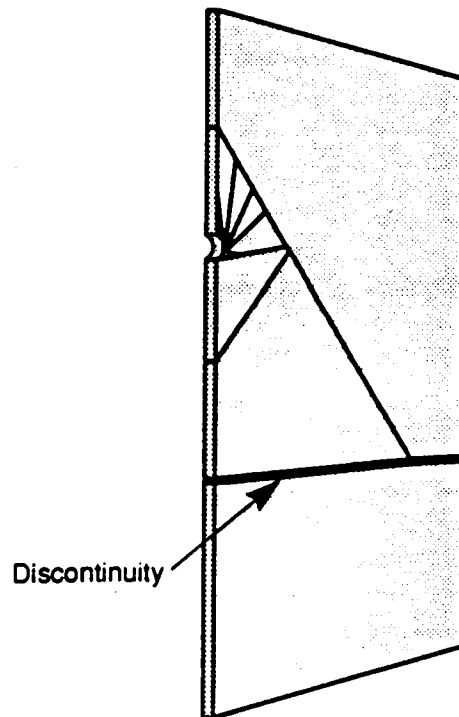


Figure 4-7. 3DEC model showing semicircular source and "joined" blocks used to provide appropriate zoned discretization for benchmark problem (c) in Figure 4-1

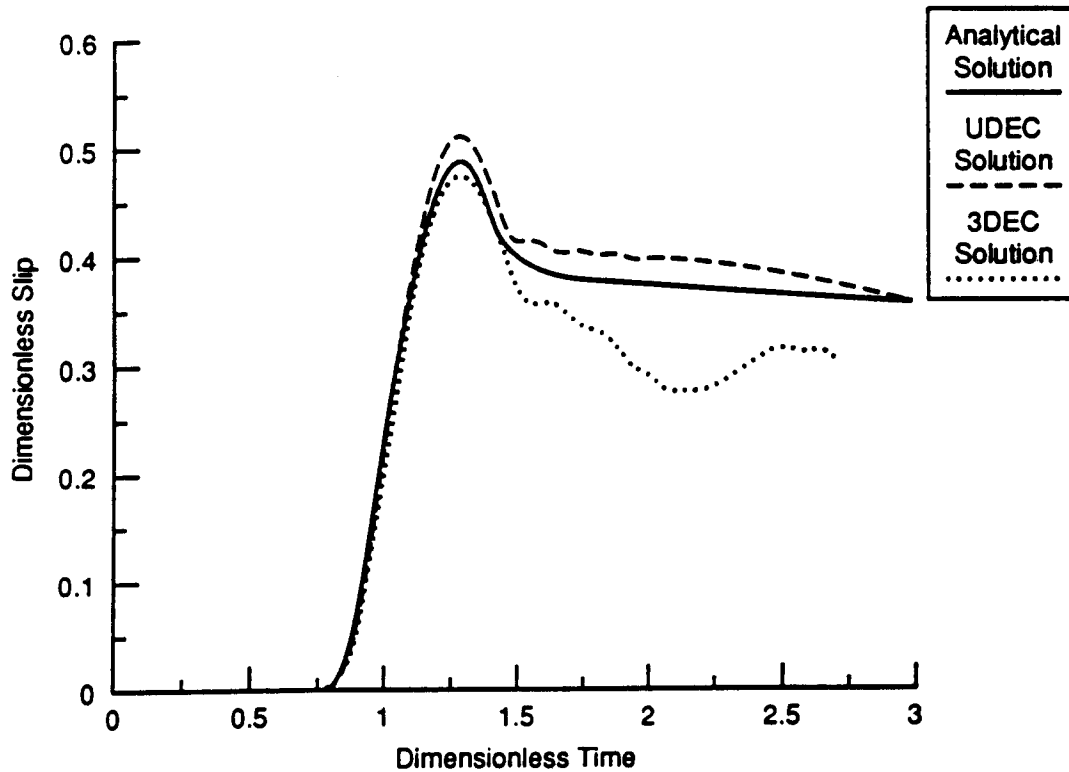


Figure 4-8. Comparison of dimensionless slip at point P with Coulomb joint-model dimensionless slip = $(4hp\beta^2/m_p)\delta u$, dimensionless time = $t\theta/h$

The shear specimens are prepared from 18-in. (457-mm) diameter core, which was drilled from the Superior, Arizona, site. Figure 4-9 shows a typical 18-in. (457-mm) diameter core collected from the field. The rock is a welded tuff of the Apache Leap formation. The top half of the shear specimen measures 8 x 8 x 4 in. (203 x 203 x 102 mm). The bottom half of the shear specimen measures 12 x 8 x 4 in. (305 x 203 x 102 mm). The cores received from the field are cored in the laboratory to produce 2-in. (50-mm) diameter cores. For uniaxial and triaxial compression testing, these are cut to a length of 5 in. (127 mm), and surface ground. For Brazilian disk tension testing, 2-in. (50-mm) diameter core is cut to a thickness of 0.5 in. (12 mm). Procedures for specimen preparation (both shear and mechanical characterization test specimens) were documented in the *Quality Assurance Program for Mechanical Characterization of Tuff, the CNWRA*, by Daemen (1990).

4.3.1 Direct Shear Specimen Preparation

During this reporting quarter, three direct shear test specimens (SRM15.1.1/15.2.2, SRM28.1.2-1A/28.2.3-B, and SRM15.3.4/15.3.5) were prepared. Figure 4-10 shows a picture of a direct shear specimen in the cutting process using a slab saw. Figure 4-11 shows the three prepared direct shear specimens. Progress in specimen preparation was slowed due to problems encountered in the cutting process. These problems are discussed briefly in Section 4.3.4. Approximately 11 other specimens are being prepared; for example, the section of core 5 to 6 in. (100 to 150 mm) thick containing the fracture surface has

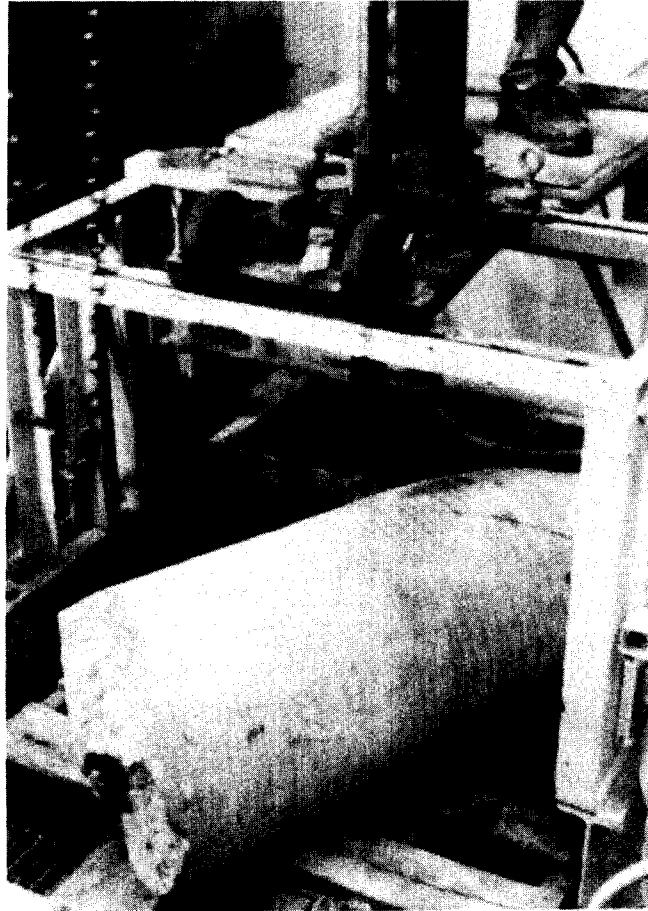


Figure 4-9. Core drilled at the field site shown set up for laboratory coring

been separated from the rest of the core by drilling 2-in. (50-mm) core specimens (used for characterization testing). These characterization specimens are ready to be cut.

4.3.2 Uniaxial and Triaxial Compression Specimens

Twenty-two core specimens have been prepared up to the point of dimension checking. This includes coring the specimen from the field core, cutting it to length, grinding the end surfaces, checking the smoothness and perpendicularity of the specimen, and measuring the length and diameter. Figure 4-12 shows the rock-specimen grinding machine used for the project. Approximately 30 other cylindrical specimens are in the preparation process.

4.3.3 Brazilian Disk Tension Specimens

One to three disk specimens for each group of uniaxial and triaxial compression test specimens were cut to length from the 2-in. (50-mm) diameter cores. Approximately 25 disk specimens were prepared. Figure 4-13 shows the core specimens after preparation for compression and Brazilian disk tension tests.

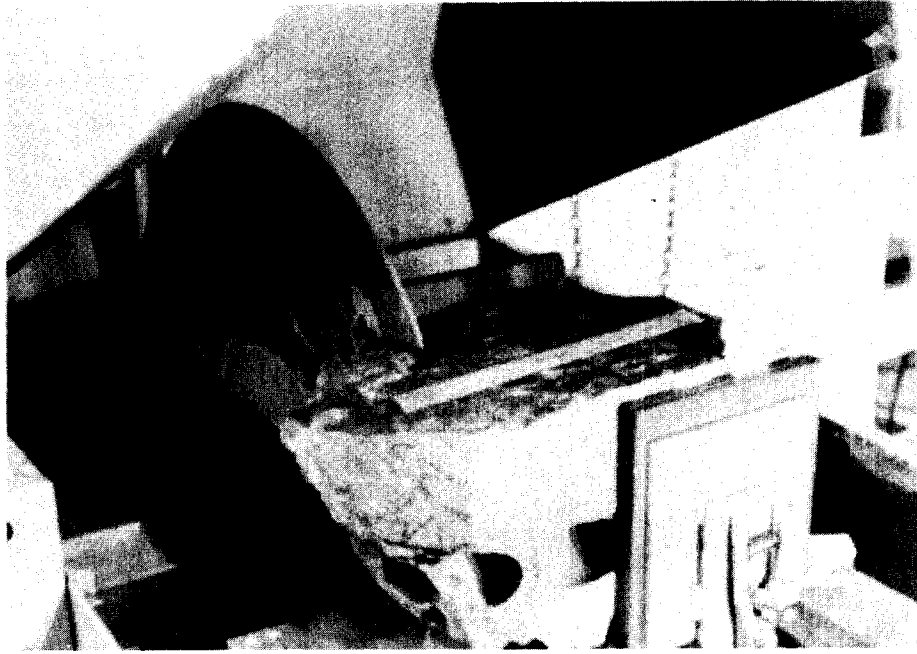


Figure 4-10. Direct shear specimen shown in the cutting process using a slab saw

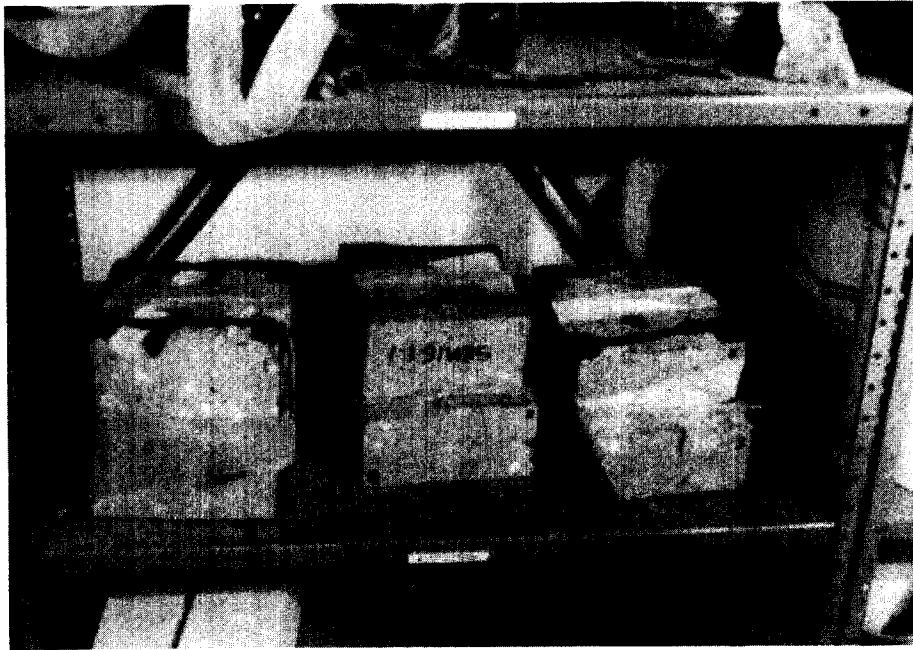


Figure 4-11. Three prepared direct shear specimens

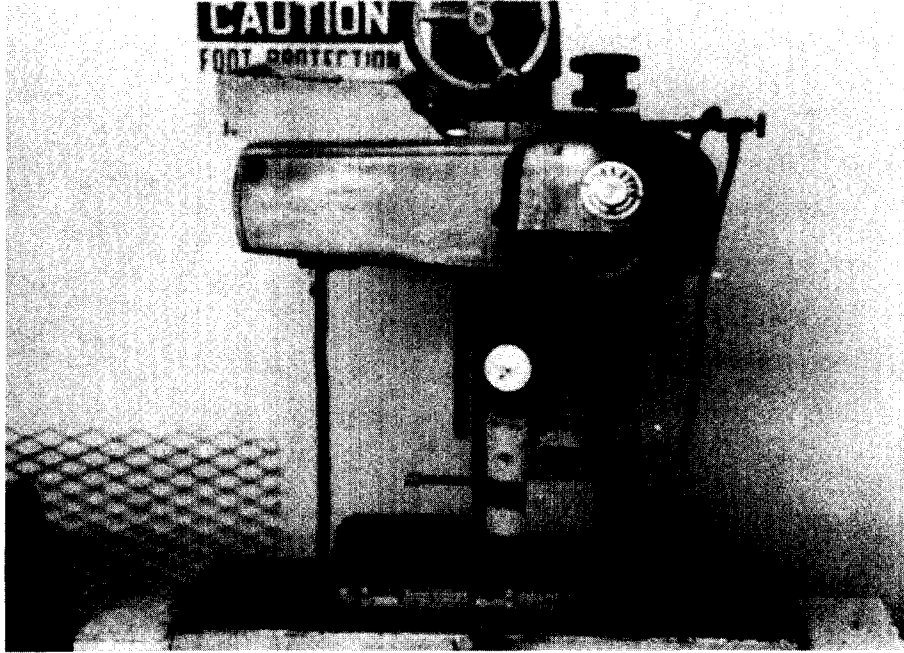


Figure 4-12. Grinding machine



Figure 4-13. Two Brazilian disk tension specimens and one compression specimen in the preparation process

4.3.4 Problems for Direct Shear Specimen Preparation

Several problems occurred in the preparation of direct shear specimens. One arose from using water as a cutting fluid to avoid the potential for altering fracture surface mechanical characteristics. This subjected unpainted metal parts of the saw mechanism to rapid rusting. The problem was partly solved by replacing threaded rod pieces with stainless steel. Also, the main carriage slide and another metal slide were cleaned frequently and given a protective coat of thick grease. This grease did not come in contact with the direct shear specimen. The use of water only, applied against the recommendations of the saw manufacturer, reduces cooling and cutting effectiveness and contributes to blade wear.

Some difficulty was encountered in clamping the large core pieces in the saw when the clamped rock surfaces were not flat. This resulted in the saw blade jamming in the sawcut. It was often necessary to back the blade off and reset the specimen. This resulted in rougher or more uneven cuts, which may be smoothed out by surface grinding.

4.4 NEVADA TEST SITE (NTS) DATA COLLECTION ON GROUND-SHOCK EXCITATION

Chapter 6 of the *Site Characterization Plan, Consultation Draft* (1988), contains a conceptual description of the Yucca mountain repository system. Several components of this system will be subjected to seismic-design considerations. It is well accepted that the design of surface buildings can be developed according to various well-known structural seismic standards and codes. However, the seismic behavior of underground structures is not well understood; and the seismic-design standards for underground facilities are not very well developed. Special efforts, therefore, must be made to understand the key parameters affecting the performance of underground structures and to ensure that analytical design models (e.g., computer codes) are capable of accurately simulating the observed seismic response of underground structures. Since ground shock due to underground explosion events is one source of seismic activities at the proposed Yucca Mountain site, data from field tests on ground-shock excitation are valuable for understanding the repository performance under ground shock and for validating the analytical design models.

The goal of this study is to assemble data sets on impulsive ground-shock field tests. These data will enable the CNWRA, and therefore the NRC, to develop methodologies to evaluate and reduce uncertainties in the analytical design models used in seismic assessment of a repository in tuff media. The objective is to quantify uncertainties in predicting the preclosure and postclosure seismic performance by understanding the capabilities and limitations of numerical modeling methods currently in use. Specifically, five or six collected data sets will be used to determine if a particular code can adequately predict ground motion in the vicinity of faults, joints, and other discontinuities in the rock mass. Databases being searched include: NTIS, COMPENDEX PLUS, GEOARCHIVE, GEOREF, NUCLEAR SCIENCE ABST., DOE ENERGY, ENERGYLINE, GEOBASE, GEOMECHANICS ABSTRACTS, AND DASLAC.

There are many types of nuclear-explosive (NE) and conventional high-explosive (HE) tests that have been performed at the Nevada Test Site and various sites for which block-motion information has been recorded. Important components of the block-motion

information are the velocity and displacement data along major discontinuities forming geologic blocks. Tests have included surface bursts, shallow buried cratering, and deep underground vertical or horizontal line-of-sight events, of which the deep-underground NE and HE tests are of interest for this study.

From these tests, at least two types of motion data, driven and triggered, can be collected. Driven motion, of interest for this study, is dominated by the explosion-induced stress transients, whereas triggered motion is dominated by the partial seismic relief of prestress conditions. Driven-motion data can be further divided into very near-field motion in the collapse region and strong ground motion. It is the strong ground-motion data that are of interest because displacements are large enough to accurately measure differential displacements across geologic features without the rock mass being significantly damaged.

Data required to perform a complete block-motion analysis include the following.

- (1) Site geology and geometry of underground facilities. These include a description of rock type and of fault and bedding-plane characteristics involved in the field test.
- (2) Block-motion observations of velocity and displacement-time history records and final geologic block displacements after passage of the ground wave on opposing sides of a major structural feature.
- (3) Ground motion, which includes stress and particle velocity measurements. This can be accurately scaled to other locations by knowing the specified range (distance from the event) and without knowing the event yield.
- (4) Material properties for both effective rock-mass materials and discrete geologic features. These include rock-index properties (e.g., density), wave speeds, strengths, and stiffnesses.
- (5) Tectonic stress magnitude and direction measurements of preblast in situ principal stresses.

A preliminary set of five field test cases for which some of the most complete data sets have been collected were selected, and attempts are being made to secure the documents containing the data. The five cases are listed in Table 4-2.

Published references for the first two cases have been obtained, and data are currently being summarized. Four other key references have been identified for the last three cases, and efforts are underway to locate document copies.

Access to several of the documents used to date has not been easy because of their unpublished and/or classified status. Use of some documents will most likely require permission of the Defence Nuclear Agency (DNA). It may be necessary to review classified documents at a secured location, extract the data set sought by the project that does not allow estimation of event yield, and have DNA screen the study report for security classification. It is intended that the study report be unclassified and unrestricted in distribution.

Table 4-2

CANDIDATE FIELD TESTS OF BLOCK MOTION

Event	Test Date	Rock Type	Number Observ.	Event Yield	Saturation	Test Type
ROCKTEST II	3/70	Granite	3	small	unsat.	DIHEST*
STARMET	11/70	Granite	4	Very small	unsat.	DIHEST
MIGHTY EPIC	5/76	Tuff	18	moderate	part.sat.	UGT**
DIABLO HAWK	9/78	Tuff	30	moderate	part.sat.	UGT
HURON LANDING	9/82	Tuff	10	moderate	unsat.	UGT

*Direct Induced High Explosive Simulation Technique

**Underground Test

4.5 FIELD INVESTIGATION

The field-site evaluation and selection of the Lucky Friday Mine, Mullan, Idaho, for instrumented field studies for (1) seismic effects on underground openings and (2) seismic effects on hydrologic regime have been discussed in the first CNWRA research program quarterly report (CNWRA, 1990). The instruments are to be installed at the Lucky Friday Mine to monitor (1) the short- and long-term responses of excavations and their supports to repeated seismic events and (2) the change in water pressure in faults or other structural features in the rock mass as a result of seismic loading.

4.5.1 Excavation Response

The transient and long-term displacement response of excavations will be monitored in close proximity to seismic events greater than 1 Richter magnitude. The objective in this study is to monitor the effects of dynamically induced stress (and failure) states. This will be accomplished at the Lucky Friday Mine by instrumenting tunnels in the ramp system below the present mining. The two sites, Nos. 95 and 101, are both at 5210 level and are near the bottom of the present ramp development; thus, they are new excavations which have not deteriorated. The instruments will be installed at this location. The excavations have a 10-foot (3-m) square cross section and are supported by 6-foot (1.8-m), resin-grouted, 1-inch (2.5-cm) diameter rebar, 2 x 2-inch (5- x 5-cm) chain-link mesh, and 1-1/2 to 2-inch fiber-reinforced shotcrete.

Three basic types of instruments are necessary:

- (1) Extensometers to monitor long-term displacement changes,
- (2) Triaxial velocity gauges to determine the transient response of the rock at excavation surfaces, and
- (3) Closure points to monitor opening closure.

Figure 4-14 shows a cross section of the tunnel and location of the instruments. Both instrument sites have the same geometry. Five 5-anchor rod extensometers are proposed per section. The deep anchor will be at approximately 25 feet (7.6 m) down the hole, with anchors at roughly 5-foot (1.5-m) intervals. Hydraulically inflated anchors will be used to ensure a nonslipping grip. The rod displacement will be sensed by linear potentiometers in the instrument head, which has a range of 2 inches (5 cm) and a resolution governed by the resolution of the data acquisition system. The linear potentiometers will be read by a remote data acquisition system described in Section 4.5.3.

Closures will be measured across at least two cross sections to determine the long-term cross-sectional dimension change in the opening. The closure will be determined manually using a tape extensometer (Figure 4-14).

The magnitude of the ground shock must be measured at the instrumentation site. A triaxial velocity gauge will be used at each section for the monitoring function. The gauges will be amplified at the gauge location, and analog signals sent to the U.S. Bureau of Mines computer at the ground surface via a twisted pair up the Silver Shaft.

4.5.2 Piezometers - Pore Water-Pressure Measurement

The transient pore water-pressure change along several fault structures that are in close proximity to the seismicity will be measured. Because the fault structures must be fully saturated with water, the zones in which the fracture are to be sampled must be below the present workings, which provide a draw-down to the surrounding groundwater. The faults must be pierced and packed off, with pressure measurements taken in the packed-off regions.

An NQ-sized hole [2.98-in. (7.57-cm) diameter] is to be drilled at approximately 20 degrees downward in a southerly direction from the 5700-level station (Figure 4-15). The hole will be directed toward an intersection with the main and footwall split fault structures as well as with the South Control fault. These structures should be intersected within about 1200 feet (366 m) of the collar, some 400 feet (122 m) below the 5700 level.

These intervals will be packed off down-hole using inflatable straddle packers. The straddle-packer sections will be separated by pipe, and stiff pipe sections will be used to push the packers into position using the feed of the diamond drill. A vibrating-wire pressure transducer will be installed in the interval between each straddle packer, and in at least one nonfault zone between the packed regions. A secondary or backup pressure-measurement capability will be obtained using a set of secondary access tubes to the packed

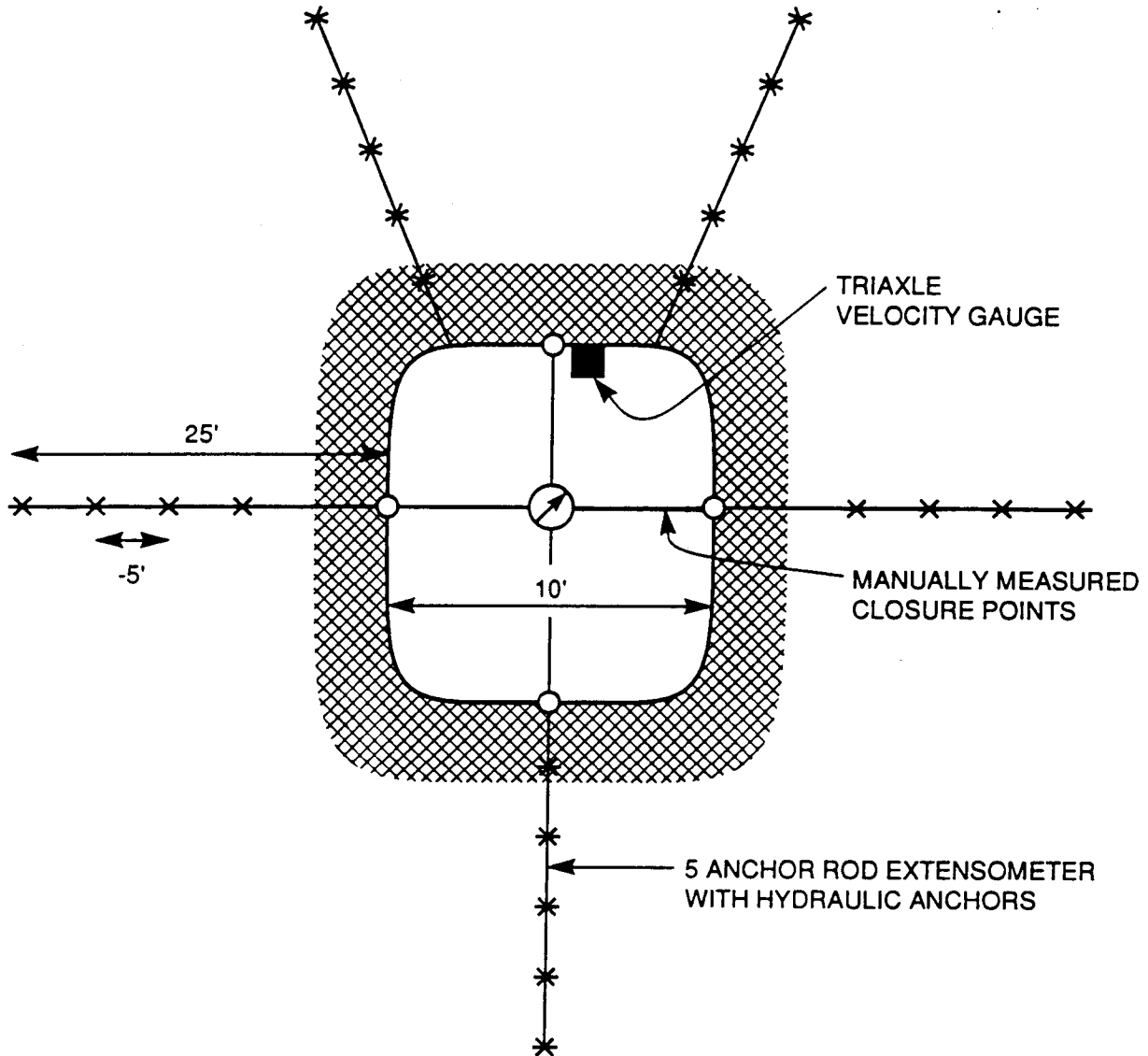


Figure 4-14. Proposed typical instrumentation array for cross sections of the 5210 sublevel at 95 and 101 stopes

intervals. The packers will be inflated with water via inflation lines, which will be connected to a hydraulic manifold at the borehole collar. Any pressure leak-off from the packers can be monitored, and packers repressurized. The magnitude of the ground shock will be measured at the straddle-packer sites by a hydrophone.

4.5.3 Data Acquisition

The extensometer and piezometer data acquisition system consists of two primary components: an underground data logger and a surface personal computer. A 32-channel data logger with power supply will be located near one of the extensometer installations within the 5210 ramp and at the 5700-level station. A multiplexer board will be located at the other extensometer installation to sample the extensometers and send it

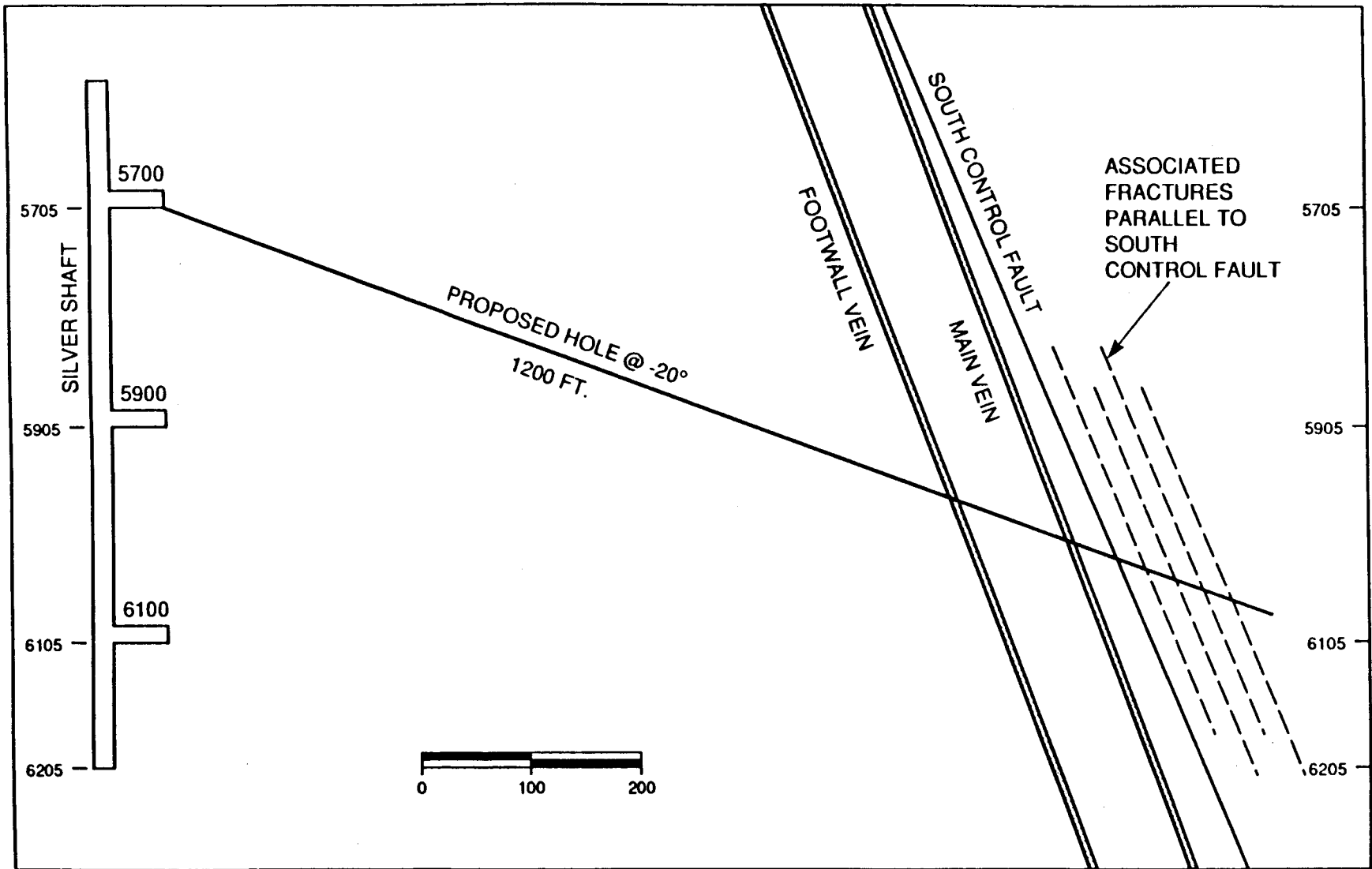


Figure 4-15. Lucky Friday silver shaft cross section of the proposed drill hole for piezometer installation (view looking N74°E)

to the data logger at the 5210 ramp. Four piezometers will be connected to the second data logger at the 5700-level station. The two data loggers will be networked via a coaxial cable. The triaxial gauges and hydrophone will be connected to the mine-wide macro-seismic network of the U.S. Bureau of Mines. The ground-shock data and extensometer and piezometer response data will be communicated to the computers at the surface through the Lucky Friday mine cable system.

The primary difficulty in data acquisition is the sampling frequency of the piezometers. A typical rockburst event has a duration of less than 10 seconds. Because the timing of these events is unknown, a sampling frequency must be set such that several data points are obtained during a seismic event. If a sampling frequency of, for example, 1/2 second were used, the data-storage requirements would be extremely large. To solve this problem, the data logger can be used to check the change in successive data points for each transducer. If no change occurs within successive time intervals, then the data are only saved at a given rate (e.g., every hour). If, however, a change over the given target level is detected, data are sampled at the programmed interval (i.e., 1/2 second). In this manner, both the transients and long-term pressure changes will be monitored.

4.6 REFERENCES

- Brady, B. H. G., L. M. Cramer, and R. D. Hart. 1985. Preliminary analysis of a loading test on a large basalt block. Technical Note. *Int. J. Rock Mech. Min. Sci. & Geomech. Abstr.* 22:345-348.
- CNWRA. 1990. *Report on Research Activities for the Quarter January 1 Through March 30, 1990*. CNWRA 90-01Q. San Antonio, Texas: CNWRA.
- Daemen J. J. K. 1990. *Quality Assurance Program for Mechanical Characterization of Tuff, the CNWRA*. Tucson, Arizona: Department of Mining and Geological Engineering, University of Arizona.
- Day S. M. 1985. Test problem for plane strain block motion code. S-Cubed Inc., Memorandum to Itasca, Inc. Minneapolis, Minnesota: Itasca, Inc.
- DOE. 1988. *Site Characterization Plan, Consultation Draft*. DOE/RW-0160, Vol III. Washington, D.C.: DOE.
- McGarr A. 1984. Scaling of ground motion parameters, state of stress, and total depth. *J. Geophys. Res.* 89(B8):6969-6979.
- Miller P. K. 1978. The effects of boundary friction on the propagation of elastic waves. *Bull. Seis. Soc. America* 68:987-998.
- Olsson W. A. 1982. Experiments on a slipping crack. *Geophys. Res. Letters* 9(8): 797-800.
- Salvado C., and J. B. Minster. 1980. Slipping interfaces: A possible source of radiation from explosive sources. *Bull. Seis. Soc. America* 70:659-670.

5. INTEGRATED WASTE PACKAGE EXPERIMENTS

by Gustavo Cragnolino and Narasi Sridhar

Investigators: Gustavo Cragnolino (CNWRA) and Narasi Sridhar (CNWRA)

5.1 TECHNICAL OBJECTIVES

The objectives of the Integrated Waste Package Experiments (IWPE) are planned to be accomplished by the following tasks listed in accordance with Revision 1 of the program plan: (1) collection and review of information for assessment of the current status of the Yucca Mountain Project (YMP) corrosion and materials program for waste-package containers, (2) waste-package experimental programs, and (3) general support and reporting.

The current quarterly report follows the above task classification. A second revision of the IWPE program plan was submitted to the NRC on May 23, 1990. Following the approval of the second revision, future quarterly reports will reflect the Revision 2 task classification.

5.2 COLLECTION AND REVIEW OF INFORMATION ON CORROSION FOR WASTE-PACKAGE CONTAINERS

As part of the activities in Task 1, the critical review of the experimental results reported by Lawrence Livermore National Laboratory (LLNL) and by Cortest Columbus was continued. In this reporting period, their work on crevice corrosion of candidate container materials was analyzed; and the more relevant aspects of both studies are presented below.

Crevice corrosion is a form of localized attack that occurs within crevices and other shielded areas where a stagnant solution is present. The occurrence of crevice corrosion, as a plausible degradation mode for the current design of containers and their emplacement in the boreholes of the proposed Yucca Mountain repository, needs particular consideration. Contact of the container outer surface with rocks, dirt, packing fillers, or other materials inadvertently placed in the borehole gap may lead to the formation of creviced or shielded areas where the initiation of crevice corrosion is possible in the presence of an appropriate aqueous environment. In addition, weldment voids and flaws or deep surface scratches and marks may act as microcrevice sites. It should be noted, however, that independently of any particular design, all engineered structures and components are more prone to be affected by crevice corrosion than by pitting corrosion. Obviously, an adequate design can reduce the risk of crevice corrosion; but in many industrial applications, fabrication defects or the deposition of particulate matter, sometimes under abnormal operating conditions, lead to the premature initiation of this form of localized attack.

Despite the above noted reasons, crevice corrosion of the candidate materials for high-level nuclear waste containers has not been studied systematically in the experimental program conducted at LLNL as a part of the YMP Waste Package Plan. The results reported until now are reviewed in the next section together with results of the work conducted at Cortest Columbus under NRC sponsorship.

5.2.1 LLNL Investigations

Initial tests were carried out using rectangular coupons, fitted with PTFE washers containing 12 separate slots to promote crevice-corrosion conditions (McCright, 1984). Specimens of AISI 304L, 316L, and 317L stainless steels were tested, among other steels, in J-13 well water conditioned with crushed tuff rock at 100°C and in the gaseous phase in equilibrium with that solution (i.e., air saturated with water vapor). Triplicate specimens of each alloy were used in the tests. After 1000 hours of exposure to both environments, specimens were weighed, weight losses were determined, and the surfaces were examined to detect the occurrence of localized corrosion in the freely exposed and the creviced surfaces. No signs of localized corrosion were detected in any of the specimens tested. Weight loss data are given in Table 5-1.

Table 5-1
CORROSION TEST RESULTS FOR STAINLESS STEELS SPECIMENS
(McCRIGHT, 1984)

ALLOY	CORROSION RATE ($\mu\text{m}/\text{y}$)					
	J-13 well water (100°C)			Air saturated with water vapor (100°C)		
	#1	#2	#3	#1	#2	#3
314L SS	nil	0.25	nil	nil	0.25	nil
316L SS	nil	nil	nil	0.51	0.51	0.51
317L SS	0.25	nil	0.13	0.25	0.51	0.76

Nil is less than 0.13 $\mu\text{m}/\text{year}$, which is the weight-loss detection limit.

The results of more extended crevice-corrosion testing were also reported (Glass, 1984). After approximately one year exposure to J-13 well water at temperatures ranging from 50 to 100°C, it was found that all the alloys tested, including AISI 304L, 316L, 321, and 347 stainless steels as well as Incoloy alloy 825, exhibited preferential attack in the creviced area. Although the attack was considered to be minor and was described as *staining*, it is possible that breakdown of the passive film occurred within the crevice, even in a relatively mild environment such as J-13 well water. Prolonged exposure time and more aggressive environmental conditions may have led to a more severe attack. It was concluded from weight-loss measurements that all stainless steels tested exhibited very low corrosion rates, as shown in Table 5-2. The corrosion rates were found to be comparable

to that of Incoloy alloy 825. On the basis of these results, the authors (Glass, 1984) suggested that any one of these candidate alloys could meet the 300- to 1000-year containment objective. However, they also indicated that the different materials may exhibit varying degrees of susceptibility to crevice corrosion even in J-13 well water. A more sensitive technique for evaluating the tendency to crevice corrosion is required.

Table 5-2

CORROSION RATE OF CANDIDATE CONTAINER MATERIALS IN J-13 WATER AS DETERMINED FROM WEIGHT-LOSS DATA (GLASS, 1984)

ALLOY	Test Duration	Corrosion Rate ($\mu\text{m}/\text{y}$)				
		Temperature ($^{\circ}\text{C}$)				
	(hrs)	50	70	80	90	100
304L	3548	0.03	0.20	0.20	0.15	0.10
	5000	0.23	0.20	0.23	0.15	0.13
316L	3548	0.23	0.25	0.28	0.15	0.18
	5000	0.10	0.23	0.25	0.25	0.20
317L	3548	0.35	0.28	0.28	0.18	0.08
	5000	0.03	0.25	0.20	0.28	0.10
321	3548	0.18	0.30	0.20	0.20	0.20
	5000	0.13	0.28	0.20	0.33	0.03
347	3548	0.23	0.38	0.25	0.20	0.25
	5000	0.28	0.33	0.25	0.28	1.05
I-825	3548	0.30	0.28	0.18	0.20	0.15
	5000	0.38	0.38	0.20	0.28	0.28

5.2.2 Cortest Investigations

Beavers and Durr (Beavers, 1990) recently reported the results of crevice corrosion tests. For both AISI 304L stainless steel and Incoloy alloy 825, no attack was observed after 4050 hours of exposure to aerated, simulated J-13 water at 90°C . As in the case of the tests conducted at LLNL, ribbed PTFE washers were used to define the crevice geometry; and triplicate specimens of each alloy were tested. The testing solution was allowed to evaporate in approximately 1 week by controlling the rate of air flow through the solution and the cooling-water flow rate in the condensers located in the cover of the testing flasks. Then, fresh J-13 water was replaced into the flask, and the operation was

repeated on a weekly basis for the duration of the test. The corrosion rate, determined by weight loss, was found to be lower than $0.02 \mu\text{m}/\text{y}$ for both alloys. No signs of localized corrosion were detected in these long-term boil-down tests. As a result of the evaporation process, in these tests the solutions are expected to become concentrated with time, giving rise to high concentrations of soluble salts over the long testing period. For these reasons, it is difficult to understand why crevice corrosion was not observed in AISI 304L stainless steel, which is an alloy extremely susceptible to this type of localized attack. For example, Sedriks (Sedriks, 1979) reviewed data showing that the probability of crevice-corrosion initiation for 304L after 30 days exposure to seawater ($19.4 \text{ g Cl}^-/\text{kg H}_2\text{O}$) rises from 70 to 90 percent of the specimens tested by increasing the temperature from 25 to 50°C. This is a clear indication of poor resistance to crevice corrosion in relatively concentrated chloride solutions.

Additional data on the behavior of AISI 304L stainless steel and Incoloy alloy 825 have been provided by Beavers and Durr (Beavers, 1990). After approximately a 3000-hour exposure to an aerated solution of pH 10 containing 1000 ppm Cl^- as the main aggressive species and to the vapor phase above the solution at 90°C, crevice corrosion of AISI 304L was observed in both the vapor and liquid phases. On the other hand, no evidence of localized corrosion was observed on Alloy 825.

5.2.3 Future Research Needs

It is apparent that limited experimental work has been done to assess the resistance of the austenitic alloys to crevice corrosion under simulated tuff repository conditions. In addition, the scarce data are essentially confined to behavior in a single environment (i.e., J-13 well water) without considering variations in pH, temperature, and concentration of anionic and cationic species. Also, the initiation of crevice corrosion is critically related to the geometry and dimensions of the crevice (i.e., crevice gap and depth). Another important factor is the creviced/uncreviced area ratio. The effect of these parameters has not been evaluated in the studies discussed above. Finally, an additional consideration is the nonmetallic material used to configure the crevice. PTFE is the single material used in the tests reviewed above. This material, like many polymers, will creep under mechanical loading at relatively low temperatures; and hence, crevice dimensions may be altered. No attempt has been done to test other materials. Ceramic or tuff as non-metallic components of the crevice may have a different effect that requires experimental evaluation.

From an experimental point of view, important developments in electrochemical techniques used for the study of crevice corrosion (Ijessling, 1990) have not been applied to container materials under environmental conditions that simulate more closely those expected in the repository. In addition, the existence of heat-transfer effects combined with a geometry that may contribute to a significant buildup in the concentration of aggressive species has not yet been considered.

From a practical point of view, it should be noted that crevice corrosion of austenitic stainless steels and nickel base alloys has been studied extensively, mainly in seawater environments (Sedriks, 1979 and 1982). Although few studies have examined the effect of alloying elements as single variables, since most of the comparisons have been made with commercial alloys, resistance to crevice corrosion is well known to increase with

chromium content. This is probably because chromium raises the pitting potential in the noble direction, thereby rendering film breakdown within the crevice more difficult. Nickel also seems to have a beneficial effect, but undoubtedly molybdenum provides the greatest improvement in crevice-corrosion resistance. Nitrogen in the presence of molybdenum also enhances crevice-corrosion resistance. It should be emphasized that these correlations are strictly valid for solutions containing relatively high chloride concentrations (i.e., artificial seawater). In the current experimental program, more dilute solutions containing anions such as HCO_3^- , SO_4^{2-} , NO_3^- , and F^- , in addition to chloride are of particular interest. The selection of Hastelloy alloy C-22 as another alloy within the experimental program permits study of the validity of the above noted trends at higher temperatures and in solutions not previously considered.

5.3 WASTE PACKAGE EXPERIMENTAL PROGRAMS

The objective of this task is to provide independently developed data for the NRC to use in the evaluation of information supplied by DOE regarding the degradation of waste-package container materials. The experimental program has been divided into two major tasks: (1) Corrosion of Container Materials in the Tuff Repository Environment and (2) Metallurgical Stability of Container Materials in the Tuff Repository Environment. The latter task includes studies of hydrogen absorption and embrittlement.

5.3.1 Corrosion of Container Materials in the Tuff Repository Environment

The main activities within this task have been related to the initial material and electrochemical characterization of the candidate alloys. The initial material characterization is performed to document the microstructural condition of the materials to be tested, the corrosion rate in some standard immersion tests related to intergranular corrosion, and any significant variations found on the surfaces of the materials that may affect long-range performance. In the current reporting period, the initial material characterization tests were completed. Recommendations for future investigations are given. The electrochemical characterization of the candidate container materials has been designed to elucidate the range of performance of these materials as a function of environmental variables. Localized corrosion (crevice corrosion and pitting) is considered to be one of the most critical of the corrosion processes, and hence emphasis is placed on experimental investigation of these corrosion modes. The cyclic, potentiodynamic, polarization curve has been chosen as the test technique. The initial tests used to verify the test techniques and the results of tests on two materials, Incoloy alloy 825 and AISI 304L stainless steel, are reported here.

5.3.1.1 *Microstructural Analyses of CDA-613*

The microstructures of the candidate materials were presented in the previous quarterly report (CNWRA 90-01Q). It was indicated that in the case of the Copper-Aluminum alloy (CDA-613), precipitates were observed throughout the matrix and that these precipitates were probably Cu-Fe-Al intermetallic particles. In the current reporting period, the scanning electron microscope (SEM) was used to analyze the precipitates. A sample of CDA-613 (heat No. Ampco Metal - M5459) was polished, etched, and then observed in the SEM. Energy dispersive X-ray analysis (EDX) was conducted using

the spot mode. The results are subject to some limitations: (1) the depth of analysis can be considerably larger than the thickness of the precipitates, and hence dilution from the matrix may result; and (2) selective dissolution may occur during etching, resulting in a change in composition of the precipitates. However, the analysis can be used as a qualitative indicator of the chemical distribution within the alloy.

The results are shown in Figure 5-1 in terms of weight percent of each element. The precipitate particles are shown as richer in iron and depleted in aluminum and copper, a finding consistent with literature. Brezina (Brezina, 1982) has reviewed the aluminum bronzes quite extensively. The solubility of iron in the alpha phase of the Cu-Al system is quite low and decreases with a decrease in temperature, as shown in Table 5-3.

Table 5-3

**SOLUBILITY OF IRON IN CU-AL ALPHA PHASE AS A
FUNCTION OF TEMPERATURE (BREZINA, 1982)**

Temperature (°C)	Fe (wt. %) Solubility
500	0.6
600	0.9
800	1.5
1000	2.6

It is not surprising, therefore, that CDA-613 containing about 2.5 percent Fe exhibits numerous iron-rich precipitates. West (West, 1982) refers to these particles as alpha iron, while Brezina states that the iron-rich particles in the aluminum bronzes may include alpha-iron, FeAl, and Fe₃Al intermetallics. The literature analyses of these particles range from aluminum-enriched to aluminum-depleted precipitates. The current results are qualitatively consistent with the literature results, but cannot be used to differentiate among the above three types of iron-rich particles because of possible dilution from the matrix. In any case, the potential concern with this alloy is localized corrosion at the iron-rich particles and galvanic corrosion of the particles when coupled with the copper-rich matrix.

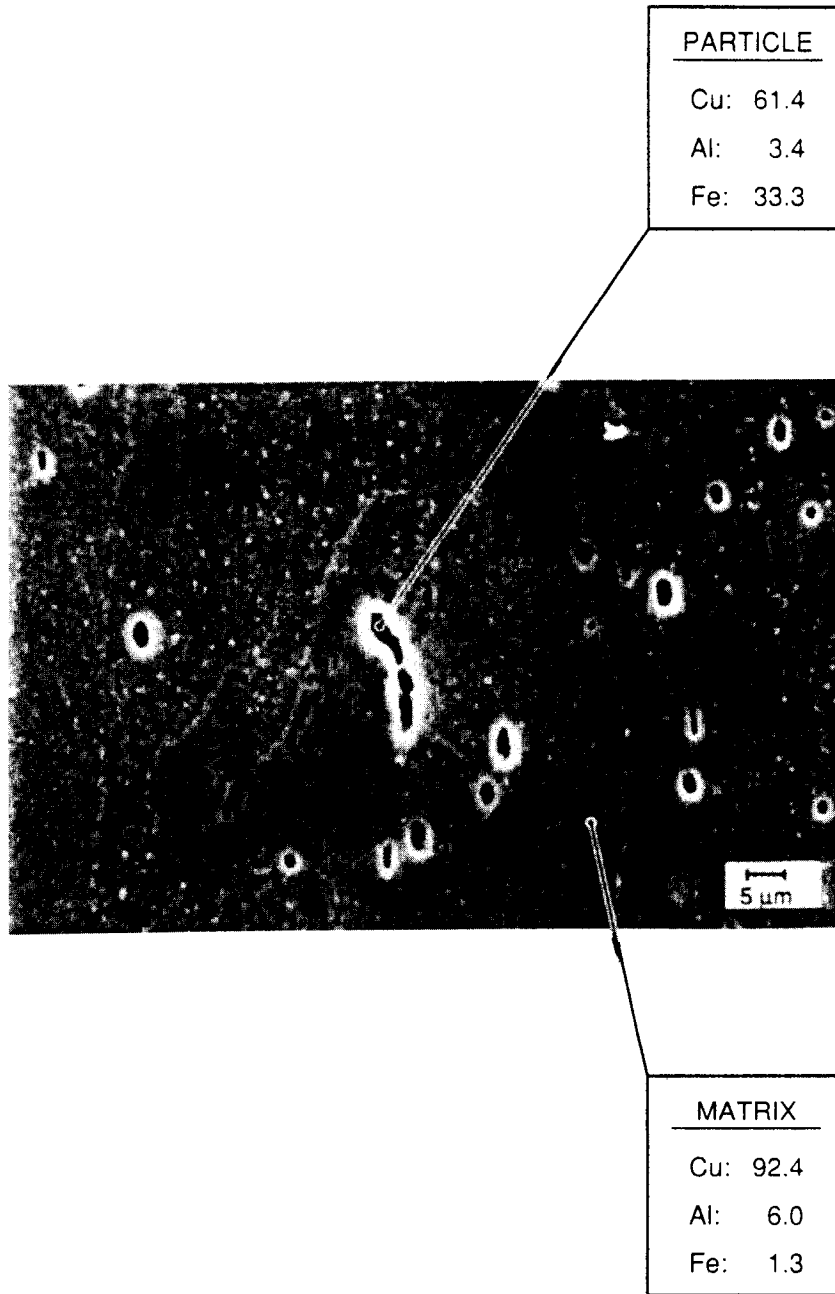


Figure 5.1. SEM-EDX analysis of polished and etched CDA-613 alloy

5.3.1.2 Corrosion Tests in Standard Solutions

The purpose of these tests was twofold: (1) to ensure that the starting conditions of the materials were appropriate, that is, the materials as supplied were not sensitized, and (2) to determine if the variations in surface composition or microstructure affected performance in standard tests. The test method chosen was ASTM A-262, Practice B, for the stainless steels and ASTM G-28, Practice A, for the Ni-base alloys (Incoloy 825 and Hastelloy C-22). Both these tests involved immersing the samples in a boiling solution of 50 percent (wt.) sulfuric acid + 42 g/l ferric sulfate. In the case of AISI 304L and 316L stainless steels and Incoloy 825, the immersion time was 120 hours. Hastelloy alloy C-22 was tested for 24 hours. Weight-loss determinations were made at the end of the immersion period; and from the weight-loss values and measured sample areas, equivalent corrosion rates were determined. Duplicate samples were tested for each condition, and average corrosion rates are plotted in Figure 5-2. The corrosion rates of polished samples (which is the recommended method of testing in the ASTM standards) of all the alloys except Incoloy 825 agree quite closely with published values in the literature (Streicher, 1958, Craig, 1989). The measured values for Incoloy 825 are considerably lower than that of published values (Brown, 1969). This difference can be explained by the fact that the alloy's composition has been modified since 1969 and is currently melted with higher chromium and lower carbon than before. Since the ASTM G-28A test involves an oxidizing environment, the higher chromium content in the current alloy can be expected to result in lower corrosion rates.

It is interesting to compare Figures 5-2 and 5-3. The samples of Incoloy 825 and Hastelloy alloy C-22 in the as-received surface condition exhibited higher corrosion rates than those with polished surface. These results corroborate the observed chromium depletion in the case of these two alloys (Figure 5-3). The differences between the two surface conditions for AISI 304L and 316L stainless steels are not as large, again in agreement with the lack of significant chromium depletion in these alloys. Polishing (to 120-grit finish) removes the depleted layer substantially and hence decreases the corrosion rate.

This factor will be considered in future long-term localized corrosion and stress corrosion cracking studies. The current results may be used as the basis for future quality control specifications.

5.3.1.3 Electrochemical Characterization of Materials

Verification Tests. The verification tests were performed in accordance with ASTM G-5 and ASTM G-61 procedures. The purpose is to assure the performance of the electrochemical system. The ASTM G-5 test is performed in a 1N sulfuric acid solution at room temperature on a type 430 stainless steel sample supplied by ASTM. The ASTM G-61 test is performed in a 3.56-percent (wt.) NaCl solution at room temperature on a 304L stainless steel sample. The resulting curves agreed well with the curves published by ASTM. Technical operating procedures were written (CNWRA TOP-008 and TOP-009) to include these standard tests at the beginning and end of every set of tests.

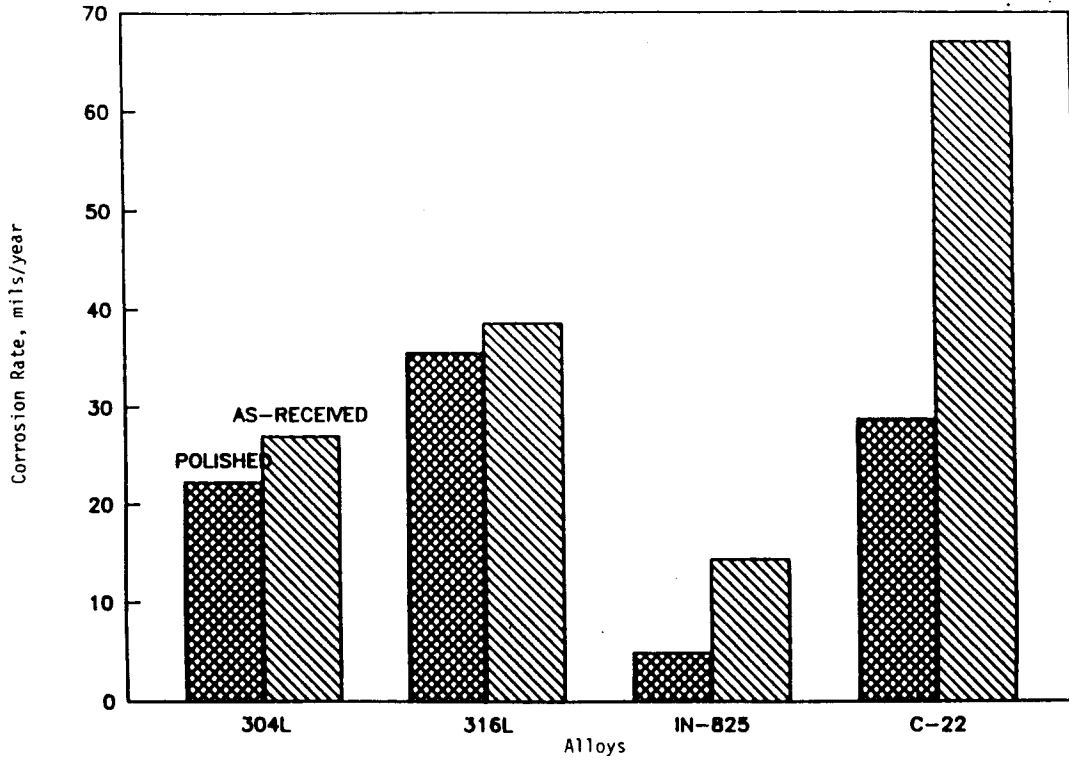


Figure 5-2. ASTM A-262 B test results. Corrosion rate vs. surface condition.

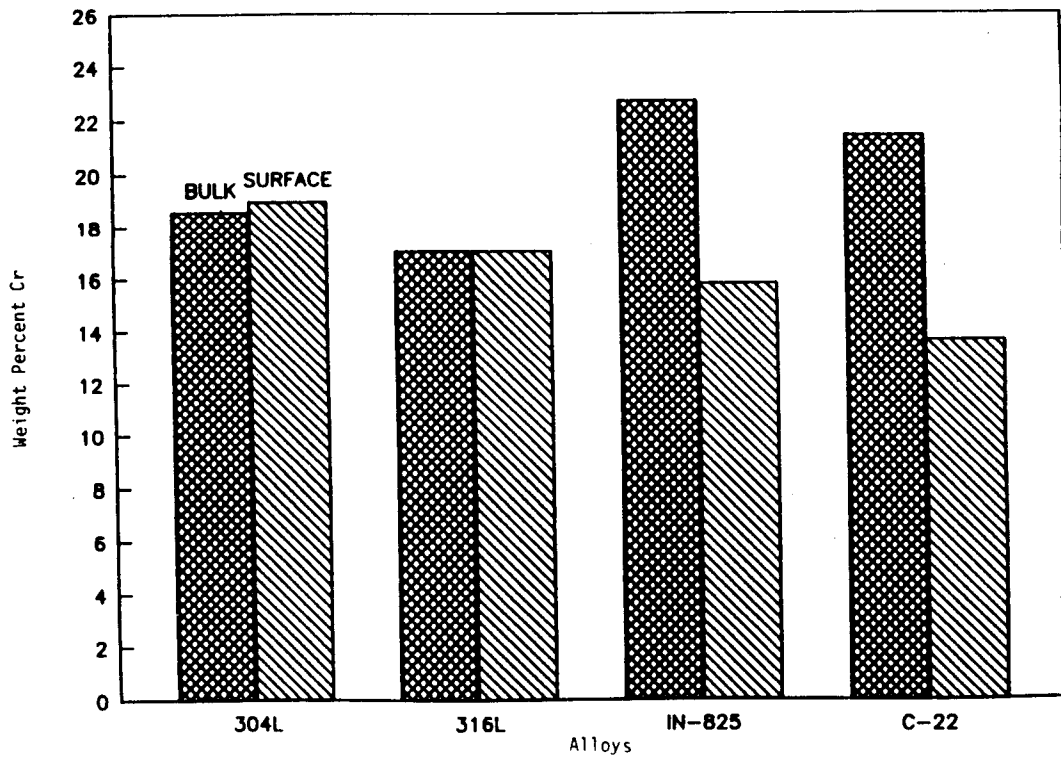


Figure 5-3. Surface Cr depletion. SEM-EDX analysis on 0.5-in. (1.3-cm) plates.

Development of J-13 Water Preparation Procedures. Through the investigations of Pabalan (Pabalan, 1989), it was found that the procedures used by Battelle and Cortest in the preparation of simulated J-13 water for corrosion tests can lead to higher chloride level than found in natural J-13 water. This was because HCL was added to control the initial pH. Further, it was concluded that because of the slow dissolution of silicic acid ($\text{SiO}_2 \cdot n\text{H}_2\text{O}$) and the unknown water of hydration, the concentration of silicon in the resulting solution was unknown and varying with time. The pH of the solution also varied with time and attained a pH of about 8 in equilibrium with atmospheric CO_2 partial pressure irrespective of how the pH was controlled initially at 7. To avoid the above mentioned difficulties, the procedure was modified; and a new technical operating procedure (TOP) was instituted (CNWRA TOP-010). The pH was allowed to assume natural values and measured before and after the tests. Silicic acid was not added. However, since silicon is a dominant species in terms of concentration in the natural J-13 water, separate experiments are underway to study the effect of silicon on localized corrosion. Sodium metasilicate, which is much more soluble than silicic acid, will be used in this case.

Effect of Chloride Content on Electrochemical Response of Incoloy 825. Much of the testing reported in the literature concerning the localized corrosion behavior of Incoloy 825 in simulated J-13 water has been performed at two chloride levels, namely, 6 and 1000 ppm. However, the response curve of this alloy with respect to chloride concentration can only be deduced by performing tests at intermediate chloride levels. Additionally, since pitting is a stochastic process, it is of interest to determine the variability of the process with respect to chloride content. Hence, cyclic, potentiodynamic polarization tests were carried out on multiple samples of Incoloy 825 in simulated J-13 water with a chloride level of 6 ppm and the same solution augmented in chloride level to 20, 100, 200, 300, and 1000 ppm. The 6-ppm solution represents the chloride content of the natural J-13 water. The 20-ppm chloride solution represents the chloride content of the simulated J-13 solution prepared by the Battelle procedure. The chloride content of the pore water from unsaturated tuff has been shown to range from 34 to 105 ppm (Glassley, 1990). The CNWRA TOP-010 was used in the preparation of the solutions. Potassium chloride was used to enhance the chloride concentration where necessary. The CNWRA TOP-003 was used for preparing the samples, and TOP-008 was used for conducting the polarization tests.

The results of cyclic polarization tests are shown in Table 5-4. An example of a polarization curve is shown in Figure 5-4. Several features are worthy of note in this figure. The corrosion potential is relatively low, which is indicative of well deaerated conditions. The average value of the corrosion potential was -573 mV versus saturated calomel electrode (SCE) with a standard deviation of 48.6 mV. The initial pH was also quite reproducible with an average value of 8.24 and a standard deviation of 0.1. Following the initial passive region, a secondary anodic peak was observed at approximately 277 to 382 mV versus SCE. The peak potential was a function of ionic content (conductivity) but not a function of chloride level, since the peak was present even in a nonchloride environment. The peak has been observed in the case of Hastelloy alloy C-22, but not in the case of AISI 304L and 316L stainless steels. Although various speculations exist regarding the cause of this peak, no particular mechanism has been established clearly.

Table 5-4

**RESULTS OF CYCLIC POLARIZATION TESTS ON INCOLOY ALLOY 825 IN SIMULATED
J-13 SOLUTIONS MODIFIED TO VARIOUS CHLORIDE LEVELS**

Test No.	Chloride ppm	E pit mV vs. SCE	E peak mV vs. SCE	E prot mV vs. SCE	E corr mV vs. SCE	(E pit- Eprot) mV	Initial pH	Final pH
34	0	783	382	741	-579	42	8.31	9.73
27	6	767	377	717	-480	50	8.23	9.78
30	6	768	355	706	-522	62	8.31	9.69
32	6	760	351	698	-534	62	8.30	9.76
33	6	743	322	685	-547	58	8.21	9.85
29	6	769	356	705	-557	64	8.30	9.61
31	6	747	322	681	-527	66	8.32	9.89
24	20	736	327	675	-570	61	8.31	9.86
8	20	773	380	707	-565	66	8.28	9.61
14	20	735	339	687	-470	48	8.30	9.85
22	20	739	335	683	-506	56	8.34	9.72
21	20	738	349	682	-588	56	8.28	9.56
23	20	761	352	697	-573	64	8.29	9.50
12	20	646	374	121	-543	525	8.27	9.48
16	100	740	323	366	-542	374	8.30	9.65
19	100	729	316	669	-637	60	8.25	9.72
9	100	754	361	688	-576	66	8.05	9.59
18	100	742	341	656	-592	86	8.32	9.64
17	100	726	329	672	-520	54	8.23	9.71
15	100	739	350	417	-563	322	8.30	9.66
20	100	739	334	309	-571	430	8.26	9.56
26	200	728	315	415	-526	313	8.40	9.85
10	200	746	353	152	-600	594	8.05	9.52
13	200	723	334	377	-579	346	8.27	9.67
25	200	740	335	335	-546	405	8.28	9.70
11	300	579	347	34	-566	545	8.05	9.52
47	300	628	316	103	-589	525	8.32	9.52
48	300	729	320	51	-585	678	8.38	9.41
5	1000	691	282	-35	-655	726	8.08	9.50
3	1000	699	294	-46	-647	745	8.12	9.49
4	1000	679	298	-63	-631	742	8.11	9.49
6	1000	467	291	-26	-610	493	8.10	9.48
2	1000	669	284	135	-657	534	8.09	9.71
1	1000	682	277	-48	-668	730	8.14	9.66
7	1000	699	306	-42	-643	741	8.11	9.65

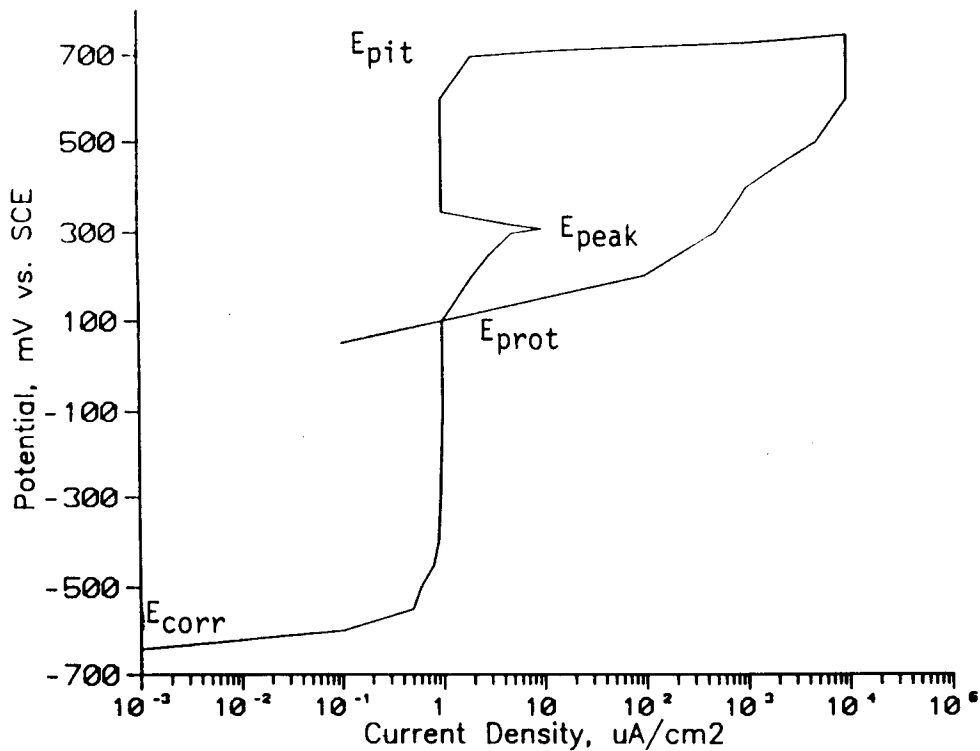


Figure 5-4. Sample curve from a cyclic polarization test

Following the peak, a rapid increase in current density was noted above a potential termed as "pitting potential, E_{pit} ." The term E_{pit} can be misleading in some cases because, as indicated in Table 5-1, no pitting was observed in some environments when the sample was examined visually (at 40X) after the test. In the cases where no pitting was observed, this potential must be considered to be only that due to oxygen evolution. In other cases, pitting was observed at the end of the test; but the potential at which increase in current density was observed was close to the oxygen evolution potential. Hence, both processes took place simultaneously. In addition, crevice corrosion also occurred in borderline cases. On reversing the direction of scan of the potential, the return curve exhibited varying degrees of hysteresis. In tests where pitting or crevice corrosion occurred, the hysteresis was significant. In others, no significant hysteresis was observed; but this has not always been the case. In other test programs currently underway at CNWRA, considerable hysteresis has been present without any localized corrosion.

The above observations emphasize the need to monitor the sample visually and not rely only on the electrochemical response. The point of intersection of the reverse curve with the forward curve is called the protection or repassivation potential, E_{prot} . It has been argued, based on short-term test results, that below this potential any pit already nucleated will repassivate; and thus the alloy will be protected from localized corrosion. As mentioned in the IWPE Program Plan - Revision 2, this assertion needs verification for long-term exposure.

The data generated are presented in Figure 5-5. Samples where pitting or crevice corrosion were observed at 40X magnification are shown in the figure. In the

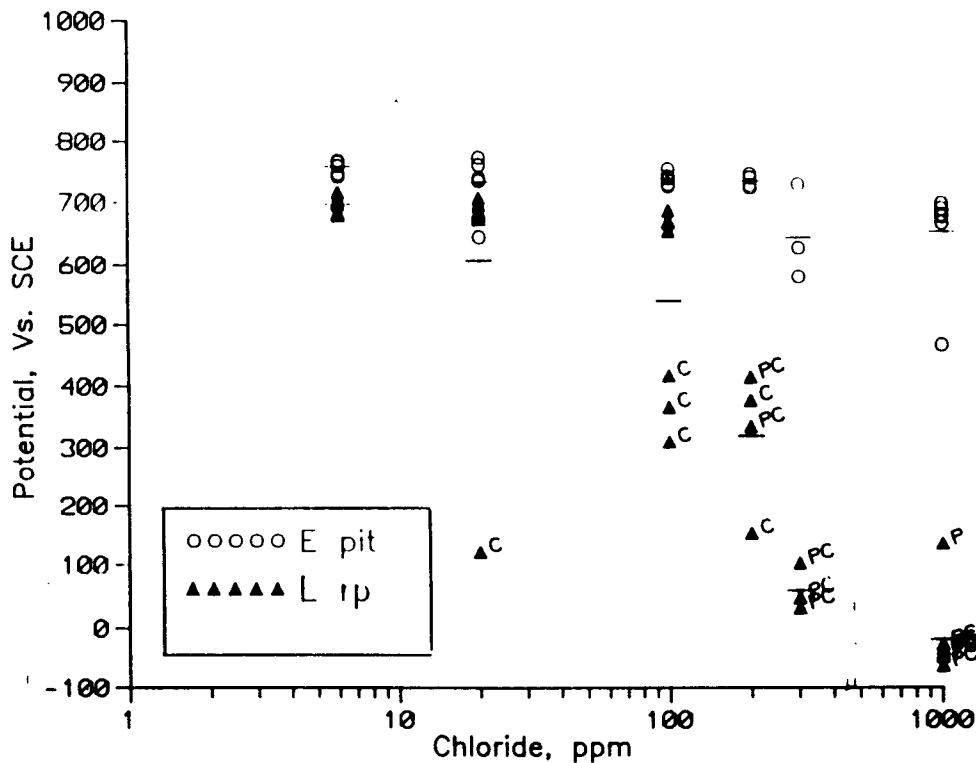


Figure 5-5. Effect of chloride in simulated J-13 water on pitting of Incoloy 825 (P=pit, C=crevice attack)

simulated J-13 water containing 6-ppm chloride, which most closely resembles the natural environment, none of the seven samples tested showed pitting or crevice corrosion. This finding is similar to those of others and to the results from previous tests at the CNWRA (Sridhar, 1990). In the simulated J-13 water augmented with chloride to 1000 ppm, all the tested samples pitted again, reinforcing previous results. In the solutions with 20- to 300-ppm chloride, pitting and crevice corrosion occurred in varying proportions of the samples. In the 20-ppm chloride solution, crevice corrosion occurred only on one of seven samples tested. In the 100-ppm solution, more samples showed crevice corrosion. Both pitting and crevice corrosion were observed in the higher chloride solutions. This environmental response can be compared to that of AISI 304L stainless steel, which is shown in Figure 5-6. These data are a collection of previously reported data (Sridhar, 1990). In terms of the response to chloride content, Incoloy 825 is only slightly better than 304L stainless steel. More samples of 304L stainless steel pitted in the 20-ppm solution. The behavior of 304L stainless steel in higher chloride solutions within the 20- to 100-ppm range needs to be evaluated further.

5.3.2 Metallurgical Stability of Container Materials in the Tuff Repository Environment

Within this task to investigate the metallurgical stability of container materials in the tuff repository environment, the main activities have been confined to studies of hydrogen absorption and embrittlement. These studies are an ongoing project at Ohio

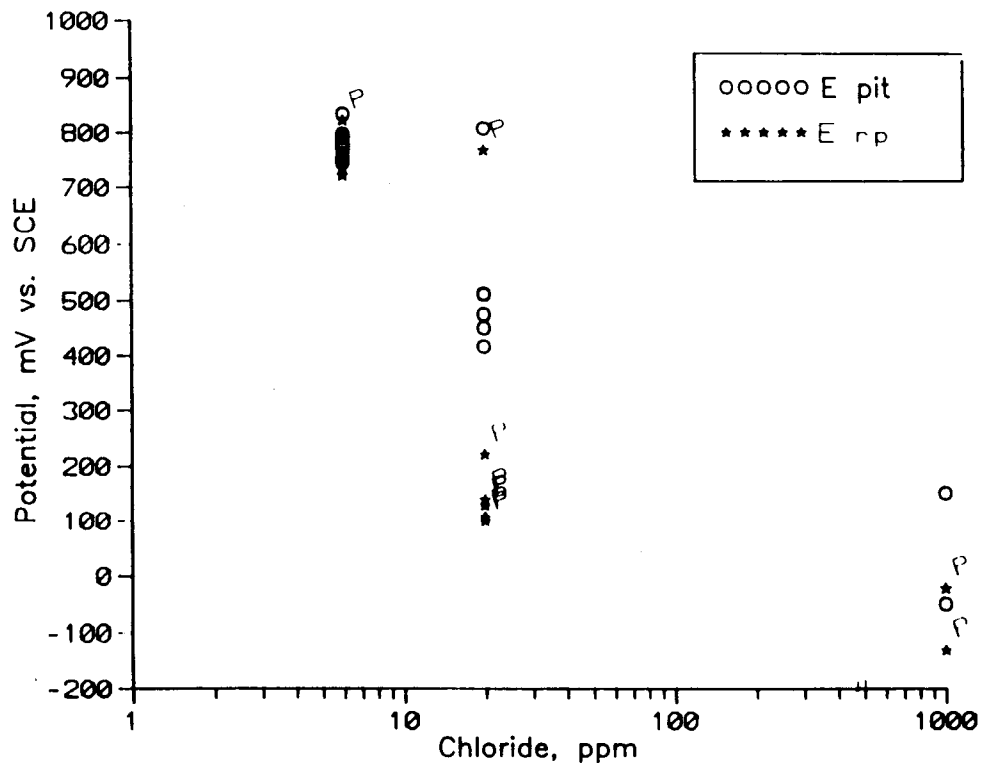


Figure 5-6. Effect of chloride in simulated J-13 water on pitting of 304L stainless steel (P=pits)

State University's Fontana Corrosion Center under the direction of Professor Bryan Wilde, and work to date is discussed in this section.

Hydrogen embrittlement is a potential degradation mode for some of the container materials and has received scant attention. Possible mechanisms for the generation of hydrogen are galvanic coupling of the container and liner materials and radiolysis of water. While this degradation mode is not currently considered to be of major importance, it is believed that suitable test techniques must be put in place to quantify the embrittlement susceptibility. The investigations thus far have focused on the development of techniques to characterize the hydrogen permeation rate in various candidate container materials.

Electrochemical permeation techniques developed originally by Devanathan and Stachurski (Devanathan, 1962) are being used to measure the hydrogen permeation rates. The technique involves the measurement of these rates through a foil of the candidate material. Hydrogen is evolved cathodically on one side of the foil and is oxidized on the other side by the application of a suitable anodic potential that minimizes dissolution. The oxidation (anodic) current density remains low until hydrogen arrives at the anodic side, after which current density rises in proportion to the flux of hydrogen permeating through the foil. Hence, the rise transients can be used to calculate the diffusivity of hydrogen.

Hydrogen permeation tests on the austenitic materials--AISI 316L stainless steel, Incoloy 825, and Hastelloy C-22--have been completed. The results of these tests were reported in the CNWRA *Intermediate Milestone Report* (Sridhar, 1990). The measured diffusivity values for these three materials agreed quite closely with the literature values, as shown in Table 5-5. Subsequent to this report, permeation tests have been conducted on some of the copper-based alloys. In the case of CDA-102 (oxygen-free high-conductivity copper), no hydrogen permeation was detected within the time frame of the test (200 hours). The low permeability (which is a product of diffusivity and solubility) may reflect the difficulty of absorbing hydrogen (low solubility) in this material, since literature data (Hagi, 1986, DeWulf, 1985) suggest that the diffusivity of hydrogen in copper is about the same order of magnitude as in the austenitic alloys. The diffusivity of hydrogen measured for the cupronickel alloy (CDA-715) is shown in Table 5-5, together with data for the other alloys previously reported.

Table 5-5

**DIFFUSIVITY OF HYDROGEN IN CANDIDATE CONTAINER MATERIALS
MEASURED BY THE ELECTROLYTIC PERMEATION TECHNIQUE**

MATERIAL	HYDROGEN DIFFUSIVITY AT 95°C
Hastelloy alloy C-22	$4.5 \times 10^{-10} \text{cm}^2/\text{sec}$
Incoloy alloy 825	$8.6 \times 10^{-11} \text{cm}^2/\text{sec}$
316L stainless steel	$1.3 \times 10^{-10} \text{cm}^2/\text{sec}$
CDA-715 (Cu-30%Ni)	$6.0 \times 10^{-10} \text{cm}^2/\text{sec}$

These measurements established the feasibility of using this technique to measure hydrogen permeation rates at 95°C. Further work will focus on extending the technique to measurements in simulated J-13 water and similar environments at temperatures higher than 95°C. Additionally, the effect of applied stress on hydrogen permeation will be examined. Finally, the effect of absorbed hydrogen on the mechanical properties of the materials will be examined through the use of slow-strain-rate tests.

5.4 SUMMARY OF RESULTS

Observations to this point indicate several areas of concern:

- (1) The presence of iron-rich particles in CDA-613 may lead to preferential corrosion due to the electrochemical dissimilarity of these particles and the copper-rich matrix. Future investigations of the alloy should consider this aspect in greater detail.

- (2) Chromium depletion at the surface of the nickel-based, chromium-containing alloys led to increased corrosion in a standard oxidizing environment. Hence, the effect of the depletion on the container performance should be considered both for general and localized corrosion processes, particularly for stress-corrosion cracking.
- (3) The threshold chloride level for localized corrosion of Incoloy 825 in aqueous environments is quite low (20 to 100 ppm).
- (4) Crevice corrosion occurred prior to pitting in many samples of Incoloy 825 exposed to chloride solutions. Crevice corrosion is an important failure mode and should be examined more systematically.
- (5) Near the threshold chloride levels when localized corrosion initiates, considerable scatter in data is observed. The statistical distribution of the parameters is not the same throughout the environmental space.
- (6) Hydrogen permeation tests performed in 0.1N NaOH at 95°C have resulted in values of hydrogen diffusivities in AISI 316L stainless steel, Incoloy 825, Hastelloy C-22, and CDA-715 comparable to values reported in the literature for similar materials. Further investigations will continue in simulated repository environments

5.5 REFERENCES

- Beavers, J. A., and C. L. Durr. 1990. Container corrosion in high level nuclear waste repositories. *First Semiannual Report, Year 3, September 1989 - February 1990*. Contract No. NRC-04-87-069. Columbus, Ohio: Cortest Columbus, Inc.
- Brezina, P. 1982. Heat treatment of complex aluminum bronzes. *International Metals Reviews* 27(2):77.
- Brown, M. H. The relationship of heat treatment to the corrosion resistance of stainless alloys. *Corrosion* 25(10):438.
- Craig, B., ed. 1989. *Handbook of Corrosion Data*. Metals Park, Ohio: American Society for Metals (ASM) International:605.
- Devanathan, M. A., and A. Stachurski. 1962. *Proceedings of Royal Society of London*. A270:90. London: Royal Society:90.
- Dewulf, D. W., and A. J. Bard. 1985. Electrochemical determination of hydrogen transport through copper. *J. Electrochem. Soc.* 132(12):2965-2967.
- Glass, R. S., G. E. Overturf, R. E. Garrison, and R. D. McCright. June 1989. *Electrochemical Determination on the Corrosion Behavior of Candidate Alloys Proposed for Containment of High Level Nuclear Waste in Tuff*. UCID-20174. Livermore, California: Lawrence Livermore National Laboratory (LLNL).

- Glassley, W. E. January 1990. Geochemical interactions. Presentation to the Nuclear Waste Technical Review Board. Livermore, California: LLNL.
- Hagi, H. 1986. Diffusion coefficients of hydrogen in Ni-Cu and Ni-Co alloys. *Transactions of Japanese Institute of Metals* 27(4):233-240.
- Ijsseling, F. P. 1980. Electrochemical methods in crevice corrosion testing. *Br. Corrosion J.* 15:51.
- McCright, R. D., H. Wiss, M. C. Juhas, and R. W. Logan. 1984. Selection of candidate canister materials for high-level nuclear waste containment in a tuff repository. *CORROSION 84*. Paper No. 198. Houston, Texas: National Association of Corrosion Engineers.
- Pabalan, R. August 10, 1989. Test of technical procedure for preparing simulated and modified J-13 well water. Internal CNWRA Memorandum. San Antonio, Texas: CNWRA.
- Sedriks, A. J. 1979. *Corrosion of Stainless Steels*. New York: J. Wiley & Sons.
- Sedriks, A. J. 1982. Corrosion resistance of austenitic Fe-Cr-Ni-Mo alloys in marine environments. *International Metal Reviews* 27:321.
- Sridhar, N., G. Cragolino, and F. F. Lyle. June 5, 1990. *Progress Report of Activities and Recommendations in the Integrated Waste Package Experimental Program, May 1988 - April 1990*. CNWRA Intermediate Milestone Report 20-3704-042-005-900, NRC Contract 02-88-005. San Antonio, Texas: CNWRA.
- Streicher, M. A. April 1958. *Intergranular Corrosion Resistance of Austenitic Stainless Steels*. American Society for Testing and Materials (ASTM) Bulletin No. 229. Philadelphia, Pennsylvania: ASTM:77.
- West, E. G. 1982. *Copper and Its Alloys*. Published by Ellis Harwood Ltd. New York: John Wiley & Sons.

6. STOCHASTIC ANALYSIS OF UNSATURATED FLOW AND TRANSPORT

by Rachid Ababou

Investigator: Rachid Ababou (CNWRA)

6.1 TECHNICAL OBJECTIVES

A quantitative characterization of large-scale flow and radionuclide transport through the heterogeneous unsaturated fractured rock of Yucca Mountain will be necessary to evaluate compliance with the siting criteria and performance objectives associated with the proposed Yucca Mountain HLW repository 10 CFR Parts 60.122 and 60.113. The pertinent technical issues concerning radionuclide migration at Yucca Mountain will need to be understood so as to demonstrate that the hydrogeologic conditions at the repository site strongly inhibits radionuclide transport to the accessible environment and meets performance criteria. Realistic modeling of the complex, heterogeneous flow and transport processes at Yucca Mountain may require incorporating the effects of relatively small-scale space-time variability in modeling large-scale unsaturated flow and radionuclide transport. This constitutes one of the main areas of investigation of this research project (entitled Stochastic Analysis of Large-Scale Flow and Transport in Unsaturated Fractured Rock).

The specific objectives of the project are to: perform a review of the literature and assess available models and data relevant to the subject site; select a global approach to model large-scale flow and transport in unsaturated fractured rock; develop submodels for incorporation into the global model; and perform large-scale simulations and participate in the validation of flow/transport models for the Yucca Mountain repository.

The project plan was revised and issued on August 2, 1990. The project is divided in three tasks: "Review, Analysis, and Development of Modeling Approach," including Task 1, "Literature Review of Modeling Approaches"; Task 2, "Preliminary Data Review and Assessment"; and Task 3, "Selection and Initial Development of Global Modeling Approach." The complete results of the literature review, initial data assessment, model selection, and first stages of model development will be presented in the Technical Report for Task 1, due in October 1990.

6.2 RESEARCH ACCOMPLISHMENTS

The overall rationale of the project and preliminary research areas were developed succinctly in the previous quarterly report (literature review and models assessment, hydrodynamic data and statistical correlations, supercomputer modeling and 3D data visualization, and numerical issues with nonlinearity and random-type heterogeneity). In this quarterly report, ongoing work and results obtained in some of the above research areas are discussed.

6.2.1 Three-Dimensional Synthetic-Flow Experiment

The use of 3D color-graphics visualization tools for analyzing the spreading pattern of a synthetic moisture plume in a randomly heterogeneous and imperfectly stratified soil was demonstrated. This work was part of our initial involvement in INTRAVAL model validation activities. A draft of a section of the INTRAVAL Phase II report, written by R. Ababou, has now been completed. This section, entitled "High-Resolution Modeling of Strip Source Infiltration: Three-Dimensional Synthetic Experiment Analogous to the Las Cruces Trench Experiment" and currently pending publication, is given in full in Appendix A. It describes in some detail the modeling and 3D data-processing work accomplished so far, and suggests future directions in model validation such as conditional synthetic experiments.

6.2.2 Numerical Analysis of Nonlinear Unsaturated Flow

In the course of the project's research on modeling approaches, focus initially was on the numerical difficulty of the unsaturated flow equation and specifically on the numerical effects of nonlinearity, competition between capillary diffusion and gravity drainage, and convergence of nonlinear iterations. This work by R. Ababou was recently published in the *Proceedings of the Eighth Conference on Computational Methods in Water Resources, Computational Mechanics Publications*, Vol. A, pp. 151-160, June 1990, under the title "Numerical Analysis of Nonlinear Unsaturated Flow Equations." Because the proceedings are not widely available and were published during the reporting period, this paper is made available in Appendix B. This work will continue by extending the nonlinear numerical analysis to both heterogeneous and fractured porous media.

6.2.3 Unsaturated Coefficients and Statistical Correlations

Progress was made in identifying the implications of statistical cross correlations among saturated and unsaturated hydrodynamic parameters. By investigating randomly generated unsaturated conductivity curves, and analyzing the family of curves by theoretical as well as empirical means, the existence of a crossing point at a certain characteristic pressure and the existence of an envelope were determined. Work is in progress to formalize the theory. Hopefully, these results can be used to simplify statistical characterization of naturally heterogeneous and fractured porous media, such as the Yucca Mountain fractured tuff.

7. GEOCHEMICAL NATURAL ANALOGS

by English C. Percy

Investigators: William M. Murphy (CNWRA) and English C. Percy (CNWRA)

7.1 TECHNICAL OBJECTIVES

The Geochemical Natural Analogs project is designed to provide background on previous and current natural analog studies applied to contaminant transport. As part of this project, a geochemical natural analog study will be made of contaminant transport relevant to the proposed repository at Yucca Mountain. This study will provide fundamental, new data for time and space scales generally inaccessible in laboratory studies and will aid validation of predictive models for geochemical transport.

Initial work on this project has focused on a literature survey, identified as Task 1. The first objective of this task, to participate in a technical workshop on the use of natural analogs, has been completed. Compilation and evaluation of literature on research conducted on natural analogs relevant to contaminant transport at the candidate HLW repository at Yucca Mountain is in progress. Also ongoing is a review of literature on potential sites for a natural analog study to be undertaken in the future. Evaluation of these sites is in progress with respect to the degree of relevance to understanding contaminant transport at Yucca Mountain, the possibility of constraining initial and boundary conditions, the feasibility of research at the sites, and the potential usefulness for unsaturated-zone contaminant-transport model validation. Discussion about these Task 1 efforts is presented in the following sections.

7.2 ACTIVITY THIS PERIOD IN TASK 1

7.2.1 Technical Presentation and Literature Review

A poster titled "Possible Analog Research Sites for the Proposed High-Level Nuclear Waste Repository in Hydrologically Unsaturated Tuff at Yucca Mountain, Nevada" was presented at the Natural Analog Working Group meeting in Pitlochry, Scotland. A draft paper summarizing the presentation comprises the substance of this quarterly report.

Work also continued on literature identification and review. Relevant references from the published literature were compiled, acquired, read, and evaluated. A total of 284 pertinent references have been identified, hard copies of 201 have been obtained, and 163 have been reviewed. The literature was searched for a variety of natural analog applications which have been proposed and executed. Reviews are continuing on additional references containing information on analog sites that may have geochemical transport aspects appropriate for comparison with Yucca Mountain. In addition, the literature reviewed contains pertinent information on criteria for selecting potential sites for a natural analog study relevant to Yucca Mountain.

7.2.2 Possible Sites for Geochemical Analog Research

A variety of analogs of the proposed Yucca Mountain repository system has been considered including the warm and hot springs of the Yellowstone geyser system in Wyoming (e.g., DOE, 1988) and interflow thermal effects at the Valles Caldera, New Mexico (Krumhansl and Stockman, 1988). Alexander and Van Luik (1990) summarized DOE natural analog studies for the Yucca Mountain site, and proposed research on radionuclide transport at the uranium deposits in the McDermitt Caldera on the Nevada-Oregon border. Another intriguing set of analogs is the environments of underground explosions of test nuclear devices on the Nevada Test Site (NTS). Some of these tests have been in the hydrologically unsaturated zone of lithologically similar rocks. Studies of the transport of radionuclides from other test sites at the NTS have revealed important results such as the negligible retardation of Ru-106 (Coles and Ramspott, 1981) and I-129 migration rates, which exceed that of tritium (Thompson, 1985).

Because they share many features essential to nuclear-waste migration phenomena, the geologic settings of the Peña Blanca deposits in the Chihuahua City uranium province, Mexico, and the Akrotiri Peninsula archaeological site on Santorini, Greece, can be regarded as analogs of the Yucca Mountain repository system. Research at these sites could permit identification and characterization of processes that would occur as radionuclides are released from the candidate repository to the geologic environment, and could aid in the development and validation of predictive models for the evolution of the Yucca Mountain repository which are essential for licensing. The object of this paper is to illustrate similarities among Yucca Mountain, Peña Blanca, and Santorini, with particular reference to processes of alteration and transport of analogs of radioactive contaminants in the geologic environment.

7.2.2.1 *Yucca Mountain, Nevada*

Yucca Mountain is 150 km northwest of Las Vegas, Nevada, on federal land including part of the NTS. Geologic information about the Yucca Mountain area has been gathered since the early 1900s. Work was initially directed toward mineral and energy resource exploration; more recently, studies have been connected with government activities at the NTS. Since 1977, the DOE has gathered considerable information on Yucca Mountain, and the following information is drawn largely from that collection (e.g., DOE, 1988).

Yucca Mountain lies in a hydrologically closed basin in the southern part of the Great Basin physiographic province, which is bounded to the east by the Colorado Plateau and to the west by the Sierra Nevada Range. The Great Basin is a product of continental extension over the last 20 Ma and is characterized by north-south trending horsts and grabens, offset by widely spaced regional strike slip faults. The southern part of the basin is composed of heavily eroded tilted-block ranges and sediment-filled valleys. Tectonic features near Yucca Mountain are dominated by normal faults and other extensional structures. Yucca Mountain consists of a series of north-trending structural blocks, which have been tilted eastward by west-dipping, high-angle normal faults related to Basin and Range tectonism over the last 7 Ma.

At Yucca Mountain, a series of silicic volcanic units with a thickness ranging from 1 to 3 km rests on Silurian dolomite. These volcanic rocks are variably welded, devitrified, and altered ash-flow and air-fall tuffs with minor volcanic flows and breccias. The oldest of the silicic volcanic units at Yucca Mountain was deposited about 14 Ma ago, and the youngest is about 12 Ma old. Subsequent small-scale basaltic volcanism has occurred near Yucca Mountain episodically into the Pleistocene Epoch.

The proposed repository horizon is in a devitrified rhyolite ash-flow tuff unit in the Topopah Spring Member of the Paintbrush Tuff, which was deposited 12 to 13 Ma ago and is about 300 m thick at Yucca Mountain. The basal-welded vitrophyre of the Topopah Spring Member grades upward into a densely welded, devitrified, nonlithophysal zone from 27 to 56 m thick, which is the proposed location of the repository. This zone is phenocryst poor (2 -22 percent); the phenocrysts include sanidine; plagioclase (andesine to oligoclase); and minor quartz, biotite, amphibole, allanite, zircon, and iron-titanium oxides. The primary groundmass of the Topopah Spring Member is glass and/or devitrification products comprising alkali feldspar and silica minerals. Smectite and the silica-rich zeolite minerals clinoptilolite and mordenite are dominant alteration products. In some areas primary glass is completely converted to zeolites. Overall, the Topopah Spring Member averages about 70- to 800-percent SiO₂ (Byers, 1985). Approximately 10 m beneath the Topopah Spring Member is a layer 30 to 300 m thick, which is locally rich in zeolites (60 to 80 percent clinoptilolite and mordenite).

The saturated-zone groundwaters from tuffaceous aquifers at Yucca Mountain are dilute ($<10^{-2}$ m), oxidizing, sodium bicarbonate solutions, rich in silica, with lesser calcium, potassium, magnesium, chloride, sulfate, nitrate, and fluoride. Information about the pore waters in the unsaturated zone is limited at this time. The proposed repository horizon is about 200 m above the water table in rocks with porosity that is thought to be 40 to 70 percent saturated with water. In this low-pressure medium, water would vaporize as the temperature increases in the near field. Water movement in the unsaturated zone is thought to be slow (e.g. 0.5 mm/yr) if it is dominated by matrix flow. The chemistry, distribution, and behavior of water in unsaturated, fractured tuffs are incompletely understood, particularly under conditions of thermal perturbations, and are currently a subject of investigation.

Yucca Mountain is in a midlatitude desert climate with average annual precipitation less than 15 cm and average temperature of about 13°C. Only about 0.3 percent of the local precipitation is thought to penetrate to the deeper portions of the unsaturated zone. A variety of evidence (e.g., pack-rat middens and palynology) suggests that the climate has been arid to semiarid for the last 2 Ma. The aridity of the region results in little groundwater recharge and hence a low rate of groundwater movement. The groundwater in southern Nevada does not discharge into rivers or large bodies of surface water; rather, it discharges by evapotranspiration (e.g., at Alkali Flats, California) and at springs (e.g., at Death Valley, California).

7.2.2.2 *Peña Blanca, Mexico*

The Peña Blanca district is in northern Mexico about 50 km north of Chihuahua City and is part of the Chihuahua City uranium province. Many of the uranium deposits in the district have been drilled or developed by underground or open-pit mining

over a period of 20 years (Goodell, 1981), but Peña Blanca has no mining activity at this time. Combined, these deposits include more than 2000 metric tons of U_3O_8 and constitute the bulk of Mexican uranium resources.

Peña Blanca is part of the northern Mexico basin and range system and lies near the boundary between a stable craton to the west and a more mobile belt to the east (Goodell, 1985). The regional structural province is bounded to the east by the Trans-Pecos Range and to the west by the Sierra Madre Occidental (George-Aniel et al., 1985). The Sierra Peña Blanca is a north-dipping horst block with a superimposed set of parallel northwest-striking normal (extensional) faults (Goodell, 1981).

Peña Blanca stratigraphy consists of a sequence of mid-Cretaceous (Albian to Cenomanian) limestones and mudstones on which a series of Tertiary silicic volcanics has been deposited (Cardenas-Flores, 1985). Host rocks for the uranium deposits are the Escuadra and Nopal Formations comprising outflow facies of variably welded tuffs with ignimbrite, vitrophyre, lahar, air-fall, and water-worked units. The preserved total thickness of the volcanic units varies over the Sierra Peña Blanca area from 106 to 538 m, and rock ages range from 44 Ma to 35 Ma (Goodell, 1981).

The Peña Blanca tuffs are generally devitrified rhyolitic ignimbrites consisting largely of glass devitrified to cristobalite and feldspar with quartz, sanidine and minor biotite phenocrysts (Cardenas-Flores, 1985). These tuffs have SiO_2 contents at 63 to 78 percent, Al_2O_3 at 11 to 14 percent, and K_2O at 4 to 7 percent (Goodell, 1981). Background uranium concentrations of the tuffs range from about 4 to 10 ppm (George-Aniel et al., 1985). Uranium in the ores was likely derived from the alteration of volcanic glass in the tuffs by convective hydrothermal groundwater systems. Uranium deposits, tentatively dated at 3.5 Ma, are commonly associated with minor hydrothermal alteration at faults, fractures, and breccias and are underlain by an extensive, unwelded, zeolitized tuff (part of the Nopal Formation). Fluid inclusion evidence suggests mineralization by low salinity (0 - 4.94 wt percent NaCl equiv.), moderate temperature (150 - 250°C) fluids (George-Aniel et al., 1985). The present uranium mineralization is predominantly uranyl silicates and vanadates (Goodell, 1981); however, the sparse occurrence of uraninite and other reduced phases (e.g., pyrite) indicates that original uranium (IV) mineralization has been oxidized. Some areas of Peña Blanca mineralization contain enough cesium to form margaritasite (Cs carnotite) $(Cs,K,H_3O)_2(UO_2)_2V_2O_8 \cdot H_2O$ (Wenrich et al., 1982) in addition to the uranium minerals.

The distribution of uranium indicates that mineralizing hydrothermal fluids circulated primarily in faults and fractures, although there is dispersed uranium mineralization in areas with low fracture permeability (Goodell, 1981), suggesting that matrix flow was important locally. Stratigraphic control appears to have been important to ore localization in all deposits, with characteristics such as secondary porosity, brecciated zones, and fissures controlling detailed ore distribution (Cardenas-Flores, 1985). There is general agreement that the ores were emplaced by a geothermal, convecting groundwater system (Goodell, 1981; Goodell, 1985; Cardenas-Flores, 1985) which may have had significant inputs of volcanic fluids (George-Aniel et al., 1985) in addition to dominant meteoric waters (Goodell, 1985).

All of the Peña Blanca uranium deposits are presently above the water table in the unsaturated zone. At present, uranium is being remobilized by oxidizing

meteoric groundwaters which episodically penetrate the deposits through fractures in the unsaturated tuffs. The climate in the Peña Blanca area is arid, with annual precipitation of about 24 cm and average annual temperature of 19°C.

Similarities between the geologic settings of the proposed HLW repository site at Yucca Mountain and the uranium deposits at Peña Blanca suggest that a variety of present and past processes at Peña Blanca are analogous to those that could affect radionuclide migration at Yucca Mountain. The oxidation of Peña Blanca uraninite, the resulting dispersion of uranium from the sites of original mineralization, and the formation of secondary uranyl silicates are analogous to processes that may affect spent nuclear fuel and elemental migration at the repository. The behavior of Cs in some of the ores may be analogous to that of Cs from HLW. Processes in the zeolitized horizon underlying the ore deposits at Peña Blanca may also constitute good analogs of radionuclide retardation in zeolitized tuffs at Yucca Mountain.

Information required for a thorough study of the Peña Blanca analog site includes primary and alteration mineralogies of the ores and host rocks. The spatial distributions of these minerals and their temporal relations must be ascertained. Knowledge of the chemical compositions of the ores and host rocks with regard to both major and trace elements, and especially the compositions of individual mineral phases within the ores and the distributions of important radionuclides and analog elements within the minerals are required. Determination of the hydrological relations in the area of the deposit both at the present and in the past are necessary. Groundwater compositions must be measured, including spatial variations.

The factors listed above are all measurable; however, as with many natural analogs, it may be difficult to place limits on the initial and boundary conditions for alteration and transport processes at Peña Blanca. The timing of the onset of oxidation of the ores is important to elemental migration studies and may remain uncertain. The original distribution of the uraninite and other ore constituents can only be inferred from the present distribution. Changes and durations of changes in the hydrology in the past may remain unknown. It is likely that the hydrothermal systems responsible for forming the ores have complex histories; it may be difficult to separate the variable hydrothermal alteration and remobilization of the ores from the effects of later meteoric fluids.

7.2.2.3 Santorini, Greece

The eruption at Stronghyle volcano in approximately 1645 B.C. (Hammer et al., 1987) buried a Minoan city under volcanic debris on what is now the Akrotiri peninsula on the island of Thera, Santorini. This event was one of the largest explosive eruptions in post-glacial time; a caldera with an area of 83 km² and a depth of 600 to 800 m was formed (Watkins et al., 1978). Since archaeological excavations began in 1967, much information has been unearthed regarding the archaeology and geology of the area. Investigations at the site are ongoing.

Santorini comprises a complex of volcanos located about 100 km north of Crete. Prior to the 1645 B.C. eruption, the single large island of Stronghyle occupied the area of the Santorini group. The great eruption destroyed Stronghyle and left the islands of Thera, Therasia, and Aspronisi as remnants. During the past 1800 years, the islands of Palea and Nea Kameni have formed in the caldera by submarine and subaerial volcanism

(Pichler and Kussmaul, 1980). All of the eruptions have been confined to a 3- to 4-km wide, northeast trending graben, which formed as a result of extension in the eastern Mediterranean over the past 10 Ma (Heiken and McCoy, 1984).

The oldest subaerial volcanic activity at Santorini deposited ash and pumice on Lower Tertiary phyllite basement approximately 1 Ma ago. Volcanic activity continued intermittently, depositing 30 to 90 m of pumice, ash, and lava flows on the island. The Minoan eruption buried settlements under 30 m of volcanic sediment (Pichler and Friedrich, 1980). Four phases of this eruption have been identified (Heiken and McCoy, 1984): (1) Plinian eruption with massive pumice fall; (2) phreatomagmatic base surge of fine ash and pumice lapilli; (3) phreatomagmatic eruption of pumice bombs, lithic fragments, and ash as well as distal mudflows; and (4) ignimbritic eruption, deposited at temperatures greater than 500°C (Wright, 1978). All of the Minoan eruption phases deposited pyroclasts of rhyodacitic composition (Heiken and McCoy, 1984). Paleosols are preserved in several places below the Minoan tuff and locally reach thicknesses of 3 to 4 m. These paleosols developed on the series of welded tuffs and ignimbrites upon which the buildings of Akrotiri (the largest of the known Minoan towns buried by the eruptions) were founded (Pichler and Friedrich, 1976).

The anthropological horizon at Akrotiri is located in the unsaturated zone above the groundwater table. In the semiarid climate, the mean annual precipitation is essentially equivalent to the estimated annual evapotranspiration loss (approximately 35 cm/year, mean air temperature is 17°C) (Marinos and Marinos, 1978). The hygroscopic character of the upper soil layers generally prevents deep infiltration of rain water even though the deeper soils appear to be permeable (Marinos and Marinos, 1978). In the Akrotiri area, steep-sided gullies have been cut into the tephra sequence by runoff after exceptionally heavy rains. Paleoclimatological data indicate that the climate on Santorini at the time of its eruption did not differ strongly from the present climate; air temperatures were slightly warmer, and the climate was slightly more arid (McCoy, 1980).

Elemental migration at the Akrotiri site, analogous to that which would occur at the Yucca Mountain repository, could possibly be well constrained chemically, temporally, and spatially using artifacts as analogs for contaminant sources. For example, numerous lead balance weights discovered at this site have distinct chemical compositions (Gale and Stos-Gale, 1981). Oxidation rinds developed on the lead weights (Petrucci, 1978) suggest that some components have been released during alteration. Artifacts therefore may constitute well-constrained point sources for dispersion of trace species analogous to migration of waste elements at Yucca Mountain. The known period of 3600 years between the eruption of Santorini and the present corresponds well to the time frame of interest in the evaluation of the HLW repositories. The rock types enclosing the archaeological site are similar to those at Yucca Mountain, and the climates and hydrological relations are comparable.

Information required for a detailed study of the Santorini analog site includes compositions of lead weights or other artifacts (major and trace elements). Mineralogy and composition of the alteration products of the artifacts (e.g., oxide coatings), and knowledge of the primary and alteration mineralogy of the rocks surrounding the artifacts are required. Bulk chemical compositions of the rocks surrounding the weights must be measured as a function of location, with particular emphasis on concentration

gradients of (trace) elements derived from the artifacts. Present and former hydrological relations in the area of the contaminant analogs and groundwater compositions (including local variations) are also of importance.

7.3 CONCLUSIONS

Uranium deposits at Peña Blanca, Mexico, and archaeological sites at Santorini, Greece, offer good analogs of processes that would be expected to occur in the geologic setting of the proposed HLW repository at Yucca Mountain, Nevada. The sites at both Peña Blanca and Santorini are in the hydrologically unsaturated zone of siliceous tuff sequences, and both sites occur in climates similar to that of southern Nevada. The past and present oxidation of uraninite at Peña Blanca constitutes an analog for the alteration of spent nuclear fuel. The processes of migration of uranium and other elements from sites of initial mineralization under unsaturated, oxidizing conditions at Peña Blanca are analogous to those that would occur in the Yucca Mountain repository. Studies using buried artifacts at the Santorini archaeological site as analogs of contaminant sources would permit analyses of the rates and mechanisms of trace elemental migration in a geologic setting analogous to Yucca Mountain. The initial and boundary conditions at Santorini could be especially well defined, and the time period since burial of the artifacts (3600 years) is comparable to the period of interest in radioactive waste management.

Though Peña Blanca and Santorini provide good analogs to some processes important to HLW containment, there are no perfect analogs. The source term and boundary conditions at Peña Blanca may be difficult to constrain closely because of the complexity of the original hydrothermal systems and subsequent alteration. Conversely, at Santorini (where the source term and boundary conditions are relatively well known) the material and elemental sources are not necessarily close analogs to spent fuel or vitrified waste forms. Nevertheless, the physical similarities between these sites and Yucca Mountain could permit identification and characterization of relevant waste-form degradation and contaminant migration phenomena, and could aid in the development and validation of predictive models for performance assessments.

7.4 REFERENCES

- Alexander, D. H., and A. E. Van Luik. 1990. Natural analogue studies useful in validating regulatory compliance analyses. *Proceedings GEOVAL*. Stockholm, Sweden.
- Byers, F. M. Jr.. 1985. *Petrochemical Variation of Topopah Spring Tuff Matrix with Depth (Stratigraphic Level), Drill Hole USW G-4, Yucca Mountain, Nevada*. LA-10561-MS, UC-70. Los Alamos, New Mexico: Los Alamos National Laboratory (LANL).
- Cardenas-Flores, D. 1985. Volcanic stratigraphy and U-Mo mineralization of the Sierra de Peña Blanca District, Chihuahua, Mexico. *Uranium Deposits in Volcanic Rocks*. Proceedings of a technical committee meeting, El Paso, Texas, April 1984. IAEA-TC-490. Austria: International Atomic Energy Agency (IAEA):125-136.

- Coles, D. G., and L. D. Ramspot. 1982. Migration of ruthenium-106 in a Nevada test site aquifer: Discrepancy between field and laboratory results. *Science* 215:1235-1237.
- Department of Energy (DOE). 1988. *Site Characterization Plan: Yucca Mountain Site, Nevada Research and Development Area, Nevada*. DOE/RW-0199. Washington, D.C.: DOE.
- Gale, N. H., and Z. Stos-Gale. 1981. Lead and silver in the ancient Aegean. *Scientific American* 244:176-192.
- George-Aniel, B. G., J. Leroy, and B. Poty. 1985. Uranium deposits of the Sierra Peña Blanca. *Uranium Deposits in Volcanic Rocks*. Proceedings of a technical committee meeting, El Paso, Texas, April 1984. IAEA-TC-490. Austria: IAEA:175-186.
- Goodell, P. C. 1981. Geology of the Peña Blanca uranium deposits, Chihuahua, Mexico. *Uranium in Volcanic and Volcaniclastic Rocks: AAPG Studies in Geology*. No. 13. El Paso, Texas: American Association of Petroleum Geologists:275-291.
- Goodell, P. C. 1985. Chihuahua City uranium province, Chihuahua, Mexico. *Uranium Deposits in Volcanic Rocks*. Proceedings of a technical committee meeting, El Paso, Texas, April 1984. IAEA-TC-490. Austria: IAEA:97-124.
- Hammer, C. U., H. B. Clausen, W. L. Friedrich, and H. Tauber. 1987. The Minoan eruption of Santorini in Greece dated to 1645 BC? *Nature* 328(6):517-519.
- Heiken, G., and F. McCoy, Jr. 1984. Caldera development during the Minoan eruption, Thira, Cyclades, Greece. *Journal of Geophysical Research* 89(B10):8441-8462.
- International Geological Congress (IGC). 1989. Geological problems in radioactive waste isolation: a world wide review. Workshop W3B. P. A. Witherspoon and G. de Marsily, conveners. *28th International Geological Congress, Washington, D.C.* LBL-27333. Berkeley, California: Lawrence Berkeley Laboratory (LBL):42.
- Krumhansl, J. L., and H. W. Stockman. 1988. Site selection criteria and preliminary results from the Valles Caldera natural analog study. *Proceedings of Workshop IV on Flow and Transport through Unsaturated Fractured Rock Related to High-Level Radioactive Waste Disposal*. Tucson, Arizona: University of Arizona:249-250.
- Marinos, G. P., and P. G. Marinos. 1978. The groundwater potential of Santorini Island. *Thera and the Aegean World*. London: Thera and the Aegean World, Inc.:297-305.
- McCoy, F. W. 1980. Climatic change in the eastern Mediterranean area during the past 240,000 years. *Thera and the Aegean World*. London: Thera and the Aegean World, Inc.:79-100.

- Petruso, K. M. 1978. Lead weights from Akrotiri: preliminary observations. *Thera and the Aegean World*. London: Thera and the Aegean World, Inc.:547-553.
- Pichler, H., and W. L. Friedrich. 1976. Radiocarbon dates of Santorini volcanics. *Nature* 262:373-374.
- Pichler, H., and W. L. Friedrich. 1980. Mechanism of the Minoan eruption of Santorini. *Thera and the Aegean World*. London: Thera and the Aegean World, Inc.:15-30.
- Pichler, H., and S. Kussmaul. 1980. Comments of the geological map of the Santorini Islands. *Thera and the Aegean World*. London: Thera and the Aegean World, Inc.:413-427.
- Thompson, J. L. (ed.). 1985. *Laboratory and Field Studies Related to the Radionuclide Migration Project*. LA-10372-PR. Los Alamos, New Mexico: LANL.
- Watkins, N. D., R. S. J. Sparks, H. Sigurdsson, T. C. Huang, A. Federman, S. Carey, and D. Ninkovich. 1978. Volume and extent of the Minoan tephra from Santorini volcano: new evidence from deep-sea cores. *Nature* 271:122-126.
- Wenrich, K. J., P. J. Modreski, R. A. Zielinski, and J. L. Seeley. 1982. Margaritasite: a new mineral of hydrothermal origin from the Sierra de Peña Blanca uranium district, Mexico. *American Mineralogist* 67:1273-1289.

APPENDIX A

**High-Resolution Modeling of Strip Source Infiltration:
Three-Dimensional Synthetic Experiment Analogous
to the Las Cruces Trench Experiment
*by R. Ababou***

**High-Resolution Modeling of Strip Source Infiltration:
Three-Dimensional Synthetic Experiment
Analogous to Las Cruces Trench Experiment**

by

Rachid Ababou
Center For Nuclear Waste Regulatory Analyses
Southwest Research Institute
San Antonio, Texas 78228-0510

ABSTRACT

A high-resolution, three-dimensional finite difference model based on a mixed variable formulation of partially saturated or unsaturated flow is used to model strip source infiltration and natural drainage in a randomly heterogeneous and imperfectly stratified soil. The flow regime, soil properties, and boundary conditions are analogous to those of the first Las Cruces strip source experiment, albeit with some differences. The nonlinear behavior and statistical properties of the unsaturated soil are inferred, in part, from preliminary hydrodynamic data collected at the trench site. A 15 m x 15 m x 5 m computational domain is discretized into 300,000 finite difference cells or grid points. The parameters of the unsaturated conductivity curve are assumed to be single realizations of spatially correlated random fields. Each finite difference cell possesses its own, distinct conductivity function. The detailed simulation captures the complex three-dimensional heterogeneity of the transient moisture plume, and provides direct evidence of horizontal spreading and moisture-dependent anisotropy due to imperfect, spatially variable stratification.

1.0 INTRODUCTION

1.1 Modeling Group Identification

The numerical model and simulation results described here were previously generated and partially analyzed by the M.I.T. group [Ababou 1988; Ababou and Gelhar 1988]. The Center for Nuclear Waste Regulatory Analyses is currently exploiting these results and developing new simulations toward model validation [Ababou, 1990].

1.2 Purpose and Overview

The simulations to be described below were developed with two distinct objectives in mind. The first objective was to test the linearized analytical theory of stochastic flow [Mantoglou and Gelhar, 1987 a,b,c], and particularly the moisture-dependent anisotropy of effective flow behavior, under more realistic conditions of nonlinearity, randomness, and flow geometry than allowed for in theory. The second objective was, given the constraints of the first theoretical

objective, to mimic as closely as possible the conditions of the first Las Cruces strip-source experiment.

2.0 NUMERICAL EXPERIMENT SET-UP

2.1 Input Data

The problem set-up, described below, involves a strip-source geometry and discharge rate similar to those of the first Las Cruces strip-source experiment. However, the initial soil moisture ($\theta = 0.15$, or $\Psi = 150$ cm) used in the model was higher than that observed at the field site in order to avoid an excessive conductivity contrast near the wetting front. Note that relatively low rate infiltration in moderately dry soil can produce large conductivity contrasts, owing to the very sharp decrease of conductivity with increasing suction for the exponential conductivity model adopted here.

One of the main reasons for selecting the exponential conductivity model was its convenience for developing analytical solutions of the stochastic flow equations [Mantoglou and Gelhar, a,b,c]. The exponential relationship is not adequate for modeling the very dry range of unsaturated flow. Recognizing this restriction, we studied the discrepancy between exponential and other conductivity models (Mualem-Van Genuchten) for the field site data. The discrepancy was found to be relatively minor in the suction range $50 \text{ cm} \leq \Psi \leq 150 \text{ cm}$. This is illustrated in Figure 1 from Ababou [1988, Chap. 7, Fig. 7.10].

Besides being highly nonlinear, the two-parameter exponential conductivity curve $K(h, \underline{x}) = K_{\text{sat}}(\underline{x}) \exp(\alpha(\underline{x})h)$ was highly variable in space as well. The parameters $K_{\text{sat}}(\underline{x})$ and $\alpha(\underline{x})$ were assumed to be spatially correlated replicates of two log-normally distributed, independent random fields. Furthermore, the three-dimensional correlation structure was taken to be anisotropic, with a vertical-to-horizontal anisotropy ratio of 1/4 in terms of the directional correlation scales.

A summary of input data is given in Table 1, from Ababou [1988, Chap. 7, Table 7.2]. Note that the coefficients of variation of K_{sat} and α are 67% and 22%, respectively. Single-point and two-point statistics were inferred more or less directly from in-situ field observations such as those reported in Wierenga et al. [1989]. During infiltration, the top boundary condition was a fixed flux of 2 cm/day imposed on the 4 m wide strip source, and zero flux elsewhere. The lateral boundary conditions were zero flux. The bottom boundary condition was gravity drainage (zero pressure gradient). The gravity drainage condition was quite successful in allowing moisture plumes to migrate downward, through the bottom boundary, with minimal disturbance. For more details on problem set-up, see Ababou [1988, Section 7.3.1]. For random field generation by the Turning Band method, see also Tompson et al. [1989].

2.2 Simulation and Output Data

The numerical code "BIGFLO", previously developed at MIT [Ababou, 1988], was used to generate the results discussed here. The BIGFLO code is a fully three-dimensional finite difference simulator for saturated or partially saturated flow in highly heterogeneous porous media. The algorithms are described in detail in Ababou [1988, Chap. 5]. Summaries of solution algorithms and model problems can be found in Ababou and Gelhar [1988] for the case of unsaturated flow, and Ababou et al. [1989] for the case of saturated flow.

The strip source simulation comprised two phases, an infiltration phase ($q=2$ cm/day) and a natural drainage phase ($q=0$). Given the depth of the computational domain (5 m) and the particular choice of initial conditions discussed earlier, infiltration was turned off after a relatively short time (10 days) and natural drainage was simulated for 10 more days. The simulation outputs were expressed mainly in terms of three-dimensional pressure fields. Output times of interest here are $t=5$ days and $t=10$ days (infiltration phase), and $t=15$ days (drainage phase).

A preliminary visualization of the results was obtained by contouring the pressure fields along selected slices [Ababou, 1988, Chap. 7.3]. More recently, the fully three-dimensional pressure fields have been visualized using 3D color graphics techniques such as perspective views of solid, color-coded iso-surfaces in 3D space [Ababou, 1990]. Each frame represents a snapshot of the moisture plume at a fixed, pre-selected output time.

3.0 ANALYSIS OF SIMULATION RESULTS

Some of the heterogeneous suctions obtained for three vertical slices are shown in *Figure 2* ($t=5$ days), *Figure 3* ($t=10$ days), and *Figure 4* ($t=15$ days). We recall from the previous section that the infiltration phase ended at $t=10$ days. Also, note that the heterogeneous moisture content distribution follows the same pattern as pressure, due to the fact that a single one-to-one relation $\theta-\theta(\Psi)$ was assumed, regardless of spatial location.

The detailed moisture patterns at any time differ considerably from section to section, reflecting the three-dimensional nature of the local flow process. If the soil was uniformly layered, rather than randomly stratified as here, the moisture patterns in any vertical cross-section would be nearly the same everywhere except near the free edge of the finite length strip source.

It is interesting to analyze the vertical versus horizontal extent of the moisture movement as seen in these figures. Let us define the moisture plume by $\theta \geq \theta_f$, where θ_f is a relatively dry moisture content, e.g. close to the initial value. The contours shown in *Figures 2, 3, 4* reveal significant lateral spread of the moisture plume. A number of localized wet lenses appear to be hanging over drier regions, reflecting the statistical anisotropy, or imperfect stratification, of the synthetic soil. This feature can be observed near the geometric center of the $x_2=9.8$ m cross-section (around depth $x_1=2.5$ m and abscissa $x_3=0$). Another, more

subtle phenomenon is the relatively larger spread of the relatively dry margins of the moisture plume (light gray tones), compared to the wet core of the plume (dark gray tones). This behavior is consistent with the moisture-dependent anisotropy predicted by Mantoglou and Gelhar [1987 a,b,c].

The above-mentioned features appear more clearly in full three-dimensional representation. The attached black-and-white reproductions of color plates, *Figure 5* and *Figure 6*, show three-dimensional views of the moisture plume after 10 days of infiltration. The amount of detail in this simulation helps capture the heterogeneity of the moisture pattern over a wide range of scale. The horizontal spread due to random stratification is clearly far from uniform. Layers have "holes". Horizontal "fingers" and wet lenses tend to remain suspended over dryer lenses of soil.

These results are encouraging, and suggest the feasibility of similar simulations under conditions more closely related to the Las Cruces Trench experiment. This may involve, for instance, using both probabilistic and site-specific deterministic input data, combined through stochastic conditioning techniques (work in progress).

4.0 REFERENCES

- Ababou R., *Three-Dimensional Flow in Random Porous Media, PhD Thesis, Department of Civil Engineering, Massachusetts Institute of Technology, Cambridge, Massachusetts, 2 Volumes, 833 pp., Jan. 1988.*
- Ababou R., *High-Resolution Modeling of Three-Dimensional Flow Fields, 4th INTRAVAL Workshop, Las Vegas, Nevada, Feb. 5-10, 1990.*
- Ababou R. and Gelhar L. W., *A High-Resolution Finite Difference Simulator for 3D Unsaturated Flow in Heterogeneous Media, in Computational Methods in Water Resources, Elsevier and Computational Mechanics Publications, Vol. 1, 173-178, June 1988.*
- Ababou R., McLaughlin D., Gelhar L. W., Tompson A. F., *"Numerical Simulation of Three-Dimensional Saturated Flow in Randomly Heterogeneous Porous Media", Transport in Porous Media, 4, 549-565, 1989.*
- Mantoglou A. and Gelhar L. W., (1987a), *"Stochastic Modeling of Large-Scale Transient Unsaturated Flow Systems", Water Resour. Res., 23(1), 37-46.*
- Mantoglou A. and Gelhar L. W., (1987b), *"Capillary Tension Head Variance, Mean Soil Moisture Content, and Effective Specific Soil Moisture Capacity of Transient Unsaturated Flow in Stratified Soils", Water Resour. Res., 23(1), 57-67.*
- Mantoglou A. and Gelhar L. W., (1987c), *"Effective Hydraulic Conductivities of Transient Unsaturated Flow in Stratified Soils", Water Resour. Res., 23(1), 57-67.*

- Tompson A. F., Ababou R., and Gelhar L. W., Implementation of the Three-Dimensional Turning Bands Random Field Generator, *Water Resour. Res.*, 25(10), 2227-2243, 1989.
- Wierenga P. J., Gelhar L. W., Simmons C. S., Gee G.W., and Nicholson T.J., "Validation of Stochastic Flow and Transport Models for Unsaturated Soils: A Comprehensive Field Study", Report NUREG/CR-4622, U. S. Nuclear Regulatory Commission, Washington, D.C., 1986.
- Wierenga P. J., Toorman A., Hudson D., Vinson J., Nash M., and Hills R. G., "Soil Physical Properties at the Las Cruces Trench Site," NUREG/CR-5541, U. S. Nuclear Regulatory Commission, Washington, DC, (1989).

ATTACHMENT: Tables, Figures, and Color Plates

TABLE 1

SUMMARY OF INPUT DATA FOR THE SINGLE-REALIZATION SIMULATION OF STRIP-SOURCE INFILTRATION IN A STATISTICALLY ANISOTROPIC SOIL ("TRENCH EXPERIMENT")

Type of Data	Description	Value
Domain Geometry, Boundary Conditions, and Initial Conditions	Vertical domain size Transverse horizontal domain size Transverse longitudinal domain size Strip source width Strip source length Flux at the surface of the strip Condition at the bottom boundary Initial pressure head	$L_1 = 5.0 \text{ m}$ $L_2 = 15.0 \text{ m}$ $L_3 = 15.0 \text{ m}$ $W_s = 4.0 \text{ m}$ $L_s = 9.9 \text{ m}$ $q_0 = 2 \text{ cm/day}$ $q_1 = -K(h)$ $h_{in} = -150 \text{ cm}$
Space-Time Discretization	Time step Mesh size Δx_i ($i=1,2,3$) Unidirectional number of nodes n_i Total number of nodes of 3D grid	Variable $\Delta x_i = 0.10, 0.20, 0.20 \text{ m}$ $n_i = 52, 76, 76$ $N = 300352$
Exponential Conductivity Curve (Random)	Geometric mean saturated conductivity Standard deviation of $\ln K_s$ Geometric mean of the $\ln K$ -slope Standard deviation of $\ln \alpha$ Anisotropic correlation scales λ_i	$K_G = 100 \text{ cm/d}$ $\sigma_f = 0.6083$ $\alpha_G = 0.0494 \text{ cm}^{-1}$ $\sigma_a = 0.2202$ $\lambda_i = 0.25, 1.0, 1.0 \text{ m}$
Van-Genuchten Retention Curve (Deterministic)	Saturated moisture content Residual moisture content Scaling parameter Shape factor (real number)	$\theta_s = 0.368$ $\theta_r = 0.102$ $\beta = 0.0334 \text{ cm}^{-1}$ $n = 1.982$

LAYER 1 TRENCH

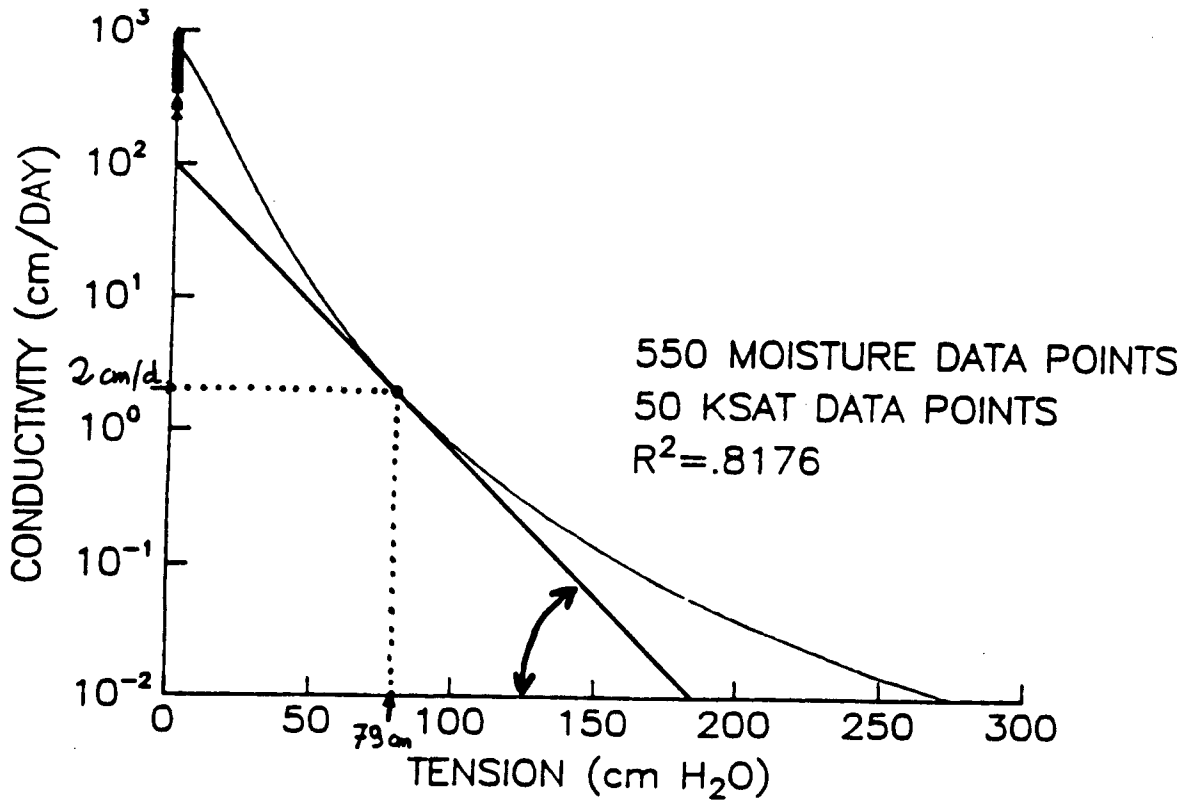


Figure 1. Mean unsaturated conductivity curve $K(h)$ for the soil of the strip-source "trench experiment": the straight line corresponds to the exponential model actually used in the numerical simulation; the other curve is the Mualem-Van Genuchten model indirectly fitted to field data by Wierenga et. al., 1986.

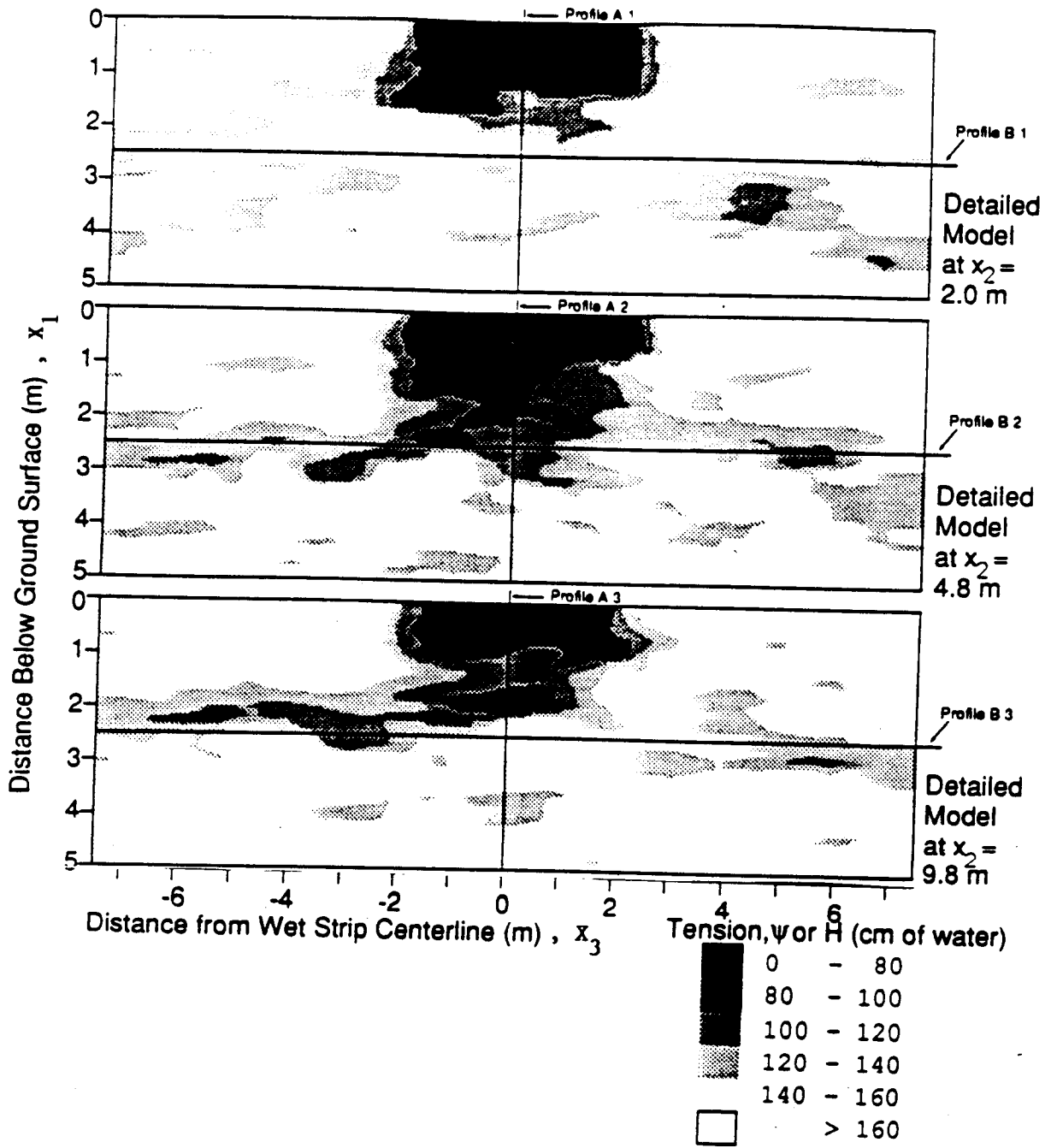


Figure 2. Infiltration ($t=5$ days)

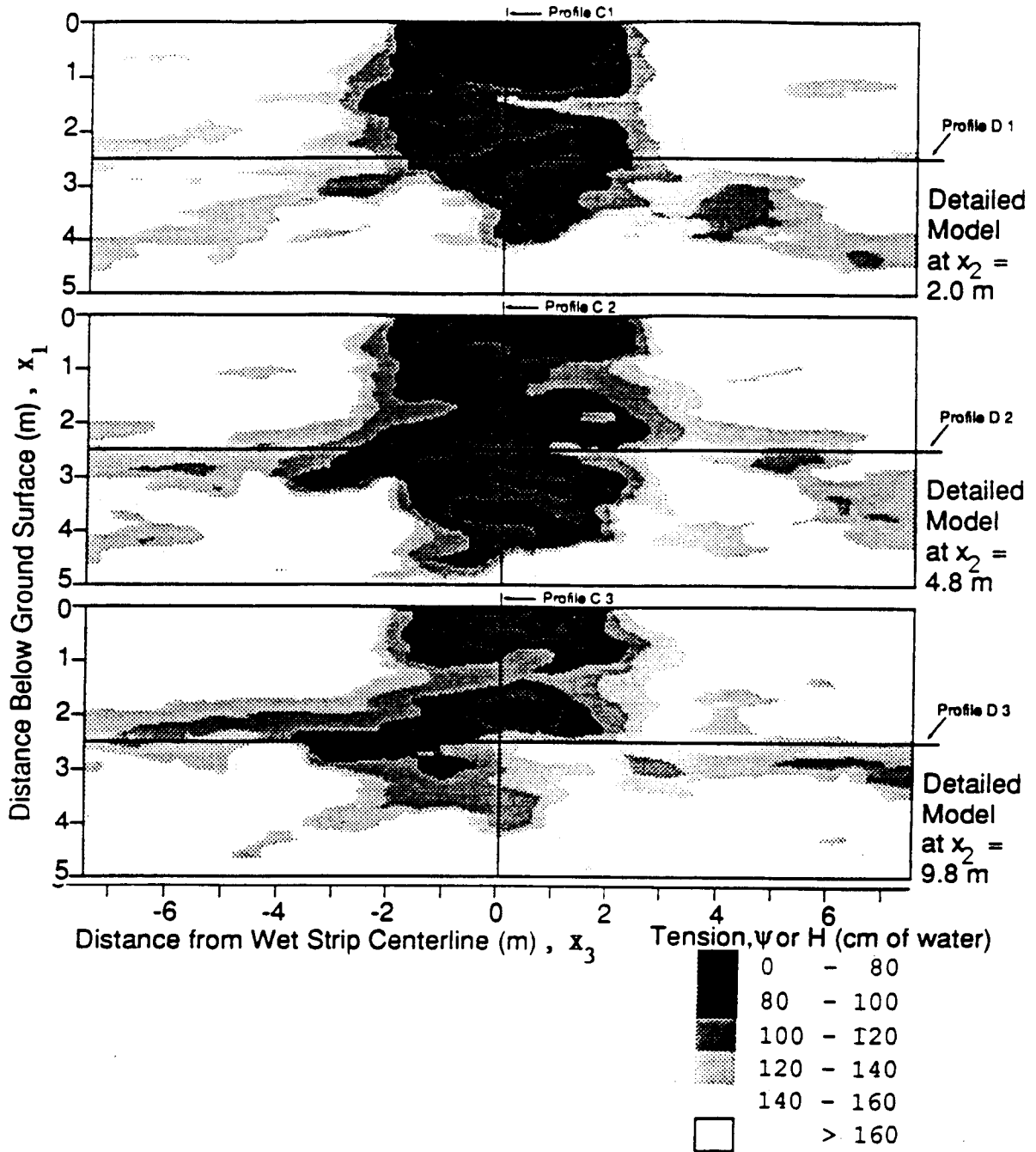


Figure 3. Infiltration (t=10 days)

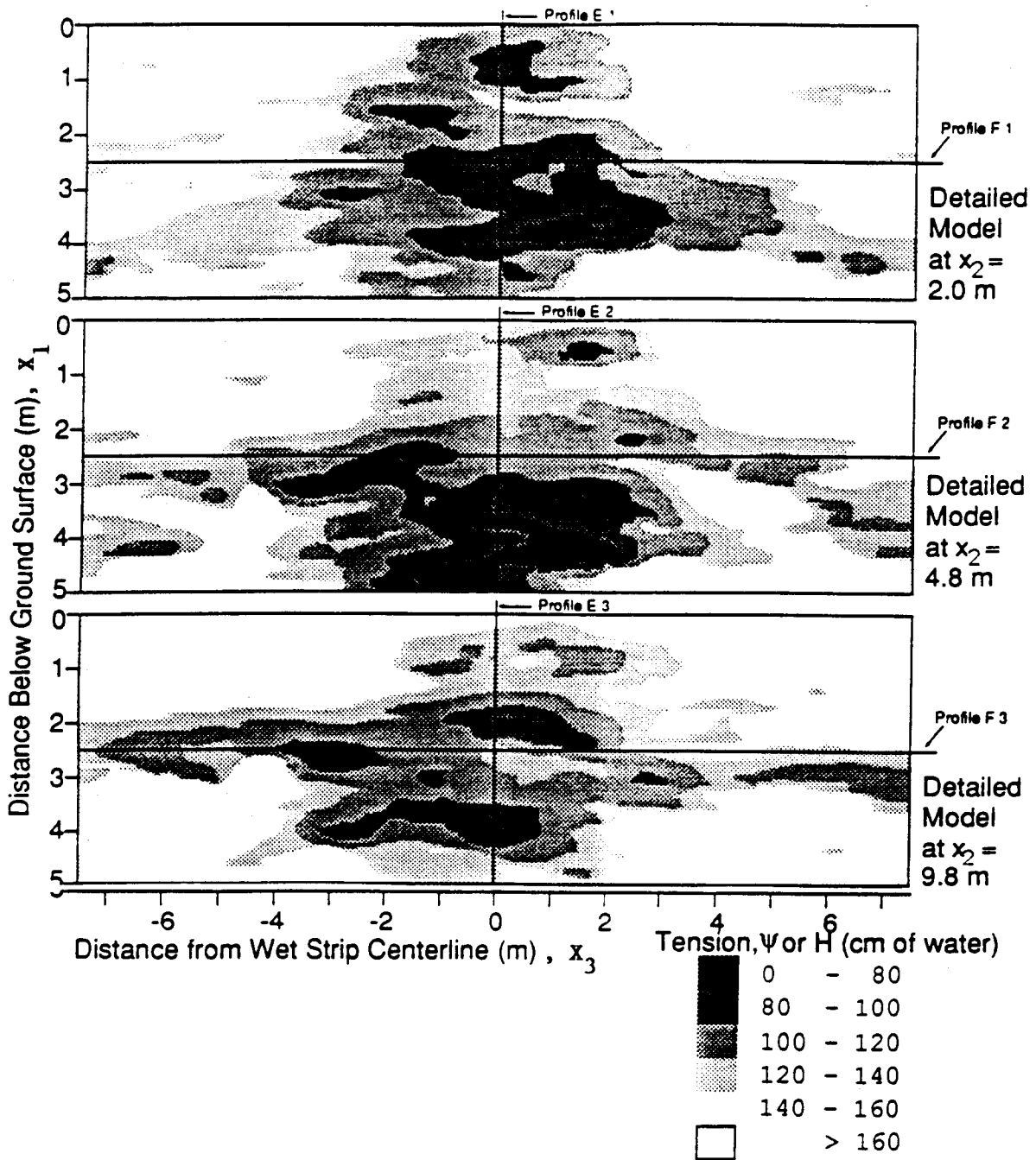


Figure 4. Drainage ($t=15$ days)

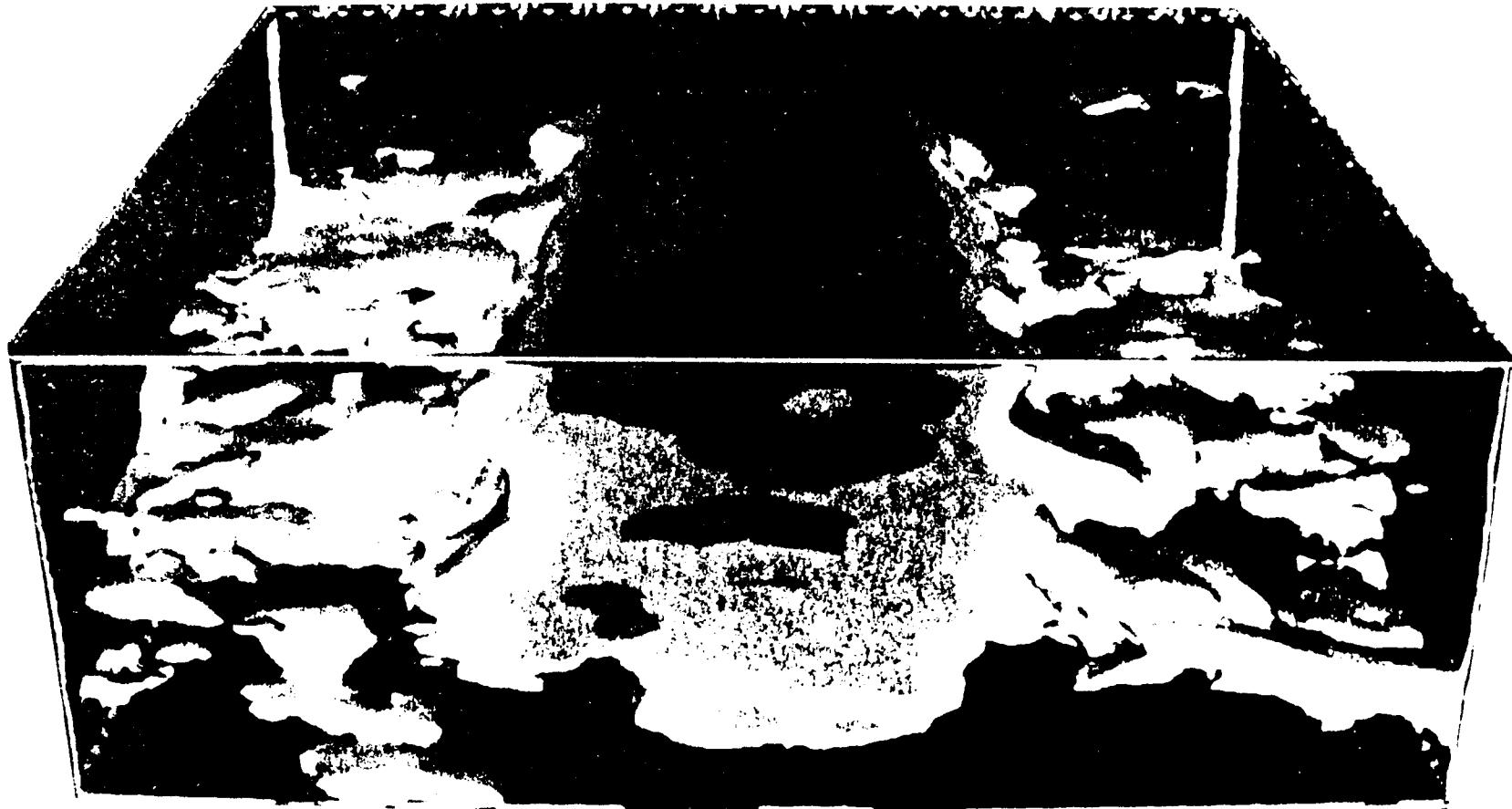


Figure 5. Front View of Three-Dimensional Moisture Plume, from Stochastic Flow Simulations of Ababou (1988).

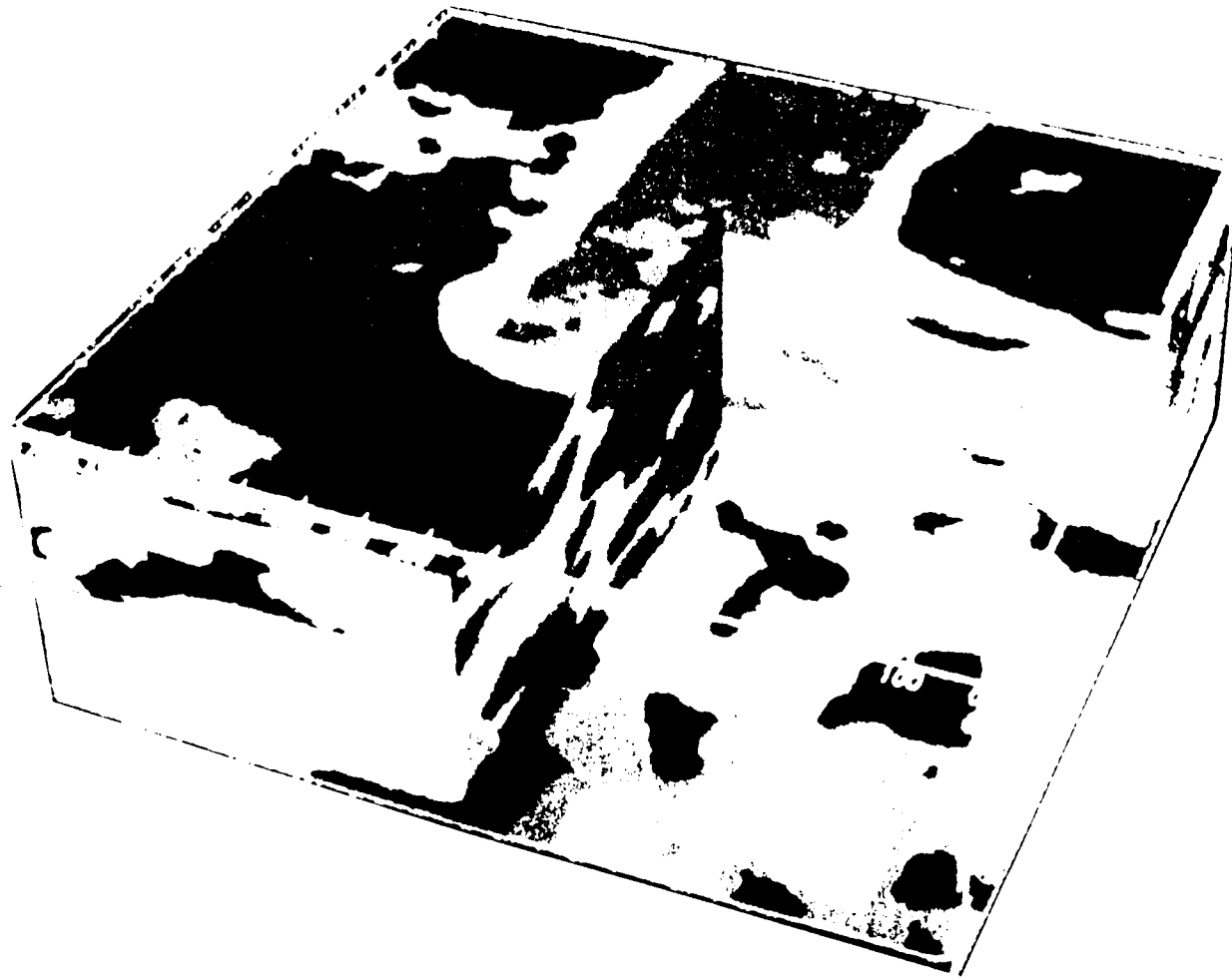


Figure 6. Back View of Three-Dimensional Moisture Pattern, with Moisture Plume Visible in Purple and Blue (Simulations from Ababou, 1988).

APPENDIX B

Numerical Analysis of Nonlinear Unsaturated Flow Equations
by R. Ababou

VIIIth International Conference on
Computational Water Resources,
Venice, Italy, June 11-15, 1990.

NUMERICAL ANALYSIS OF NONLINEAR
UNSATURATED FLOW EQUATIONS

Rachid Ababou

Southwest Research Institute,
Center for Nuclear Waste Regulatory Analyses,
San Antonio, TX 78228, U.S.A.

ABSTRACT:

The numerical behavior of the nonlinear unsaturated flow equation is examined analytically for an implicit finite difference scheme. The governing equation combines nonlinear diffusion and convection operators, and is characterized by a simple Peclet number. Numerical errors are investigated using truncation error analysis, frozen stability analysis, and functional analysis of the nonlinear mapping associated with Picard iterations. These approaches shed light on different but complementary aspects of the same numerical problem.

NUMERICAL ANALYSIS OF NONLINEAR
UNSATURATED FLOW EQUATIONS

Rachid Ababou

Southwest Research Institute,
Center for Nuclear Waste Regulatory Analyses,
San Antonio, TX 78228, U.S.A.

ABSTRACT:

The numerical behavior of the nonlinear unsaturated flow equation is examined analytically for an implicit finite difference scheme. The governing equation combines nonlinear diffusion and convection operators, and is characterized by a simple Peclet number. Numerical errors are investigated using truncation error analysis, frozen stability analysis, and functional analysis of the nonlinear mapping associated with Picard iterations. These approaches shed light on different but complementary aspects of the same numerical problem.

INTRODUCTION:

Flow in unsaturated porous media is governed by a strongly nonlinear diffusion type equation with a nonlinear, forced convection term due to gravity. These features make it particularly difficult to solve by any means. Analytical solutions have been and are still providing valuable insights for certain classes of flows, but most realistic problems have to be solved numerically: see [1] and [2] for high-resolution supercomputer simulations of 3-dimensional, transient unsaturated flow in randomly heterogeneous and stratified media.

Our experience is that the strong nonlinearity of unsaturated flow usually causes considerable numerical difficulties and requires trial-and-error adjustments of mesh size, time step, relaxation parameters, tolerance criteria, and adaptive controls. To improve the efficiency of future numerical algorithms will require some understanding of how the specific features of the unsaturated flow equation contribute to numerical errors. Exploring this question constitutes the main purpose of this paper.

UNSATURATED FLOW EQUATIONS:

For transient flow in variably saturated porous media, a mixed variable formulation of the governing equation is obtained by combining the mass conservation equation ($\partial\theta/\partial t = -\nabla \cdot Q$) with the Darcy-Buckingham equation ($Q = -K\nabla H$):

$$\partial\theta(h,x)/\partial t = \nabla (K(h,x) (\nabla h + g)) \quad (1)$$

where $H=h+g \cdot x$ is the hydraulic potential, h is pressure head, and g is the cosine vector aligned with the acceleration of gravity and equal to $(0,0,-1)$ if the third axis is vertical pointing downwards. Defining the specific moisture capacity $C = \partial\theta/\partial h$ yields the pressure-based Richards equation:

$$C(h,x) \partial h/\partial t = \nabla (K(h,x) (\nabla h + g)) \quad (2)$$

Introducing a nonlinear moisture diffusivity $D=K/C$, assuming a spatially homogeneous moisture retention curve $\theta(h)$, and $h \leq 0$ everywhere, yields the moisture-based version of eq.(1):

$$\partial\theta/\partial t = \nabla (D(\theta,x) \nabla\theta + g K(\theta,x)) \quad (3)$$

In the detailed 3-dimensional simulations of [1] and [2], the finite difference method was applied to the mixed form (1), which is more mass conservative than eq.(2) and is not limited to negative pressures as eq.(3). For convenience, however, we will use the standard Richards equation (2) for the numerical analyses to be developed in this paper.

The nonlinear gravity term containing (g) acts as forced convection, in competition with the diffusion term represented by the elliptic operator $\nabla(K\nabla h)$. For homogeneous media, eqs.(2) and (3) can be reformulated as follows, respectively:

$$C (\partial h/\partial t + v \cdot \nabla h) = \nabla(K\nabla h) \quad (2)'$$

and:

$$\partial\theta/\partial t + v \cdot \nabla\theta = \nabla(D\nabla\theta) \quad (3)'$$

where:

$$v = - (\partial K/\partial\theta) g \quad (4)$$

The vector v represents the velocity of pressure or moisture disturbances, in the absence of the right-hand side diffusive terms. Note that moisture and pressure waves propagate at the same speed in homogeneous media. The convective-diffusive form taken by equations (2-3) suggests that a Peclet number might be used to characterize convection versus diffusion effects.

A Peclet number emerges quite naturally from the Kirchhoff transform formulation [1]. This transform is valid for the class of heterogeneous media possessing a homogeneous relative conductivity curve $K_r(h)$, i.e. with a separable conductivity curve $K(h,x) = K_s(x)K_r(h)$. But we focus here on the more restricted case where both the saturated and relative

conductivities are homogeneous, i.e. with a homogeneous conductivity curve $K(h)=KsKr(h)$. The Kirchoff transform is then defined by:

$$\phi(h) = \int_{-\infty}^h K(h') dh' \quad (6)$$

Substituting eq.(6) in eq.(2) and using chain rules yields:

$$\partial\phi/\partial t + v.\nabla\phi = D \nabla^2\phi \quad (7)$$

Here again, the wave velocity V is given by equation (4), or equivalently by $V = -\alpha Dg$, where $\alpha = \partial \ln K / \partial h$ is the slope of the log-conductivity/pressure curve.

Given the form of the Kirchoff equation (7), the Peclet vector $Pe = Vl/D$ emerges as a relative measure of convective versus diffusive moisture transport over the chosen length scale (l). Furthermore, substituting the above expression for V gives a very simple expression for the Peclet vector:

$$Pe = -\alpha lg \quad (8)$$

which reveals the special role played by the α -parameter. Since transforms like $\theta(h)$ or $\phi(h)$ do not fundamentally alter the ratio of convection versus diffusion coefficients, this Peclet vector characterizes the transport of pressure as well as moisture, Kirchoff potential, or any other quantity that can be related to pressure in a one-to-one fashion.

TRUNCATION ERROR ANALYSIS:

In this section, we evaluate truncation error as a function of mesh size and time step for a nonlinear, implicit finite difference discretization of the Richards equation. Note that truncation analysis compares the discrete and differential operators, but is not concerned with the numerical errors incurred by the dependent variable itself, or with the space-time propagation of such errors (stability), or with the additional errors incurred while solving the nonlinear discretized system (linearization). Our purpose here is to identify potential sources of inaccuracies by looking at the leading order terms of truncation error.

Consider the Richards equation (2), to be solved for a 1-dimensional homogeneous medium using a fully implicit nonlinear finite difference discretization (Euler backwards in time, 2-point centered in space). The differential and discretized equations are, respectively:

$$\mathcal{L}(h) = -C(h) h_t + (K(h) (h_x + g))_x = 0 \quad (9.a)$$

$$L(h_i^{n+1}) = -C_i^{n+1} \frac{h_i^{n+1} - h_i^n}{\Delta t} + \frac{K_{i+1/2}^{n+1}}{\Delta x} \left[\frac{h_{i+1}^{n+1} - h_i^{n+1}}{\Delta x} + g \right] - \frac{K_{i-1/2}^{n+1}}{\Delta x} \left[\frac{h_i^{n+1} - h_{i-1}^{n+1}}{\Delta x} + g \right] = 0 \quad (9.b)$$

where g is a cosine representing gravity, with $g=0$ if x is horizontal and $g=-1$ if x is vertical downwards. The coefficients of the discrete operator are fully nonlinear, being expressed at the current time step ($n+1$). The mid-nodal conductivities are approximated by a geometric weighting:

$$K_{i+1/2} = \left[K(h_i) K(h_{i+1}) \right]^{1/2} \quad (10)$$

In the case of an exponential $K(h)$ curve, this scheme weights pressures arithmetically, and it yields the exact midnodal conductivity in zones of spatially constant pressure gradient.

The truncation error $E(h)=L(h)-\mathcal{L}(h)$ at the nodes of the space-time mesh was calculated in [1] using intermediate results from [3]. We choose here to express the final result in terms of both flux (Q) and pressure (h) as follows:

$$E(h) \approx \Delta t \left[\frac{\partial}{\partial x} \left[K \frac{\partial}{\partial t} \left(\frac{\partial h}{\partial x} \right) \right] - \frac{C}{2} \frac{\partial^2 h}{\partial t^2} \right] + \frac{\Delta x^2}{24} \left[\frac{\partial}{\partial x} \left(K \frac{\partial^3 h}{\partial x^3} \right) - \frac{\partial^3 Q}{\partial x^3} \right] - \frac{\Delta x^2}{8} \left[\alpha \frac{\partial}{\partial x} \left(Q \frac{\partial^2 h}{\partial x^2} \right) \right] \quad (11)$$

where $Q=-K(\partial h/\partial x+g)$, and $\alpha=\partial \ln K/\partial h$. It is interesting to note that one recovers the linear heat equation by letting $K=1$, $C=1$, and $\alpha=0$ in (9-11). Inserting in eq.(11) the identities:

$$h_t = h_{xx} \quad \text{and} \quad h_{tt} = -Q_{xxx} = h_{xxxx} ,$$

leads to the verification of a well known result [4]: the order of accuracy of the linear heat equation increases from $O(\Delta t)+O(\Delta x^2)$ to $O(\Delta t^2)+O(\Delta x^4)$ with the choice $\Delta t/\Delta x^2 = 1/6$.

Let us now discuss the implications of (11) in the fully nonlinear case. The $O(\Delta t)$ term, due to temporal discretization errors, appears to be controlled by the rate of change of the pressure gradient and by the second order time-derivative of pressure. The first of the two $O(\Delta x \Delta x)$ terms is due to spatial discretization errors other than midnodal conductivity weighting. The second $O(\Delta x \Delta x)$ term is due solely to errors in evaluating midnodal conductivities by the geometric rule (10), and vanishes in regions of spatially constant pressure gradient, as expected in the case of exponential $K(h)$.

Equation (11) simplifies considerably in the steady state case, since the 1-dimensional flux Q becomes constant in both space and time. The result suggests that, even in the transient case, spatial errors are dominated by the rate of change of pressure curvature with depth, which can become quite large near sharp wetting fronts above and below the inflexion point. This type of information may be used for designing optimal adaptive grid procedures.

STABILITY ANALYSIS:

To complement the previous truncation error analysis, we now examine how numerical errors propagate as a function of time. In addition, we hope to capture at least some of the additional error amplification effects due to inexact treatment of nonlinearity. Our approach is to analyze the stability of a linearized version of the finite difference problem, such that all nonlinear coefficients are evaluated from the solution at the previous time step (no iterations). The unstable effect of linearization is partially taken into account by unfreezing the nonlinear convective coefficient, while other coefficients remain frozen.

We focus once more on the case of 1-dimensional homogeneous media as in eqs.(9). Consider the following linearized form of the finite difference system:

$$C_i^n \frac{h_i^{n+1} - h_i^n}{\Delta t_n} = \frac{1}{\Delta x} \left[K_{i+\frac{1}{2}}^n \left[\frac{h_{i+1}^{n+1} - h_i^{n+1}}{\Delta x} + g \right] - K_{i-\frac{1}{2}}^n \left[\frac{h_i^{n+1} - h_{i-1}^{n+1}}{\Delta x} + g \right] \right] \quad (12)$$

where the superscript $(n+1)$ indicates the current time level. The form of this finite difference system suggests that, while the nonlinear diffusion operator is treated implicitly, the nonlinear gravity term $g(K[i+1/2]-K[i-1/2])/Δx$ is treated explicitly since it is entirely evaluated at the previous time level. Based on this remark, we will now examine how this discrepancy affects the numerical stability of the solution.

The proposed method is to develop a Fourier stability analysis of equation (12) with partially frozen coefficients. This is analogous to the usual frozen coefficients analysis as described in [4], except that the nonlinearity of the gravity term is taken into account via the quasilinear approximation:

$$g \frac{K_{i+\frac{1}{2}}^n - K_{i-\frac{1}{2}}^n}{\Delta x} = g \frac{K_i^n}{\Delta x} \frac{\alpha}{2} (h_{i+1}^n - h_{i-1}^n) + O(\Delta x^2) \quad (13)$$

where again $\alpha = d \ln K / dh$. The leading term on the right-hand side is expected to be a reasonable approximation of the left-hand side if the quantity $\alpha |h[i+1]-h[i]| \approx \alpha \Delta x |\partial h / \partial x|$ is on the order of unity or less. At any rate, even rough indications on

the numerical stability of the nonlinear unsaturated flow system will be useful given the lack of theoretical results in this area. With this provision, substituting (13) into (12) yields the following mixed implicit/explicit scheme:

$$\begin{aligned} & -\tilde{D}_{i-\frac{1}{2}} h_{i-1}^{n+1} + (1+\tilde{D}_{i-\frac{1}{2}}+\tilde{D}_{i+\frac{1}{2}}) h_i^{n+1} - \tilde{D}_{i+\frac{1}{2}} h_{i+1}^{n+1} \approx \\ & -\frac{1}{2} g \alpha \Delta x \tilde{D}_i h_{i-1}^n + h_i^n + \frac{1}{2} g \alpha \Delta x \tilde{D}_i h_{i+1}^n \end{aligned} \quad (14.a)$$

where \tilde{D} is the dimensionless diffusion coefficient:

$$\tilde{D}_{i(\pm\frac{1}{2})} = \frac{K_{i(\pm\frac{1}{2})} \Delta t}{C_i \Delta x^2} \quad (14.b)$$

The stability of equation (14) with frozen diffusion coefficients can be studied in the standard way using Fourier stability analysis [4]. This leads to a complex amplification factor, ρ , characterizing the growth rate of numerical errors in time:

$$\rho \approx \frac{1 + j \alpha g \Delta x \tilde{D}_i \sin(k \Delta x)}{1 + (\tilde{D}_{i+\frac{1}{2}} + \tilde{D}_{i-\frac{1}{2}})(1 - \cos(k \Delta x)) - j(\tilde{D}_{i+\frac{1}{2}} - \tilde{D}_{i-\frac{1}{2}})\sin(k \Delta x)} \quad (15)$$

where j is the square-root of -1 , and k is a Fourier mode or wavenumber taking discrete values: $k \in \{\pi/L, \dots, n\pi/L\}$.

Requiring $|\rho| \leq 1$ in equation (15) finally leads to the necessary and sufficient stability condition:

$$Pe = |\alpha g \Delta x| \leq 2 \sqrt{1 + \left(2 \frac{K_i \Delta t}{C_i \Delta x^2}\right)^{-1}} \quad (16)$$

where Pe represents the grid Peclet number [see eq.(8)]. If the Peclet number is less than 2, then the stability condition is always satisfied irrespective of the time step size. On the other hand, if the Peclet number is greater than 2, stability requires a stringent constraint on the time step size. To summarize, the stability condition is:

$$\begin{aligned} \text{either: } & Pe = |\alpha g \Delta x| \leq 2, \\ \text{else: } & Pe = |\alpha g \Delta x| \geq 2 \quad \text{and} \quad \frac{K_i \Delta t}{C_i \Delta x^2} \leq \frac{2}{(Pe-2)(Pe+2)} \end{aligned} \quad (17)$$

Recall that the Peclet number was defined as a convection to diffusion ratio [see discussion above eq.(8)]. When the grid Peclet number of eqs.(16-17) is much smaller than unity, pressure disturbances appearing at any node are smeared out by diffusion before reaching the next node (stable case).

Finally, the effects of heterogeneity can be analyzed in a qualitative manner as follows. Assume for instance that the α -parameter of the exponential conductivity curve is spatially variable. The local Peclet number is therefore also spatially variable. Assuming (roughly) that the previous stability analysis still holds locally, we see from equation (17) that instabilities must be triggered in zones of coarse porosity where α takes large values. Equation (15) shows that the most unstable Fourier modes are those with largest wavenumbers, having fluctuation scales comparable to mesh size. And, equation (16) indicates that such instabilities will grow faster where moisture diffusivity is high, e.g. in wet zones.

In order to minimize the chances of explosive error amplification, it seems reasonable to require that the vertical mesh size be a fraction of the average length scale $1/\alpha$, which typically lies in the range 10-100 cm for sandy to clayey soils. This guideline was used to design large scale numerical experiments of unsaturated flow in [1] and [2].

CONVERGENCE ANALYSIS OF NONLINEAR PICARD ITERATIONS:

In practice, an iterative scheme such as Picard or Newton must be used to iteratively linearize and solve the nonlinear algebraic system at each time step. For instance, a modified Picard scheme that preserves the symmetry of the system was used in [1,2]. In this section, we show how the convergence of the Picard scheme can be investigated by applying functional analysis methods [5,6,7] to the nonlinear mapping associated with the iteration scheme. The proposed approach is to apply the Picard method directly to the partial differential equation of unsaturated flow, and to examine the convergence properties of the resulting iteration scheme, a priori independent of discretization.

For illustration here, we will restrict our analysis to the special case of steady unsaturated flow in a spatially homogeneous 1-dimensional medium, for which an exact solution can be derived by direct integration. Assume that $K(h)$ is exponential with exponent $\alpha = \partial \ln K / \partial h$ and that the x-axis is vertical downwards. Define the dimensionless variables:

$$\xi = x/L, \quad \psi = -h/L, \quad a = \alpha/L, \quad q = Q/Ks, \quad \text{and} \quad k = K/Ks,$$

where ψ is the dimensionless suction head, always positive in unsaturated media. Our model problem is steady infiltration or evaporation in a vertical column extending, say, from soil surface at $z=0$ ($\xi=0$) to a water table or other boundary at $z=L$ ($\xi=1$). This can be formulated as the boundary value problem:

$$\mathcal{L}(\Psi) = (k(\Psi) (\Psi_{\xi} + 1))_{\xi} = 0 \quad (18)$$

$$\Psi(0) = \Psi_0 ; \quad \Psi(1) = \Psi_1$$

A straightforward integration of (18) yields the conductivity profile $k(\xi)$, which itself can be used to obtain the suction profile $\Psi(\xi)$. The complete solution is given by:

$$k(\Psi(\xi)) = q + (k_1 - q) \exp\{a(\xi - 1)\} \quad (19.a)$$

$$q = \{k_1 - k_0 \exp(a)\} / \{1 - \exp(a)\} \quad (19.b)$$

$$k(\Psi) = \exp(-a\Psi), \quad k_0 = k(\Psi_0), \quad k_1 = k(\Psi_1), \quad (19.c)$$

$$q \leq \{1 - k_1 \exp(-a)\} / \{1 - \exp(-a)\} \quad (19.d)$$

where the constant dimensionless flux q is either positive (downwards) or negative (upwards). Note that the solution is only valid for boundary conditions such that $\Psi(\xi) \geq 0$ on the $[0,1]$ interval. This requires satisfying $\Psi_0 \geq 0$, $\Psi_1 \geq 0$, and the inequality (19.d) which boils down to $q \leq 1$ if $a \gg 1$.

Let us now apply a Picard scheme with relaxation parameter ω to iteratively solve (18). The solution is constructed by way of an iterated mapping:

$$(k(\Psi^n) (\Psi^{n+1} - \Psi^n))_{\xi} = - \omega \mathcal{L}(\Psi^n) \quad (20)$$

$$\Psi^{n+1}(\xi) - \Psi^n(\xi) = 0 \quad \text{at} \quad \xi = 0 \quad \text{and} \quad \xi = 1$$

The residual operator $\mathcal{L}(\Psi)$ is the same as the one defined in equation (18), and n is the iteration counter. The Dirichlet conditions are implemented exactly at each iteration, since they are linear.

At each iteration, the iterated mapping of equation (20) is a boundary value problem that is directly integrable in terms of the incremental suction $\Psi[n+1] - \Psi[n]$. One obtains after some manipulations:

$$\Psi^{n+1} = \{ (1 - \omega) \mathcal{I}(\cdot) + \omega \mathcal{F}(\cdot) \} \Psi^n \quad (21.a)$$

where \mathcal{I} is the identity operator satisfying $\mathcal{I}(\Psi) = \Psi$, and \mathcal{F} is the Picard iteration operator defined by:

$$\mathcal{F}(\Psi^n) = \{ (\Psi_1 - \Psi_0 + 1) \mathcal{J}(\Psi^n) + (\Psi_0 - \xi) \} \quad (21.b)$$

where \mathcal{J} is the ratio of two integral operators:

$$F(\Psi^n) = \left[\int_0^\xi k(\Psi^n(s))^{-1} ds \right] / \left[\int_0^1 k(\Psi^n(s))^{-1} ds \right] \quad (21.c)$$

Each operator $\mathcal{U}(\cdot)$, $\mathcal{P}(\cdot)$, and $\mathcal{F}(\cdot)$ maps onto itself the space of continuous functions $\Psi(\xi)$ defined on the interval $[0,1]$, and (21.a) yields $\Psi[n+1](\xi) = \Psi[n](\xi)$ at $\xi=0$ and $\xi=1$.

The convergence properties of the Picard scheme are most directly related to the properties of the iteration operator (21.a) which maps the old solution $\Psi[n]$ into the new solution $\Psi[n+1]$. Without going into details, let us point out that the contraction mapping theorem and Ostrowski's local convergence theorem [7] can be used to test the conditions under which convergence occurs, and to estimate convergence rate in some function space norm. Work along these lines is ongoing. The case of transient flow will be developed by applying the same principles to the semi-discretized differential flow equation.

REFERENCES:

1. Ababou R. (1988): Three-Dimensional Flow in Random Porous Media, Ph.D. thesis, M.I.T., Cambridge, MA 02139, U.S.A., pp. 833, [Chapters 5 & 7].
2. Ababou R., and Gelhar L. W. (1988): A High-Resolution Finite Difference Simulator for 3D Unsaturated Flow in Heterogeneous Media, in: Computational Methods in Water Resources (VIIth Internat. Conf.), M. Celia et. al. ed., Elsevier & Comput. Mech. Publi., Vol. 1, 173-178.
3. Vauclin M., Haverkamp R., and Vachaud G. (1979): Résolution Numérique d'une Equation de Diffusion Nonlinéaire, P.U.G., Grenoble, France, pp. 183.
4. Ames W. F. (1977): Numerical Methods for Partial Differential Equations, Academic Press, New York, pp. 365, [Chapter 2].
5. Curtain R. F. and Pritchard A. J. (1977): Functional Analysis in Modern Applied Mathematics, Academic Press, New York, pp. 339.
6. Milne R. D. (1980): Applied Functional Analysis: An Introductory Treatment, Pitman, Boston.
7. Ortega J. M. and Rheinboldt W. C. (1971): Iterative Solution of Nonlinear Equations in Several Variables, Academic Press, New York, pp. 572, [5.1,7.1,10.1,12.1].